الجمهوريـــة الجـزائريـــة الديمقـراطيــة الشعبيـــة
وزارة التعـليم العالي و البحث العلمي

BADJI MOKHTAR- ANNABA UNIVERSITY
UNIVERSITE BADJI MOKHTAR - ANNABA

جامعة باجي مختار- عنابـة

Faculty: Sciences of Engineering **Year : 2018**
Department: Electrical Engineering

THESIS

Presented in order to obtain the diploma of Doctorate in Sciences

Entitled

Fault-tolerant control of energy processes

Option : Electrical Control

By : BOUTASSETA Nadir

Supervisor : RAMDANI Messaoud **Professor Université Badji-Mokhtar Annaba**

Committee Members :

President:	**LABAR Hocine,**	**Pr. Univ. Annaba**
Reviewers :	**LACHOURI Abderezzak,**	**Pr. Univ. Skikda**
	KHELIL Khaled,	**Pr. Univ. Souk-Ahras**
Guest :	**MEKHILEF Saad,**	**Pr. Univ. of Malaya, Malaysia**

الجمهوريـــة الجزائريـــة الديمقراطيـــة الشعبيـــة
وزارة التعليم العالي و البحث العلمي

BADJI MOKHTAR- ANNABA UNIVERSITY
UNIVERSITE BADJI MOKHTAR - ANNABA

جامعة باجي مختار- عنابـة

Faculté: Sciences de l'ingéniorat
Département: Electrotechnique

Année : 2018

THÈSE

Présentée en vue de l'obtention du diplôme de Doctorat en Science

Intitulé

Commande tolérante aux défauts des processus énergétiques

Option : Commande Electrique

Par : BOUTASSETA Nadir

Directeur de Thèse : RAMDANI Messaoud Professeur Université Badji-Mokhtar Annaba

Devant le Jury :

Président:	LABAR Hocine,	Pr. Univ. Annaba
Examinateurs :	LACHOURI Abderezzak,	Pr. Univ. Skikda
	KHELIL Khaled,	Pr. Univ. Souk-Ahras
Invité :	MEKHILEF Saad,	Pr. University of Malaya, Malaysia

Acknowledgment

Thanks to Allah first and foremost.

Thanks to my parents, wife and family members for their support and patience.

I would like to give the most sincere thanks to Prof. Messaoud Ramdani and Prof. Saad Mekhilef. I am grateful for their guidance and support in my research work.

Thanks to Prof. Labar Hocine, Prof. Khelil Khaled and Prof. Lachouri Abderezzak for accepting to be part of the scientific examination committee.

Thanks to Ammar Neçaibia, Ahmed Bouraiou, Samir Hassani and Oussama Guernine for their support and encouragements. Thanks to the members of: Unit of Research in Renewable Energy in Saharan Region (URER-MS/CDER)-Adrar-Algeria, Unit of Research in Advanced Materials (URMA/CRTI)-Annaba-Algeria, Power Electronic and Renewable Energy Laboratory (PEARL), Kuala Lumpur, Malaysia.

ملخص

يتطرق هذا العمل لموضوع التحكم في الأنظمة الطاقوية مع وجود خلل، حيث يكمن الهدف منه في إستيعاب الأعطاب عن طريق تصميم نظام تحكم يأخذ بعين الإعتبار وجود الخلل الداخلي و الإختلال الوظيفي الناتج من الوسط الخارجي.

تتميز الأنظمة الطاقوية بارتباط أدائها الوظيفي بمردودها الطاقوي، إذ إن المردود الكلي ناتج من جمع مردود العمليات الطاقوية الجزئية التي تحقق الهدف المشترك والمتمثل في إنتاج الطاقة في شكلها النهائي. كما أن مراقبة هذه العمليات واستيعاب الأعطاب تسمح في تحسين المردود الفردي لكل عملية والمساهمة في تحقيق الهدف الرئيسي المتمثل في تحسين الأداء الوظيفي الكلي.

تجدر الإشارة في هذا السياق إلى أن العمليات الطاقوية المنتجة للطاقات المتجددة تتصف بارتباطها وتأثرها بالظروف المناخية بالإضافة إلى تعرضها بشكل المباشر للوسط الخارجي، مما ينتج عن ذلك ظهور أعطاب مختلفة ووجود خلل في عمل أنظمتها. نتطرق في هذا العمل بالتحديد لأنظمة توليد الطاقات المتجددة الضوئية لهيمنتها على القدرة الإنتاجية الحالية للطاقات المتجددة الكهربائية، حيث نقوم بتحليل نوع العطب في عمل الأنظمة ونقترح نظام تحكم يتحمل وجود خلل في النظام للمساهمة في تحسين مردود العمليات الطاقوية. يتم إعادة تشكيل المتحكم ليحول بين طريقة معدلة للتحسين بالسرب تستعمل التيار الكهربائي و خوارزمية الموصلية التدريجية. بالإضافة إلى أن التقنية المقترحة تم تطبيقها عمليا للتحقق من كفاءة عملها في ظروف حقيقية بالمقارنة مع التقنيات التقليدية.

كلمات مفتاحية: التحكم في وجود خلل، أنظمة طاقوية، طاقة متتجددة، طاقة ضوئية، بحث عن النقطة القصوى، التحسين بالسرب.

Abstract

This work deals with the control of energy systems subject to faults. The objective is to accommodate faults by the design of a control law that takes into account the existence of internal faults and dysfunctions caused by external environment.

Energy systems are characterized by the dependence of their performance on energy efficiency, the total efficiency is the result of the operation of elementary energy processes to verify the final objective which is the production of energy in its final form. The supervision of these processes and tolerance to faults allow the improvement of individual performances and the achievement of global efficiency at a lower cost.

In this context, renewable energy conversion processes are characterized by the aspect of their dependence on climatic conditions and direct exposure to outdoor environment, resulting in the occurrence of different types of faults and dysfunctions. Solar photovoltaic renewable energy generation systems are considered in this work as they dominate renewable electricity capacity expansion. The study of the effect of various abnormal events and degraded operating modes of solar photovoltaic systems is performed and a fault-tolerant control law is proposed to enhance the efficiency of these energy processes. A reconfiguration of controller is designed to switch between an improved current-based particle swarm optimization technique and the incremental conductance algorithm. Practical implementation of the proposed approach shows excellent performance in real operating conditions when compared to traditional maximum power point algorithms.

Keywords: fault-tolerant control, energy systems, renewable energy, solar energy, photovoltaic, maximum power point tracking, particle swarm optimization,

Résumé

Ce travail traite le sujet de la commande des systèmes énergétique en présence de défauts. L'objectif est d'accommoder les défauts par la synthèse d'une loi de commande qui prend en charge l'existence des défauts internes et des dysfonctionnements causés par l'environnement externe.

Les systèmes énergétiques sont caractérisés par la dépendance de leurs performances au rendement énergétique; le rendement total est le résultat des rendements des processus énergétiques élémentaires réalisant l'objectif final étant produire une énergie propre et de bonne qualité sous différentes conditions et charges variables. La supervision de ces processus et la tolérance aux défauts permettent l'amélioration des rendements individuels et la contribution à la réalisation des objectifs en termes de performances globales.

Dans ce contexte, les procédés de conversion des énergies renouvelables sont caractérisés par leur dépendance des conditions climatiques et de l'environnement externe ce qui engendre des défauts et dysfonctionnements. Les systèmes de génération des énergies renouvelables photovoltaïques sont considérés puisqu'ils dominent la capacité actuelle de génération de l'électricité renouvelable, une analyse des anomalies et fonctionnements dégradés est réalisée et une loi de commande tolérante aux défauts est proposée pour améliorer le rendement de ses processus énergétiques. La reconfiguration du contrôleur est réalisée par la commutation entre une version modifiée de la technique d'optimisation par essaim de particules en utilisant le courant électrique et l'algorithme de conductance incrémentale. Une implémentation pratique est réalisée pour valider l'efficacité de la technique développée dans des conditions réelles en la comparant avec les méthodes classiques.

Mot-clés : Commande tolérante aux défauts, systèmes énergétiques, énergie renouvelable, énergie solaire, photovoltaïque, recherche du point extrémal, optimisation par essaim de particules.

Contents

List of Figures

List of Tables

List of Abbreviations

ADC	**A**nalog to **D**igital **C**onverter
CCS	**C**ode **C**omposer **S**tudio
DCF	**D**iagonal **C**anonical **F**orm
DSC	**D**igital **S**ignal **C**ontroller
DSP	**D**igital **S**ignal **P**rocessor
FDI	**F**ault **D**etection and **I**solation
FTC	**F**ault **T**olerant **C**ontrol
ICPSO	**I**mproved **C**urrent-based **P**articule **S**warm **O**ptimization
IncCond	**Inc**remental **Cond**uctance
I-V	**C**urrent-**V**oltage
LQR	**L**inear **Q**uadratic **R**egulator
MPP	**M**aximum **P**ower **P**oint
MPPT	**M**aximum **P**ower **P**oint **T**racking
P-I	**P**ower-**C**urrent
P&O	**P**erturb & **O**bserve
PSO	**P**articule **S**warm **O**ptimization
PV	**P**hoto**V**oltaic
P-V	**P**ower-**V**oltage
STC	**S**tandard **T**est **C**onditions
SVD	**S**ingular **V**alue **D**ecomposition

Physical Constants

Electron charge	$q = 1.602\,176\,62 \times 10^{-19}\,\mathrm{C}$
Boltzmann constant	$k = 1.380\,648\,52 \times 10^{-23}\,\mathrm{J/K}$
STC Irradiation	$G = 1000\,\mathrm{W/m^2}$
STC Temperature	$T = 25\,^{\circ}\mathrm{C}$

List of Symbols

G	incident solar irradiation	W/m^2
I_0	photovoltaic cell saturation current	A
I_{pv}	photovoltaic cell, panel, array static output current	A
i_{pv}	photovoltaic cell, panel, array dynamic output current	A
I_{sc}	short-circuit current	A
R_s	photovoltaic cell series resistance	Ω
R_p	photovoltaic cell parallel resistance	Ω
r_{pv}	photovoltaic array dynamic resistance	Ω
T	photovoltaic cell temperature	°C
T_s	sampling time	s
T_{sw}	switching period in pwm signal	s
V_{oc}	open-circuit voltage	V
V_{pv}	photovoltaic cell, panel, array static output voltage	V
v_{pv}	photovoltaic cell, panel, array dynamic output voltage	V

Chapter 1

Introduction

1.1 Motivation and background

Modern energy systems depend on the availability and correct operation of complex interconnected processes. The occurrence of faults or malfunctions in components may affect the overall performance of the installation and lead to a considerable energy loss. The increased demand for productivity, high performance and efficiency in energy production facilities has led to the development of sophisticated control systems in order to meet with the challenging reliability and safety requirements.

Renewable energy sources are the alternative solution for securing future energy needs as they are characterized by reduced environmental effects and effective use in isolated areas which are outside the reach of public electricity supply. The reliability of solar Photovoltaic (PV) renewable energy generation systems becomes an important issue as it dominates the renewable electricity capacity expansion [1]. The exposure of PV arrays to the outdoor environment results in a disturbed operation caused mainly by variable weather conditions and components degradation [2],[3].

PV arrays are subject to various types of faults that affect their normal operation and lead to a considerable energy loss. Degradation symptoms of PV panels have been studied to identify different sources of faults. The effect of a parasitic resistance on the performance of PV modules was investigated in [4], the variations in series and parallel resistances may be a sign of possible aging of PV modules. Such degraded panels may cause a general mismatch fault on the whole PV array. Mismatching fault occurs when the electrical parameters of one module are different from that of the remaining modules in a given PV installation, this fault is the most common in PV systems and may cause irreversible damage [5]. Partial shading, which is basically an undesirable operating condition, can be considered as a particular case of the mismatch fault. It arises when a number of PV modules are subject to a different level of solar irradiation from the rest of the installation, such temporary fault was studied extensively in the literature [6], [7], [8]. Wiring-related faults are common in electric circuits, there are mainly two types of faults in PV-based installations: Line-to-Ground and Line-to-Line faults. In [9], the line-ground fault was studied only on the AC side of the PV system, whereas the authors in [10], [11] investigated its effect on the DC side. Line-to-line fault occurs when a short-circuit between the cables of two or more PV modules with different potential is detected [12].

To mitigate the effect of such issues, fault detection and identification (FDI) methods have been proposed to monitor the state of the PV system and warn the user of degradation signs of the PV array and any other unexpected change in the systems' normal operation[13], [14]. Furthermore, FDI techniques allow the detection of wiring-related faults that may not be detected in some conditions using conventional over-current protection devices [15]. In [16], a review of fault diagnosis methods on the DC side of PV arrays is given, some of the methods take into account only detection of faults and some of them make both detection and classification. In this work we consider all the presented types of faults but we take into account only fault detection, as fault classification will not have much impact on the fault tolerant control algorithm.

On the other hand, the nonlinear nature of the Power-Voltage (P-V) characteristic curve of PV cells has made the control procedure more difficult [17]. Many maximum power point tracking (MPPT) algorithms were developed to extract maximum power from PV panels by searching the nonlinear curve for the optimal operating point [18], [19], [20]. The first algorithm that has been proposed is the Perturb & observe (P&O) algorithm, this algorithm searches the P-V curve for the maximum power point (MPP) by perturbing the actual operating point of the PV system and analyzing its effect on the output power until it reaches the optimal operating point [21]. Such periodic change in the reference value generates oscillations around the maximum power point. The amplitude of the oscillations can be reduced by choosing a variable step perturbation [22]. The limitations of this method in the case of a sudden change in solar irradiation stimulated more research work on MPPT algorithms [18], [19]. Most of the proposed methods deal with the problem of sudden change in solar irradiation [23], and some of them manage to control the PV module in the case of partial shading [24], [25], [26]. In the PSO-based MPPT algorithm proposed in [27] to control PV arrays under partial shading, the authors used the voltage variable as a particle in the particle swarm optimisation procedure; this approach slows the convergence of the algorithm because of the large space of search that extends to the open-circuit voltage. In [24], the duty cycle is chosen to track the global MPP by eliminating the need for a regulator in the PSO-based MPPT algorithm. Such choice may lead the PV system to undesirable operating regions given that it lacks direct correspondence with the physical system, and degraded performance in normal operating conditions given the absence of a voltage or current regulation in addition to low robustness in the presence of load change. Fault tolerance in PV panels was the subject of the research work in [29] and [28] , where the authors propose a reconfiguration mechanism of the PV cells in order to bypass the faulted ones, to the extent of our knowledge this is the only work that was reported on the topic.

1.2 Objective and contributions

The objective of this thesis is to design a fault tolerant power extraction strategy that will supervise the operation of PV arrays and reconfigure the control law to manage a suboptimal operation of the faulted system. The proposed strategy is based on the reconfiguration of the controller, the designed algorithm switches between an Improved Current-based PSO (ICPSO) and the Incremental Conductance (IncCond) algorithm [30].

- The ICPSO MPPT procedure gives reduced search space for the optimization process.
- A convergence criterion is added to guarantee its stability and improve its transient performance.
- A switching mechanism is designed which allows smooth transitions between the algorithm designed for fault-free condition and the Improved Current-based PSO (ICPSO) designed for faulted operating conditions.
- The proposed control strategy is also proven to be robust to load variations that may affect the FDI algorithm detection mechanism.

1.3 Thesis organization

This thesis is organized as follows:

- **Chapter 2:** The model of the PV array is developed based on the model of the PV cell. The effect of environmental conditions such as temperature and irradiation are analyzed. The effects of wiring faults, mismatch and partial shading on the characteristic curves of the PV array are given.
- **Chapter 3:** The control of the PV array operating point using a boost DC-DC converter is detailed. The design of the controller is based on the state space model of the small signal model of the DC-DC converter. The maximum power point tracking algorithms is applied to guide the PV array to its Maximum Power Point. Different MPPT approaches are presented.

- **Chapter 4:** The fault-tolerance to sensor faults is applied in the case of an offset in the PV current sensor. A more general strategy that takes into account the wiring-related faults in addition to partial shading and the mismatch fault is developed. Simulations are carried out to show the performance of the proposed algorithm compared to a base-line MPPT algorithm.

- **Chapter 5:** Experimental results resulting from the implementation of the proposed approach on a TMS320F28335 DSP microcontroller to control a developed prototype of a boost DC-DC converter that is used to adjust the operating point of a PV array simulator. The results of the application of the fault-tolerant strategy when the characteristic curves of the studied faults are implemented in the PV array simulator demonstrate the considerable gain in power compared to classical algorithms.

- **Chapter 6:** Conclusions and perspectives are given in this chapter.

Chapter 2

Modeling and fault analysis of PV energy conversion systems

2.1 Introduction

The generation process of energy based on the photovoltaic (PV) effect converts incident sunlight into electric energy. PV cells are the most basic energy conversion element that constitutes the building block of a PV panel. Thus, the modeling and proper characterization of the PV cell are required to better understand the conversion process and the evaluation of the behavior of PV systems in various operating conditions. Simulations of the effect of components faults and environmental influence on operating performance may be then realized.

2.2 Models of photovoltaic cell, panel and array

The combination of photovoltaic cells in series composes PV panels (modules) see figure 2.1. When connected in series and equipped with bypass and blocking diodes, PV panels form a PV string. A PV array is composed with the combination of parallel PV strings. The back-fed current is prevented by the use of blocking diodes. The bypass diodes are activated in the case of faulted PV modules to allow the string to produce power and to prevent hot spots that may permanently damage the PV panels.

Electric circuit-based models were proposed in the literature to mimic the

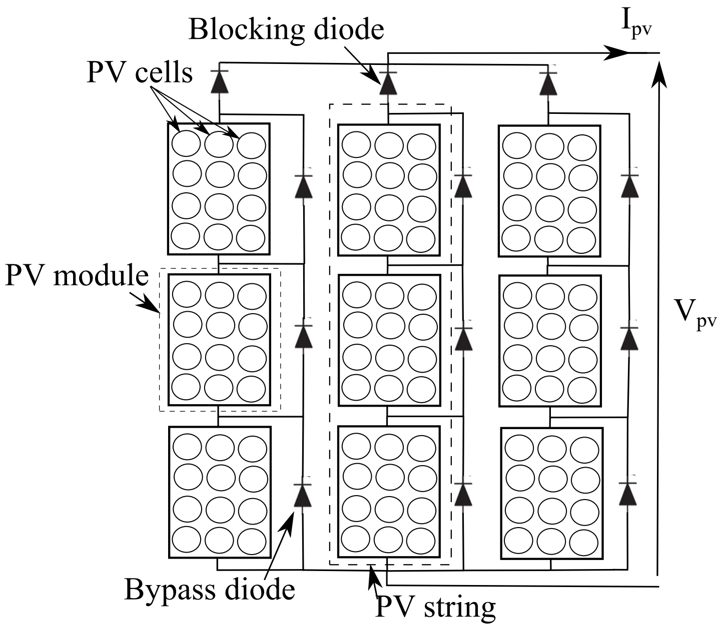

FIGURE 2.1: PV array components.

experimental current-voltage (I-V) curve of the PV cell [31],[32]. The practical model (also called one diode model) is known to have a good compromise between complexity and accuracy [33]. The one-diode equivalent circuit of

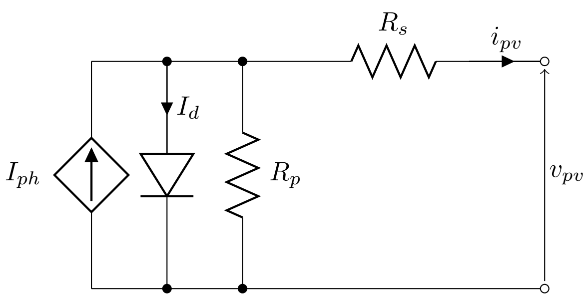

FIGURE 2.2: Equivalent electric circuit of a PV cell.

a PV cell as shown in figure 2.2 consists of a controlled current source I_{ph}, a diode traversed by a current I_d with series and shunt internal resistances R_s and R_p respectively. The controlled current source is dependent on the level of solar irradiation and the temperature of the cell surface as follows:

$$I_{ph} = (I_{ph,n} + K_I \Delta_T)\frac{G}{G_n} \tag{2.1}$$

Where $I_{ph,n}$ is the nominal generated current (given at nominal conditions: $(T = 25^oC$ and $G = 1000W/m^2)$, K_I is the short-circuit current/temperature coefficient, $\Delta_T = T - T_n$ (T and T_n are the current and nominal temperatures), G and G_n are the current and nominal irradiations. The current in the diode I_d is given by:

$$I_d = I_0 \left[exp\left(\frac{V + R_s I}{aV_t} \right) - 1 \right] \tag{2.2}$$

I_0 the saturation current of the diode is given as follows:

$$I_0 = \frac{I_{sc,n} + K_I \Delta_T}{exp\left(\frac{V_{oc,n} + K_V \Delta_T}{aV_t} \right) - 1} \tag{2.3}$$

Where $I_{sc,n}$ is the nominal short-circuit current, $V_{oc,n}$ is the nominal open-circuit voltage. K_V is the open-circuit voltage/temperature coefficient, a is a diode constant, V_t is the thermal voltage of the array: $V_t = N_s kT/q$, with N_s cells connected in series. k is the *Boltzmann* constant and q is the electron charge. R_s is the series resistance which depends on the material used to construct the PV cell, its effect is stronger in the voltage source operating region. R_p is the parallel resistance, its effect is stronger in the current source operating region.

For a PV array with N_{pp} parallel panels and N_{ss} series panels, the equivalent circuit is given in figure 2.3 and its output current is as follows:

$$i_{pv} = I_{ph} N_{pp} - I_0 N_{pp} \left[exp\left(\frac{v_{pv} + R_s \left(\frac{N_{ss}}{N_{pp}} \right) i_{pv}}{aV_t N_{ss}} \right) - 1 \right] - \frac{v_{pv} + R_s \left(\frac{N_{ss}}{N_{pp}} \right) i_{pv}}{R_p \left(\frac{N_{ss}}{N_{pp}} \right)} \tag{2.4}$$

The dynamic conductance g_{pv} is calculated by taking the derivative of eq. (2.4) with respect to voltage as follows [34],[35]:

$$g_{pv} = \frac{\partial i_{pv}}{\partial v_{pv}} = -\frac{I_0 N_{pp}}{a \cdot V_t \cdot N_{ss}} \cdot exp\left(\frac{v_{pv} + R_s \cdot \frac{N_{ss}}{N_{pp}} \cdot i_{pv}}{a \cdot V_t \cdot N_{ss}} \right) - \frac{1}{R_p \cdot \frac{N_{ss}}{N_{pp}}} \tag{2.5}$$

The dynamic resistance is then obtained from eq. (2.5):

$$r_{pv} = -\frac{1}{g_{pv}} \tag{2.6}$$

The linearized model around the operating point (I_{pv}, V_{pv}) is then given as follows [36]:

$$i_{pv} = G_{pv} \cdot v_{pv} + I_{pv} - G_{pv} \cdot V_{pv} \tag{2.7}$$

where $G_{pv} = g_{pv}(V_{pv}, I_{pv})$, is the static conductance.

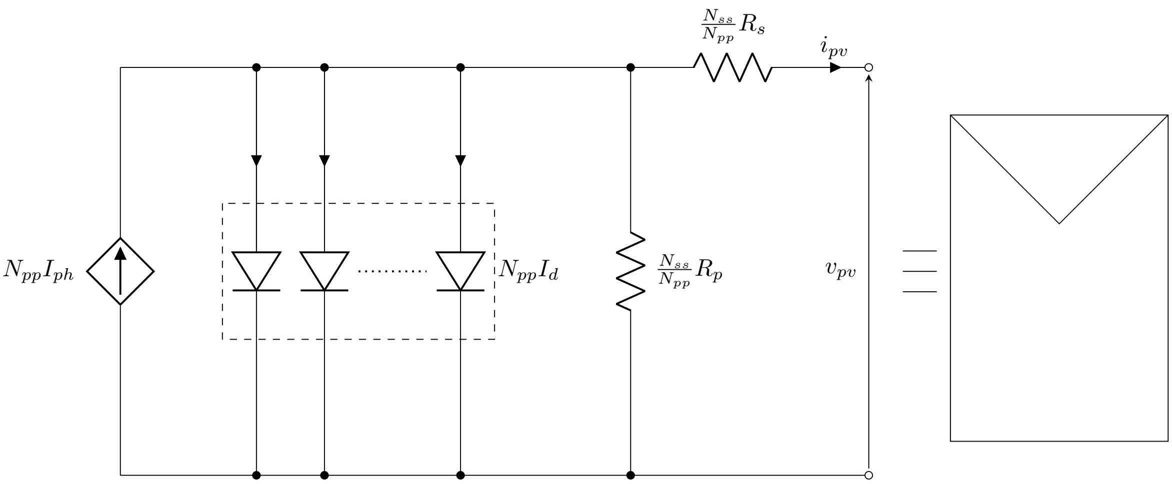

FIGURE 2.3: PV array equivalent circuit.

The parameters given in Table 2.1 are used in the consequent sections for the simulation of the PV array.

TABLE 2.1: MSX60 PV Panel characteristics

Parameter	Value
Maximum Power (P_{max})	60 W
Voltage at P_{max} (V_{mp})	16,8 V
Current at P_{max} (I_{mp})	3.56 A
Short-circuit current (I_{sc})	3.87 A
Open-circuit voltage (V_{oc})	21.0 V
Temp. coef. of I_{sc}	0.003 A/K
Temp. coef. of V_{oc}	$-0.008\ V/K$

2.3 Effect of environmental conditions on the operation of PV arrays

The electrical characteristics of PV arrays are directly affected by the variations in climatic conditions. The effect is noticed in the following particular operating points:

- The open-circuit operating point, characterized by zero output current $I_{pv} = 0$ and an open-circuit output voltage $V_{pv} = V_{oc}$.
- The short-circuit operating point, characterized by a zero output voltage $V_{pv} = 0$ and a short-circuit current $I_{pv} = I_{sc}$.
- The Maximum Power Point (MPP), characterized by an output current $I_{pv} = I_{MPP}$, an output voltage $V_{pv} = V_{MPP}$, and a maximum power extremum $\frac{\partial p_{pv}}{\partial v_{pv}} = \frac{\partial p_{pv}}{\partial i_{pv}} = 0$.

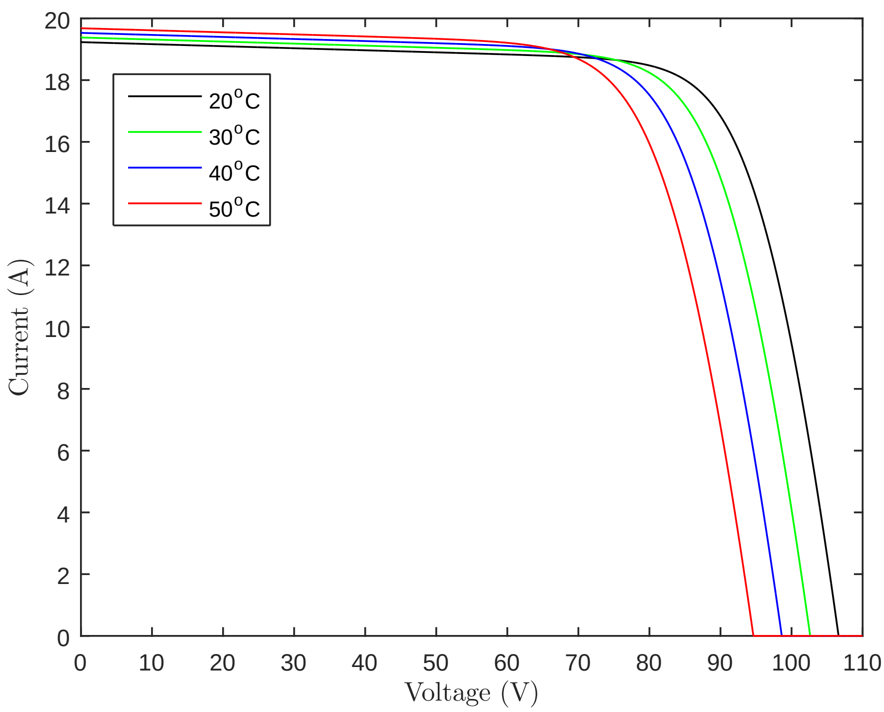

FIGURE 2.4: Effect of variable temperature on the I-V characteristic curve.

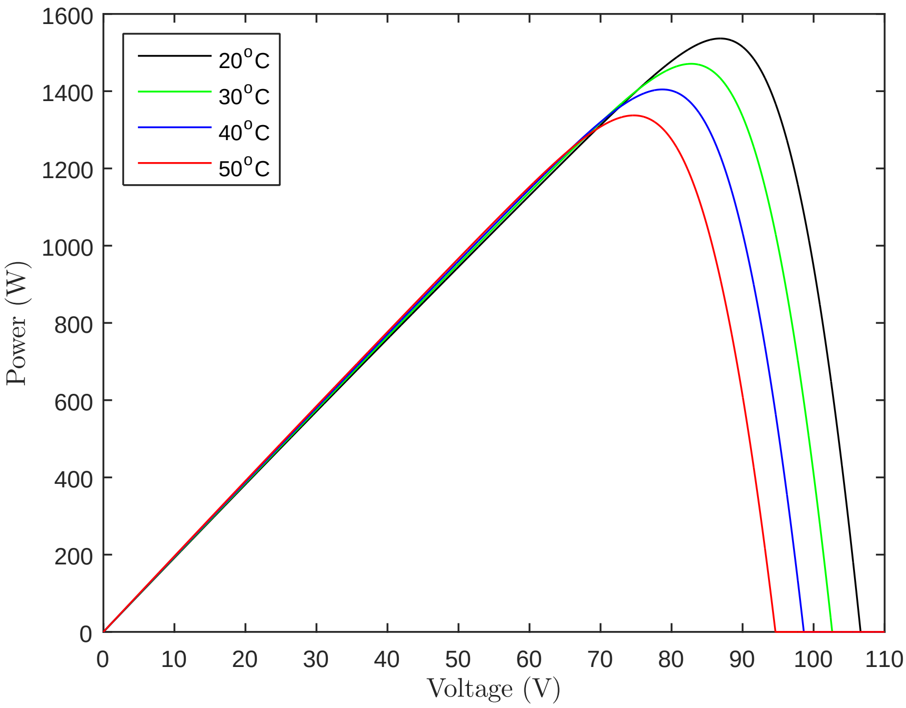

FIGURE 2.5: Effect of variable temperature on the P-V characteristic curve.

2.3.1 Effect of temperature variation

In addition to the incident solar irradiation, ambient temperature (T_a) affects the characteristic curves of PV arrays with a large variation of the open-circuit voltage V_{oc} compared to a minor change in short-circuit current I_{sc} in addition to the shifting of the MPP. The cell temperature is related to the ambient temperature with the following equation:

$$T = T_a + \frac{NOCT - 20}{800} \cdot G \tag{2.8}$$

where $NOCT$ is the Nominal Operating Cell Temperature at specific conditions ($G = 800W/m^2, T_a = 20^oC, wind = 1m/s$, open-circuit terminals with open back-side mounting). The effect of temperature's variation on the I-V characteristic curve is given in figure 2.4. The increase in temperature results in a lower open-circuit voltage V_{oc} and slightly higher short-circuit current I_{sc}.

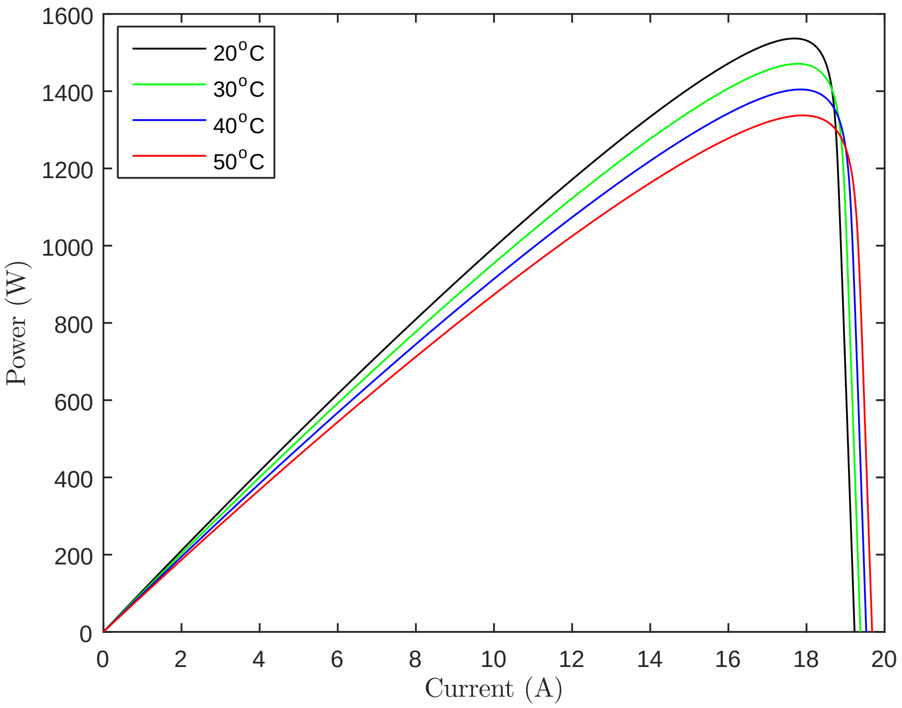

FIGURE 2.6: Effect of variable temperature on the P-I characteristic curve.

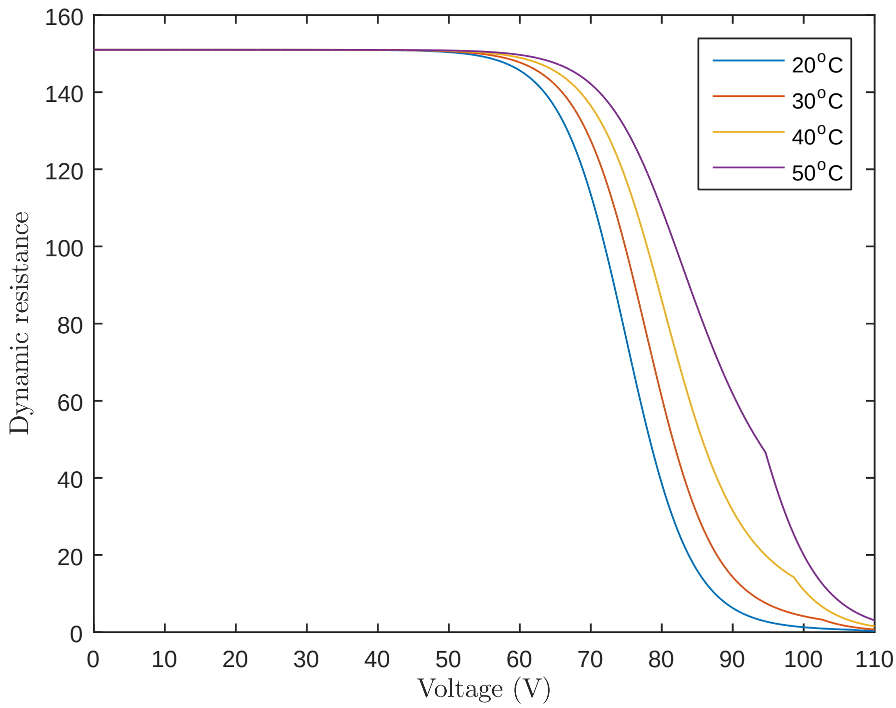

FIGURE 2.7: Effect of variable temperature on the dynamic resistance characteristic curve.

The P-V and P-I curves in figures 2.5 and 2.6 respectively show the effect of the variation of temperature on the performance of the PV array. The increase in temperature values results in a decreasing MPP (decreased performance) in addition to variations in open-circuit voltage and short-circuit current respectively. It is noticed that the voltage operating point of the MPP (V_{MPP}) changes with the variation of temperature (figure 2.5), whereas the current operating point of the MPP I_{MPP} have negligible change. The dynamic resistance is affected near the MPP region by the increase in temperature as shown in figure 2.7.

2.3.2 Effect of solar irradiation variation

The variation of solar irradiation is considered the main perturbing factor of PV energy conversion systems because it has faster dynamics compared with temperature and bigger influence on the PV output power. It affects mainly the short-circuit current I_{sc} of the PV array as shown in figure 2.8 with minor effect on the open-circuit voltage V_{oc}. The voltage operating point of the MPP is practically constant with irradiation change as shown in figure 2.9, whereas the current operating point of the MPP as shown in figure 2.10 changes with irradiation variation. The dynamic resistance remains practically unchanged as demonstrated in figure 2.11.

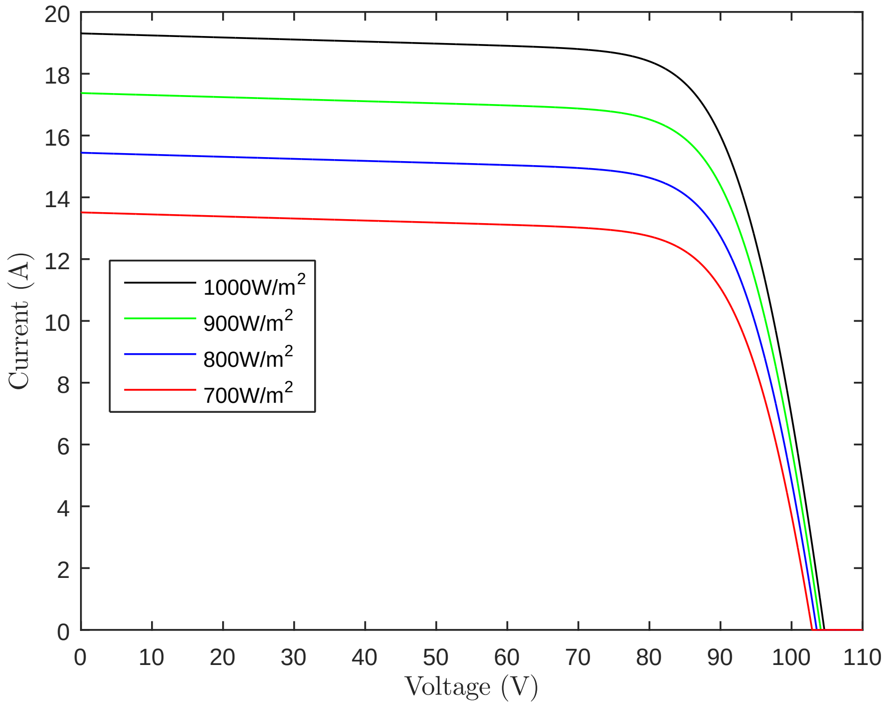

FIGURE 2.8: Effect of variable irradiation on the I-V characteristic curve.

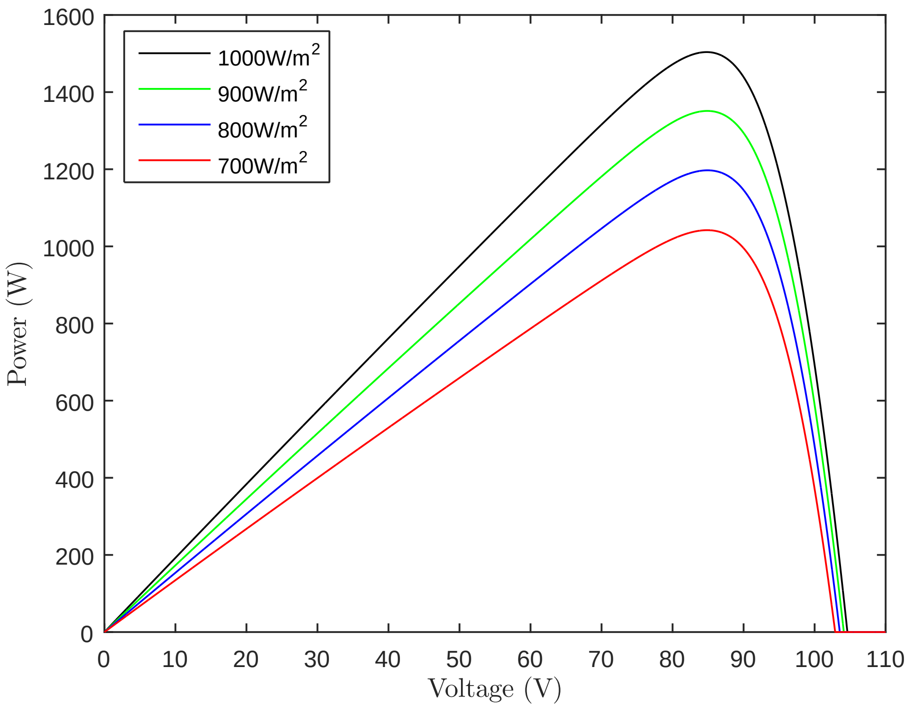

FIGURE 2.9: Effect of variable irradiation on the P-V characteristic curve.

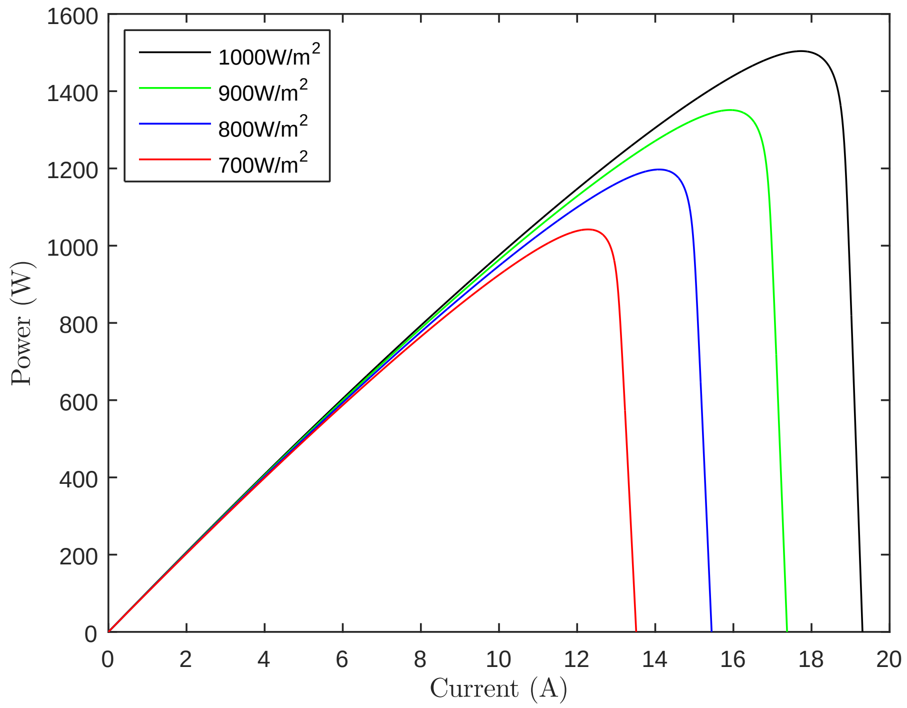

FIGURE 2.10: Effect of variable irradiation on the P-I characteristic curve.

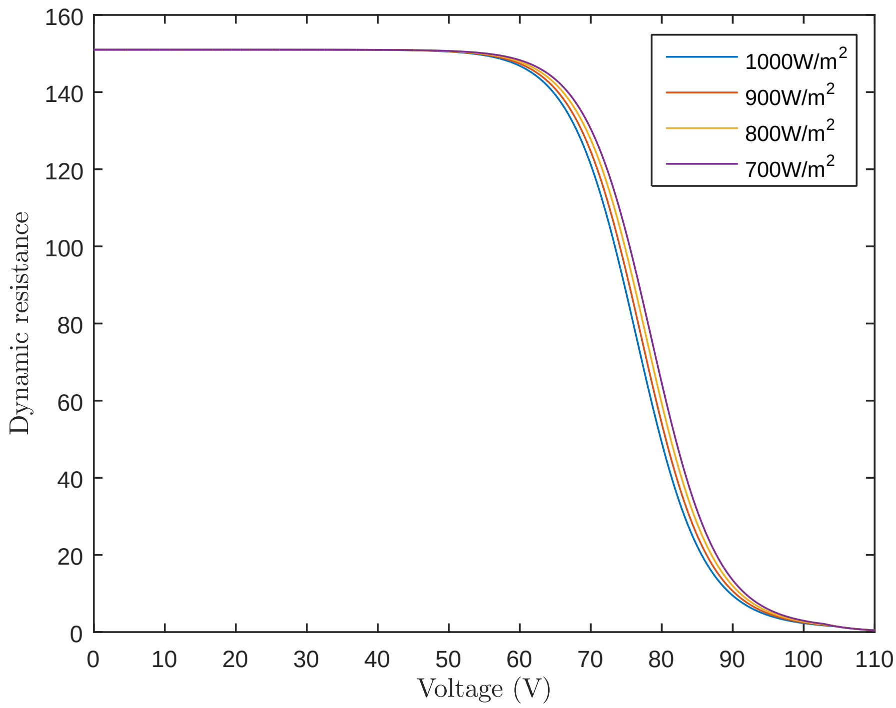

FIGURE 2.11: Effect of variable irradiation on the dynamic resistance characteristic curve.

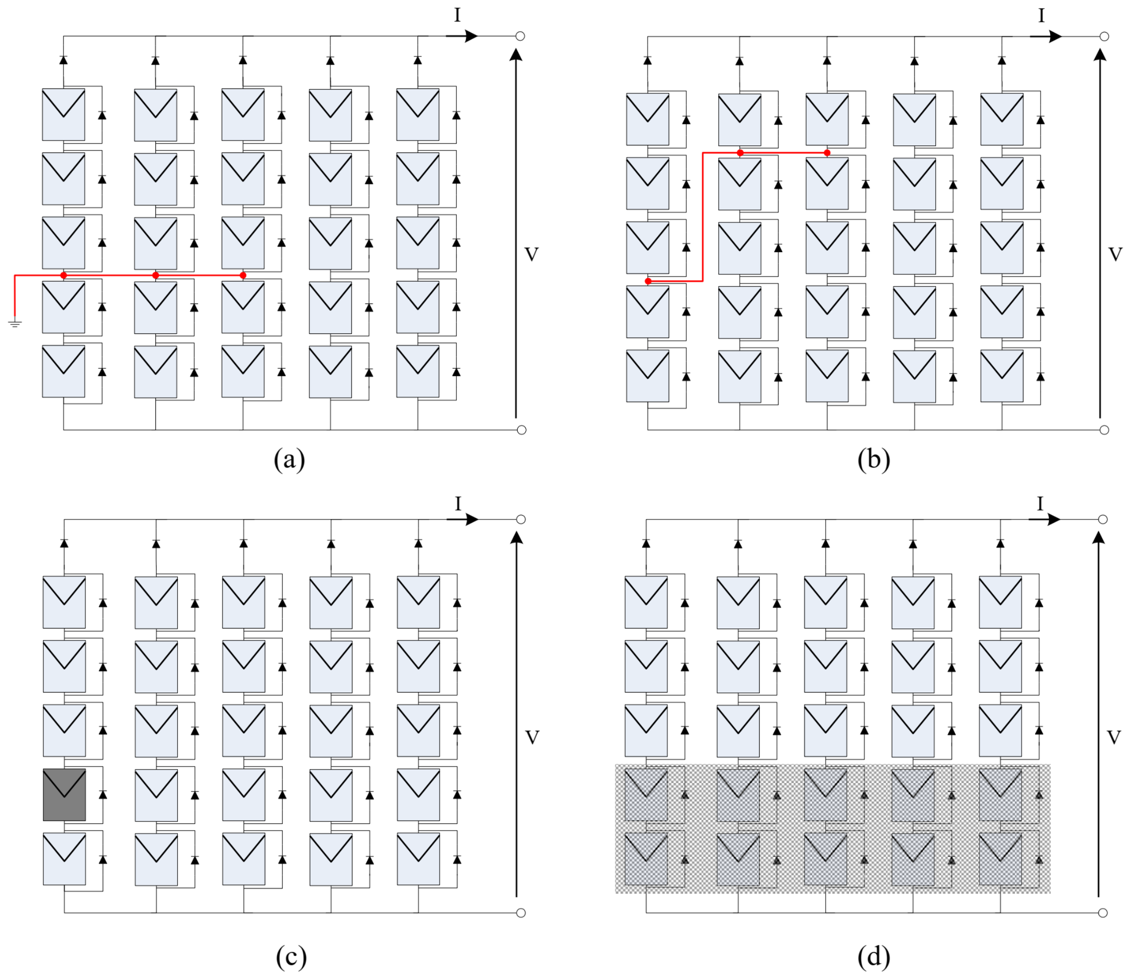

FIGURE 2.12: Configurations of the studied faults on the PV array : (a) Line-Ground, (b) Line-Line fault, (c) Mismatch fault, (d) Partial shading fault

2.4 Effect of faults on the operation of PV arrays

2.4.1 Grounding of photovoltaic arrays

Photovoltaic installation are composed of different parts constructed using electrically conductive materials (such as PV modules frames, mounting racks,...), which are subject to possible contact with insulated current carrying conductors when insulation is lost due to melting or other causes [37]. The grounding of such conducting parts is required to ensure safe operation in the case of the occurrence of such faults that exposes people or living animals to direct contact with hazardous voltage. Figure 2.13 shows the grounding of PV modules frames.

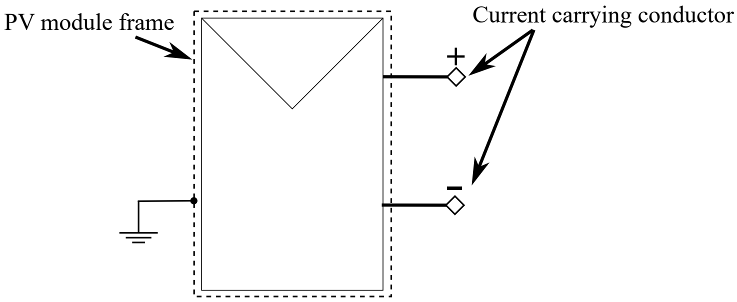

FIGURE 2.13: Grounding of PV arrays

2.4.2 The effect of Line-Ground fault

A line-ground fault is a short-circuit between a current carrying conductor (live line) and the ground. When we introduce this fault on the PV array as shown in figure 2.12 (a), the voltage given by the three strings of the PV array drops and causes a mismatch fault (strings with different output voltages) that affects the power-voltage curve of the whole PV array. Back-fed current to the faulted string is prevented by placing blocking diodes at the output of each string. The Power-Voltage (P-V) and the Current-Voltage (I-V) characteristic curves of the PV array under line-ground fault are given in figure 2.14 (a). The line-ground fault introduces multiple maximum power points on the P-V curve at different operating points. We note that the shape of the P-V curve changes with the configuration of the fault, the choice made in our case is justified by the presence of the lower MPP at the same operating point (voltage) as the MPP of the healthy array. In such situation, hill climbing based algorithms are trapped in a local extremum and fail to track the global MPP.

2.4.3 The effect of Line-Line fault

A line-line fault is a short-circuit between two current carrying conductors (two lines) in the PV array with different potentials. Line-line faults may be caused by the failure of insulation in the current carrying conductors, short-circuit faults within the PV junction-box due to mechanical damage, water

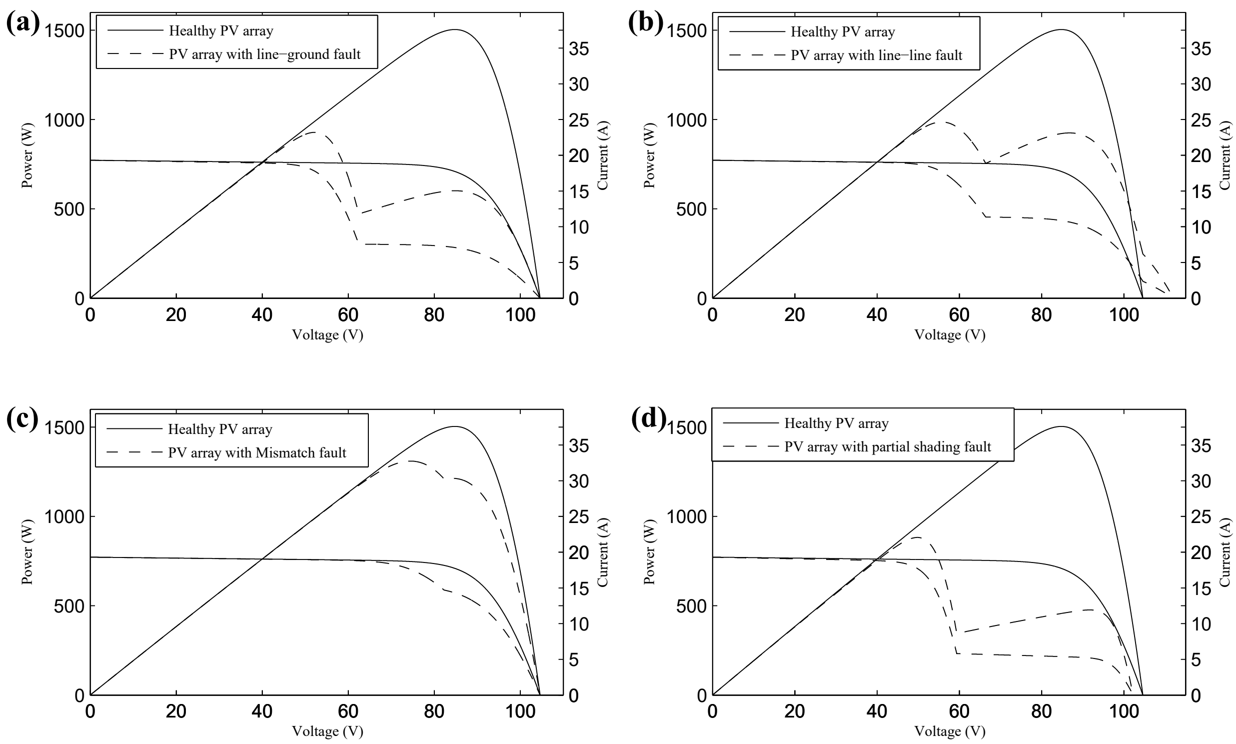

FIGURE 2.14: Effect of faults on the PV array: (a) Line-Ground, (b) Line-Line fault, (c) Mismatch fault, (d) Partial shading fault

ingress and corrosion, or double ground faults at the same time in the PV array. We introduce a line-line fault on the same previous healthy PV array; a short-circuit between the cables of three strings, as shown in figure 2.12 (b). The P-V curve of the faulted PV array in figure 2.14 (b) is characterised by the presence of multiple power points. In addition, the open-circuit voltage of the PV array has changed due to the line-line fault. This effect can be explained by the modification of the PV array circuit configuration caused by the line-line fault as illustrated in figure 2.12 (b).

2.4.4 The effect of mismatch fault

A mismatch occurs when PV cells connected in series produce lower current than the remaining cells making faulted cells dissipate power. Such effect creates a hot-spot in the PV module and may cause irreversible damage [5]. A mismatched cell is characterized by an increased series resistance and decreased shunt resistance [4]. The mismatched module affects the output power of the PV array and leads to a general performance degradation. The effect of this type of fault on the PV array is presented in figure 2.14 (c) where we introduced a mismatched module in the first string of the PV array as shown in figure 2.12 (c). The series resistance of the mismatched cell is chosen to be ($R_s^{mis} = 100 \cdot R_s$). The shunt (parallel) resistance of the mismatched module is chosen as follows ($R_p^{mis} = R_p/100$).

2.4.5 The effect of partial shading

Partial shading is considered as a common fault in PV arrays that is caused by front surface soiling of the PV cells, snow, leafs, shading of adjacent buildings...etc. The shaded cell generates less current than the other cells in series in the same string, the current imposed by the string causes over-heating of the cell that is commonly called "Hot Spot". To prevent hot spots caused by a partial shading on a PV panel, bypass diodes are added to strings allowing the current to flow through them bypassing the shaded module. The negative effect of such protection components is the introduction of multiple power points in the P-V curve as shown in figure 2.14 (d). The lower part of the PV array was partially shaded by exposing the panels to less solar irradiation ($300W/m^2$) whereas the remaining panels receive full irradiation ($1000W/m^2$) (see figure 2.12 (d)).

2.4.6 Fault analysis summary

In Table 2.2, a summary of the effect of the studied faults on the output power of the PV array is given. Multiple power points are present in the P-V curves of the faulted PV arrays. The obtained results show the amount of power loss caused by the presence of faults on the PV installation. The worst case is the partial shading fault where a power loss of 41.32% is noted for the global MPP (MPP1), and 68.29% for the local MPP (MPP2). The design of an effective MPPT algorithm is expected to increase the efficiency of PV arrays in such conditions.

TABLE 2.2: Maximum Power Points (MPP) of the faulted PV array

PV Array	Local MPP1		Local MPP2		Global MPP	
	$I_{pv}(A)$	$P_{pv}(W)$	$I_{pv}(A)$	$P_{pv}(W)$	$I_{pv}(A)$	$P_{pv}(W)$
Healthy PV Array	-	-	-	-	17.73	1504
Line-Ground fault	17.78	928.46	7.09	601.61	17.78	928.46
Line-Line fault	17.70	986.40	10.66	925.20	17.70	986.40
Mismatch fault	17.59	1310	14.43	1213.70	17.59	1310
Partial Shading fault	17.71	882.5	5.20	476.83	17.71	882.5

2.5 Summary

Photovoltaic arrays are characterized by a nonlinear current-voltage (I-V) characteristic curve. The shape of the I-V (and consequently P-V) curve changes with environmental conditions such as variable temperature and irradiation and also in the presence of abnormal operating conditions such as the partial shading and short-circuits in wirings. These changes result in the shifting of the maximum power operating point and in some cases the presence of multiple maximum power points with different power ratings. The PV system must then be equipped with operating point control interface that allows the tracking in real-time of the optimal maximum power point.

Chapter 3

Control and maximum power extraction of PV systems

3.1 Introduction

The dependence of photovoltaic arrays on the variation of the uncontrollable temperature and solar irradiation variables in addition to the different environmental and component induced faults lets the Maximum Power Point (MPP) vary in a wide range. Consequently, the operating point of the PV array has to be controlled to track the varying MPP. A power conversion stage between the PV source and the load is needed to dynamically optimize the operating point of the source to match the actual MPP. DC-DC switching regulators are commonly used to accomplish such task with high efficiency and application dependent architectures.

3.2 Dynamic Model of the boost DC-DC converter

The DC-DC switching converter illustrated in figure 3.1 is a step-up boost converter, which is characterized by an output voltage higher than the input voltage. Such conversion is usually needed in PV arrays with low output voltage that has to be increased in order to be synchronized with the grid voltage. The dynamic behavior of the power conversion stage is essential in order to design an effective MPPT algorithm.

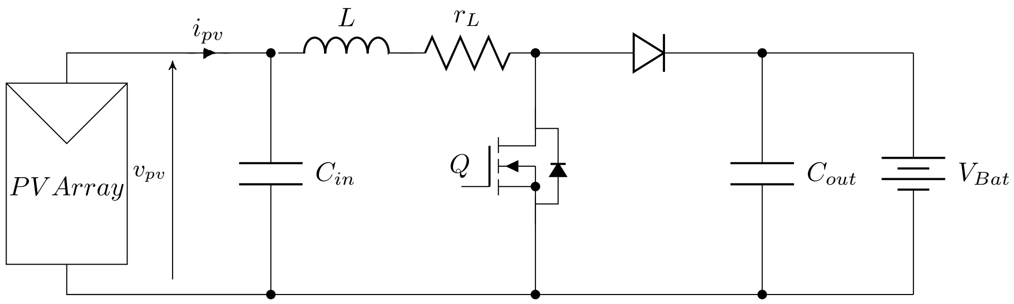

FIGURE 3.1: PV array and boost DC-DC converter association.

3.2.1 State space model of the boost DC-DC converter

The dynamic model of the boost DC-DC converter is obtained by applying the small signal approximation which consists of a small perturbation of the converter variables around static linear operating points. The model is developed by applying Kirchoff's laws for the circuit shown in figure 3.1 when the controlled switch Q is conducting ('ON' state) and when it is in open circuit condition ('OFF' state). The obtained model is nonlinear as it switches between two linear models depending on the state of Q. When the switch Q is 'ON' (closed) the circuit in figure 3.1 becomes as the circuit in figure 3.2, the following equations 3.1 are obtained:

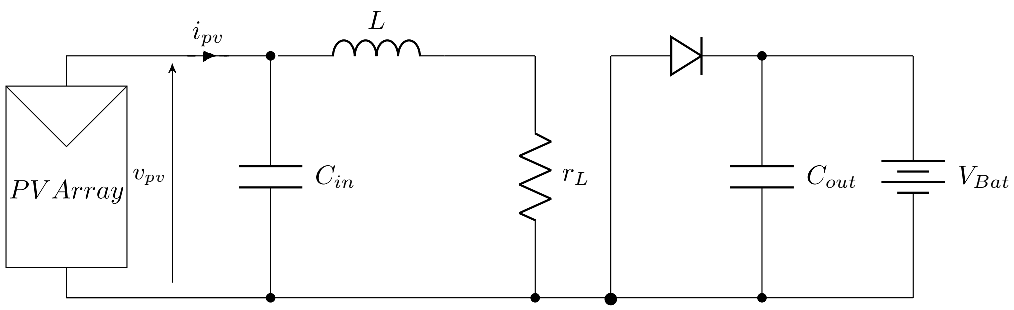

FIGURE 3.2: PV array and boost DC-DC conerter: 'ON' state.

$$\begin{cases} v_L(t) = v_{pv}(t) - r_L \cdot i_L(t) \\ i_{C_{in}}(t) = i_{pv}(t) - i_L(t) \\ i_{C_{out}}(t) = -i_o(t) \\ v_{C_{out}}(t) = V_{Bat} \end{cases} \tag{3.1}$$

Where v_L and i_L are the inductor dynamic voltage and current respectively and r_L is its internal resistance, v_{pv} and i_{pv} are the PV array dynamic output voltage and current respectively, i_o and V_{Bat} are the converter dynamic output current and voltage, i_{Cout} and v_{Cout} the output capacitor dynamic current and voltage respectively.

The time varying variables may be represented as the DC component added to the ripple resulting from the high frequency switching. In the small ripple approximation, the magnitude of the high frequency switching ripple is supposed to be much smaller that its DC component.

By using the small ripple approximation the system 3.1 becomes as follows:

$$\begin{cases} V_L = V_{pv} - r_L \cdot I_L \\ I_{C_{in}} = I_{pv} - I_L \\ I_{C_{out}} = -I_o \\ V_{C_{out}} = V_{Bat} \end{cases} \tag{3.2}$$

When the switch Q is 'OFF' (open) the circuit in figure 3.1 becomes as the circuit in figure 3.3, then the following equations are valid:

$$\begin{cases} v_L(t) = v_{pv}(t) - r_L \cdot i_L(t) - V_{fw} - V_{Bat} \\ i_{C_{in}}(t) = i_{pv}(t) - i_L(t) \\ i_{C_{out}}(t) = i_L(t) - i_o(t) \\ v_{C_{out}}(t) = V_{Bat} \end{cases} \tag{3.3}$$

Using the small ripple approximation, the equations become as follows:

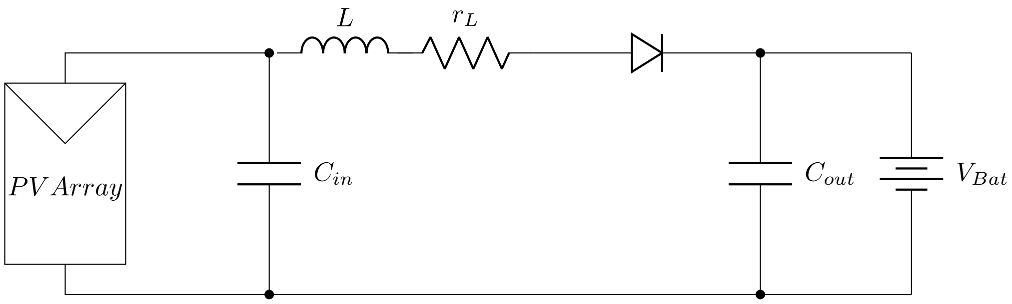

FIGURE 3.3: PV array and boost DC-DC conerter: 'OFF' state.

$$\begin{cases} V_L = V_{pv} - r_L \cdot I_L - V_{fw} - V_{Bat} \\ I_{C_{in}} = I_{pv} - I_L \\ I_{C_{out}} = I_L - I_o \\ V_{C_{out}} = V_{Bat} \end{cases} \tag{3.4}$$

Where V_{fw} is the forward voltage of the conducting diode.
The inductor volt-second balance $\int_0^{T_s} V_L = 0$ is then applied as follows:
$\int_0^{T_s} V_L = D \cdot T_s(V_{pv} - r_L \cdot I_L) + D' \cdot T_s(V_{pv} - r_L \cdot I_L - V_{fw} - V_{Bat}) = 0$

$$D(V_{pv} - r_L \cdot I_L) + D'(V_{pv} - r_L \cdot I_L - V_{fw} - V_{Bat}) = 0 \tag{3.5}$$

Knowing that $D + D' = 1$, the equation 3.5 becomes:

$$V_{pv} - r_L \cdot I_L - D'(V_{fw} + V_{Bat}) = 0 \tag{3.6}$$

$$V_{pv} - r_L \cdot I_L = D'(V_{fw} + V_{Bat}) \tag{3.7}$$

The capacitor charge balance gives the following condition $\int_0^{T_s} I_{C_{in}} = 0$ for the capacitor C_{in}.

$$\int_0^{T_s} I_{C_{in}} = D \cdot T_s(I_{pv} - I_L) + D' \cdot T_s(I_{pv} - I_L) = 0 \tag{3.8}$$

$$I_{pv} = I_L \tag{3.9}$$

When capacitor current balance is applied for C_{out} the following equation is obtained:

$$\int_0^{T_s} I_{C_{out}} = D \cdot T_s(-I_o) + D' \cdot T_s(I_L - I_o) = 0 \tag{3.10}$$

$$-I_o + D' \cdot I_L = 0 \tag{3.11}$$

$$I_o = D' \cdot I_L \tag{3.12}$$

Next we use small signal approximation to obtain the dynamic model of the boost DC-DC converter:
$v_L(t) = L \cdot \frac{di_L(t)}{dt} = d(t)(v_{pv}(t) - r_L \cdot i_L(t)) + d'(t)(v_{pv}(t) - r_L \cdot i_L(t) - V_{fw} - V_{Bat})$
By taking into consideration $d(t) + d'(t) = 1$ we find the following:
$L \cdot \frac{di_L(t)}{dt} = v_{pv}(t) - r_L \cdot i_L(t) - d'(t)(V_{fw} + V_{Bat})$
The small signal approximation supposes that the nonlinear model of the converter is linearized around a quiescent operating point. The nonlinear model is approximated by perturbing the actual static operating point as follows:

$$\begin{cases} i_L(t) = I_L + \hat{i}_L(t) \\ v_{pv}(t) = V_{pv} + \hat{v}_{pv}(t) \\ d(t) = D + \hat{d}(t) \end{cases} \tag{3.13}$$

$$d'(t) = 1 - d(t) = 1 - (D + \hat{d}(t)) = 1 - D - \hat{d}(t) = D' - \hat{d}(t) \tag{3.14}$$

$L \cdot \frac{d\hat{i}_L(t)}{dt} = V_{pv} + \hat{v}_{pv} - r_L \cdot (I_L + \hat{i}_L(t)) - (D' - \hat{d}(t))(V_{fw} + V_{Bat})$

$$L \cdot \frac{d\hat{i}_L(t)}{dt} = V_{pv} - r_L \cdot I_L - D' \cdot (V_{fw} + V_{Bat}) + \hat{v}_{pv}(t) - r_L \cdot \hat{i}_L(t) + \hat{d}(t) \cdot (V_{fw} + V_{Bat}) \tag{3.15}$$

Replacing 3.6 in equation 3.15, we find:

$$\frac{d\hat{i}_L(t)}{dt} = -\frac{r_L}{L} \cdot \hat{i}_L(t) + \frac{1}{L} \cdot \hat{v}_{pv}(t) + \frac{(V_{fw} + V_{Bat})}{L} \cdot \hat{d}(t) \tag{3.16}$$

On the other hand, we have also:

$$i_{C_{in}}(t) = i_{pv}(t) - i_L(t) \tag{3.17}$$

Replacing by the following small signal approximation variables:

$$\begin{cases} i_{C_{in}}(t) = I_{C_{in}} + \hat{i}_{C_{in}}(t) \\ i_{pv}(t) = I_{pv} + \hat{i}_{pv}(t) \\ i_L(t) = I_L + \hat{i}_L(t) \end{cases} \tag{3.18}$$

we find:

$$\hat{i}_{C_{in}}(t) = \hat{i}_{pv}(t) - \hat{i}_L(t) \tag{3.19}$$

as $I_{C_{in}} = I_{pv} + I_L$ according to equation (3.4).
For the input capacitor C_{in}:
$C_{in} \cdot \frac{dv_{c_{in}}(t)}{dt} = i_{pv}(t) - i_L(t)$
by noting that $v_{c_{in}}(t) = v_{pv}(t)$, we find:

$$\frac{dv_{pv}(t)}{dt} = \frac{1}{C_{in}} \cdot i_{pv}(t) - \frac{1}{C_{in}} \cdot i_L(t) \tag{3.20}$$

The small signal approximation gives the following:

$$\begin{cases} v_{pv}(t) = V_{pv} + \hat{v}_{pv}(t) \\ i_{pv}(t) = I_{pv} + \hat{i}_{pv}(t) \\ i_L(t) = I_L + \hat{i}_L(t) \end{cases} \tag{3.21}$$

as $I_{pv} - I_L = 0$ from eq. (3.9), equation (3.20) becomes:

$$\frac{d\hat{v}_{pv}(t)}{dt} = \frac{1}{C_{in}} \cdot \hat{i}_{pv}(t) - \frac{1}{C_{in}} \cdot \hat{i}_L(t) \tag{3.22}$$

From the definition of dynamic resistance in Chapter 2, equation (2.6): $r_{pv} = -\frac{\partial v_{pv}(t)}{\partial i_{pv}(t)}$ by taking $\partial v_{pv} = \hat{v}_{pv}$ and $\partial i_{pv} = \hat{i}_{pv}$, hence $r_{pv} = -\frac{\hat{v}_{pv}}{\hat{i}_{pv}}$, results in:

$$\frac{d\hat{v}_{pv}(t)}{dt} = \frac{-1}{r_{pv} \cdot C_{in}} \cdot \hat{v}_{pv}(t) - \frac{1}{C_{in}} \cdot \hat{i}_L(t) \tag{3.23}$$

From equations (3.16) and (3.23), and by choosing the following state variables:

$$\begin{cases} x_1(t) = i_L(t) \\ x_2(t) = v_{pv}(t) \end{cases} \tag{3.24}$$

The continuous-time state space model of the boost DC-DC converter can be obtained as follows:

$$\begin{bmatrix} \dot{x}_1(t) \\ \dot{x}_2(t) \end{bmatrix} = \begin{bmatrix} \frac{d\hat{i}_L(t)}{dt} \\ \frac{d\hat{v}_{pv}(t)}{dt} \end{bmatrix} = \begin{bmatrix} -\frac{r_L}{L} & \frac{1}{L} \\ -\frac{1}{C_{in}} & \frac{-1}{r_{pv}\cdot C_{in}} \end{bmatrix} \cdot \begin{bmatrix} \hat{i}_L(t) \\ \hat{v}_{pv}(t) \end{bmatrix} + \begin{bmatrix} \frac{(V_{fw}+V_{Bat})}{L} \\ 0 \end{bmatrix} \cdot \hat{d}(t) \tag{3.25}$$

By taking the derivative of eq. (3.23), we get:

$$\frac{d^2\hat{v}_{pv}(t)}{dt^2} = \frac{-1}{r_{pv}\cdot C_{in}} \cdot \frac{d\hat{v}_{pv}(t)}{dt} - \frac{1}{C_{in}} \cdot \frac{d\hat{i}_L(t)}{dt} \tag{3.26}$$

When replacing $\frac{d\hat{i}_L(t)}{dt}$ of equation (3.26) in (3.25):

$$\frac{d^2\hat{v}_{pv}(t)}{dt^2} = \frac{-1}{r_{pv}\cdot C_{in}} \cdot \frac{d\hat{v}_{pv}(t)}{dt} + \frac{r_L}{L\cdot C_{in}} \cdot \hat{i}_L(t) - \frac{1}{L\cdot C_{in}} \cdot \hat{v}_{pv}(t) - \frac{(V_{fw}+V_{Bat})}{L\cdot C_{in}} \cdot \hat{d}(t) \tag{3.27}$$

From eq. (3.22):

$$\hat{i}_L(t) = \hat{i}_{pv}(t) - C_{in} \cdot \frac{d\hat{v}_{pv}(t)}{dt} \tag{3.28}$$

inserting eq. (3.28) in (3.27):

$$\begin{aligned} \frac{d^2\hat{v}_{pv}(t)}{dt^2} = & \frac{-1}{r_{pv}\cdot C_{in}} \cdot \frac{d\hat{v}_{pv}(t)}{dt} + \frac{r_L}{L\cdot C_{in}} \cdot \left(i_{pv}(t) - C_{in} \cdot \frac{dv_{pv}(t)}{dt}\right) \\ & -\frac{1}{L\cdot C_{in}} \cdot \hat{v}_{pv}(t) - \frac{(V_{fw}+V_{Bat})}{L\cdot C_{in}} \cdot \hat{d}(t) \end{aligned} \tag{3.29}$$

$$\begin{aligned} \frac{d^2\hat{v}_{pv}(t)}{dt^2} = & \left(-\frac{r_L}{L} - \frac{1}{r_{pv}\cdot C_{in}}\right) \cdot \frac{d\hat{v}_{pv}(t)}{dt} + \frac{r_L}{L\cdot C_{in}} \cdot i_{pv}(t) \\ & -\frac{1}{L\cdot C_{in}} \cdot \hat{v}_{pv}(t) - \frac{(V_{fw}+V_{Bat})}{L\cdot C_{in}} \cdot \hat{d}(t) \end{aligned} \tag{3.30}$$

we replace $\hat{v}_{pv} = -r_{pv} \cdot \hat{i}_{pv}$ in equation (3.30), we get:

$$\begin{aligned} \frac{d^2\hat{i}_{pv}(t)}{dt^2} = & -\left(\frac{r_L}{L} + \frac{1}{r_{pv}\cdot C_{in}}\right) \cdot \frac{d\hat{i}_{pv}(t)}{dt} - \left(\frac{r_L}{r_{pv}\cdot L\cdot C_{in}} + \frac{1}{L\cdot C_{in}}\right) \cdot \hat{i}_{pv}(t) \\ & +\frac{(V_{fw}+V_{Bat})}{r_{pv}\cdot L\cdot C_{in}} \cdot \hat{d}(t) \end{aligned} \tag{3.31}$$

by taking the following state variables:

$$\begin{cases} z_1(t) = i_{pv}(t) \\ z_2(t) = \frac{di_{pv}(t)}{dt} \end{cases} \tag{3.32}$$

we get:

$$\begin{cases} \dot{z}_1(t) = z_2(t) \\ \dot{z}_2(t) = -\left(\frac{r_L}{r_{pv}\cdot L\cdot C_{in}} + \frac{1}{L\cdot C_{in}}\right)\cdot z_1(t) - \left(\frac{r_L}{L} + \frac{1}{r_{pv}\cdot C_{in}}\right)\cdot z_2(t) + \frac{(V_{fw}+V_{Bat})}{r_{pv}\cdot L\cdot C_{in}}\cdot \hat{d}(t) \end{cases} \tag{3.33}$$

$$\begin{bmatrix} \dot{z}_1(t) \\ \dot{z}_2(t) \end{bmatrix} = \begin{bmatrix} 0 & 1 \\ -\left(\frac{r_L}{r_{pv}\cdot L\cdot C_{in}} + \frac{1}{L\cdot C_{in}}\right) & -\left(\frac{r_L}{L} + \frac{1}{r_{pv}\cdot C_{in}}\right) \end{bmatrix} \cdot \begin{bmatrix} z_1(t) \\ z_2(t) \end{bmatrix} + \begin{bmatrix} 0 \\ \frac{(V_{fw}+V_{Bat})}{r_{pv}\cdot L\cdot C_{in}} \end{bmatrix} \cdot \hat{d}(t) \tag{3.34}$$

For the PV voltage:

$$\begin{bmatrix} \dot{z}_1(t) \\ \dot{z}_2(t) \end{bmatrix} = \begin{bmatrix} 0 & 1 \\ -\left(\frac{r_L}{r_{pv}\cdot L\cdot C_{in}} + \frac{1}{L\cdot C_{in}}\right) & -\left(\frac{r_L}{L} + \frac{1}{r_{pv}\cdot C_{in}}\right) \end{bmatrix} \cdot \begin{bmatrix} z_1(t) \\ z_2(t) \end{bmatrix} - \begin{bmatrix} 0 \\ \frac{(V_{fw}+V_{Bat})}{L\cdot C_{in}} \end{bmatrix} \cdot \hat{d}(t) \tag{3.35}$$

Which represents a second state space model ($\dot{z}(t) = Az(t) + Bu(t)$) of the boost dc-dc converter using the PV array current as state variable. The controllability matrix $\mathcal{G} = [B \quad AB \quad A^2B]$ have a full rank, hence the states are controllable.

The first state space model (3.25) is used when considering PV current tracking by supposing the input capacitor current is negligible or in the case of using the PV voltage as control variable. When the capacitor current is considered, the model (3.35) is used instead as it explicitly uses the PV current.

3.2.2 Transfer functions of the boost DC-DC converter

The Laplace transform is applied to equations (3.16) and (3.23) as follows:

$$s\cdot I_L(s) = -\frac{r_L}{L}\cdot I_L(s) + \frac{1}{L}\cdot v_{pv}(s) + \frac{(V_{fw}+V_{Bat})}{L}\cdot D(s) \tag{3.36}$$

$$s\cdot V_{pv}(s) = \frac{-1}{r_{pv}\cdot C_{in}}\cdot V_{pv}(s) - \frac{1}{C_{in}}\cdot I_L(s) \tag{3.37}$$

by rearranging eqs. (3.33) and (3.34):

$$I_L(s) = \frac{1}{L \cdot s + r_L} \cdot V_{pv}(s) + \frac{(V_{fw} + V_{Bat})}{L \cdot s + r_L} \cdot D(s) \tag{3.38}$$

$$V_{pv}(s) = \frac{-r_{pv}}{r_{pv} \cdot C_{in} \cdot s + 1} \cdot I_L(s) \tag{3.39}$$

when inserting eq. (3.39) in (3.38), we find the transfer function of the inductor current with respect to duty ratio:

$$\frac{I_L(s)}{D(s)} = \frac{r_{pv} \cdot C_{in} \cdot (V_{fw} + V_{Bat}) \cdot s + (V_{fw} + V_{Bat})}{r_{pv} \cdot L \cdot C_{in} \cdot s^2 + (L + r_{pv} \cdot r_L \cdot C_{in}) \cdot s + r_{pv} + r_L} \tag{3.40}$$

by replacing equation (3.38) in (3.39), we deduce the transfer function of the PV array's voltage with respect to the duty ratio:

$$\frac{V_{pv}(s)}{D(s)} = \frac{-r_{pv} \cdot (V_{fw} + V_{Bat})}{r_{pv} \cdot L \cdot C_{in} \cdot s^2 + (L + r_{pv} \cdot r_L \cdot C_{in}) \cdot s + r_{pv} + r_L} \tag{3.41}$$

Hence, the transfer function of the PV array's current with respect to the duty ratio is given as follows:

$$\frac{I_{pv}(s)}{D(s)} = \frac{(V_{fw} + V_{Bat})}{r_{pv} \cdot L \cdot C_{in} \cdot s^2 + (L + r_{pv} \cdot r_L \cdot C_{in}) \cdot s + r_{pv} + r_L} \tag{3.42}$$

Figure 3.4 shows the open loop response of the duty ratio to voltage in Figure 3.4(a), which presents a variable response in terms of response time and static error. The duty response to current shows the same characteristics in Figure 3.4(b). The open loop response shows the limitations of direct control based (using duty ratio as control variable) techniques, especially in maximum power point tracking techniques.

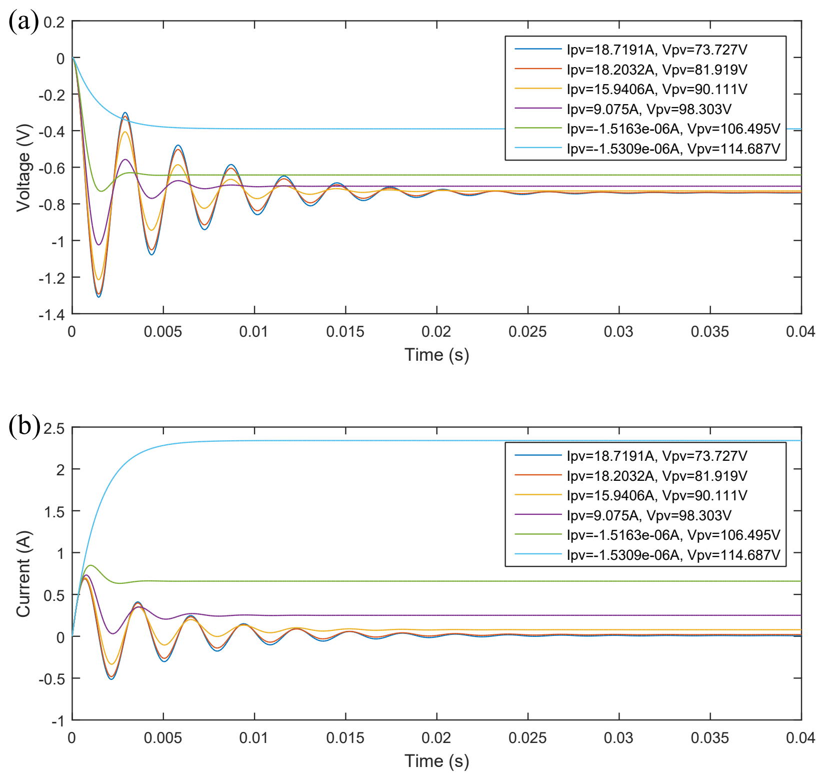

FIGURE 3.4: Response of the control to PV array voltage and current open-loop transfer functions at different operating points: (a) control-to-PV voltage response, (b) control-to-PV current response.

3.3 Controller design for the boost DC-DC converter

The implementation of the controller in a digital signal controller (DSC) requires the design of the controller in discrete form. The continuous time state space model (3.25) of the boost DC-DC converter may be written in discrete form as follows:

$$\begin{cases} x(k+1) = Ax(k) + Bu(k) \\ y(k) = Cx(k) \end{cases} \tag{3.43}$$

The control variable $u = d$ is the converter duty cycle. The output matrix C depends on the variable to be tracked. $C = [1\ 0]$ is chosen in the case of current tracking, while $C = [0\ 1]$ in the case of voltage tracking.

The state space model (3.43) of the boost DC-DC converter is used to design an optimal tracking controller for current and voltage variables. The tracking objective is defined as follows:

$$e_r(k) = y_r - y(k) = 0 \tag{3.44}$$

To achieve such objective, a Proportional Integral (PI)-like controller is designed by adding an integral state to the system (3.43) as follows:

$$\begin{cases} e_r & = \frac{x_I(k+1)-x_I(k)}{Ts} \\ x_I(k+1) & = x_I(k) + T_s(y_r(k) - y(k)) \\ & = x_I(k) + T_s(y_r(k) - Cx(k)) \end{cases} \tag{3.45}$$

The integration constant T_s in equation (3.45) is designed such that the control algorithm has time for execution and on the other hand the system must remain stable. The system (3.43) is augmented by the integral state as follows:

$$\begin{cases} \begin{bmatrix} x(k+1) \\ x_I(k+1) \end{bmatrix} & = \begin{bmatrix} A & 0_2^1 \\ -T_sC & 1 \end{bmatrix} \begin{bmatrix} x(k) \\ x_I(k) \end{bmatrix} + \begin{bmatrix} B \\ 0 \end{bmatrix} u(k) + \begin{bmatrix} 0_2^1 \\ Ts \end{bmatrix} y_r(k) \\ y(k) & = \begin{bmatrix} C & 0 \end{bmatrix} \begin{bmatrix} x(k) \\ z(k) \end{bmatrix} \end{cases} \tag{3.46}$$

Which are noted as follows:

$$\begin{cases} \tilde{x}(k+1) & = \tilde{A}\tilde{x}(k) + \tilde{B}u(k) + \tilde{B}_r y_r(k) \\ y(k) & = \tilde{C}\tilde{x}(k) \end{cases} \tag{3.47}$$

Where:

$$\tilde{A} = \begin{bmatrix} A & 0_2^1 \\ -T_sC & 1 \end{bmatrix} \quad \tilde{B} = \begin{bmatrix} B \\ 0 \end{bmatrix} \quad \tilde{B}_r = \begin{bmatrix} 0_2^1 \\ Ts \end{bmatrix} \quad \tilde{C} = \begin{bmatrix} C & 0 \end{bmatrix}$$

The state feedback control law of the system 3.47 is computed as follows:

$$u(k) = -K\tilde{x}(k) = -\begin{bmatrix} K_p & K_I \end{bmatrix} \begin{bmatrix} x(k) \\ x_I(k) \end{bmatrix} \tag{3.48}$$

The feedback gain K is designed using a Linear Quadratic Regulator (LQR) approach which is used to design the optimal tracking regulator as to minimize the following objective function:

$$J = \int_0^{+\infty} \left(\tilde{x}^T Q \tilde{x} + u^T R u \right) dt \tag{3.49}$$

such that $Q = Q^T \geq 0$, $R = R^T > 0$. Figure 3.5 shows the step response of the LQR designed regulator for voltage and current tracking. Voltage regulation response shows sensitivity to operating point and slower response when compared with current regulation. For these reasons, current regulation will be used in the consequent work to track the maximum power point.

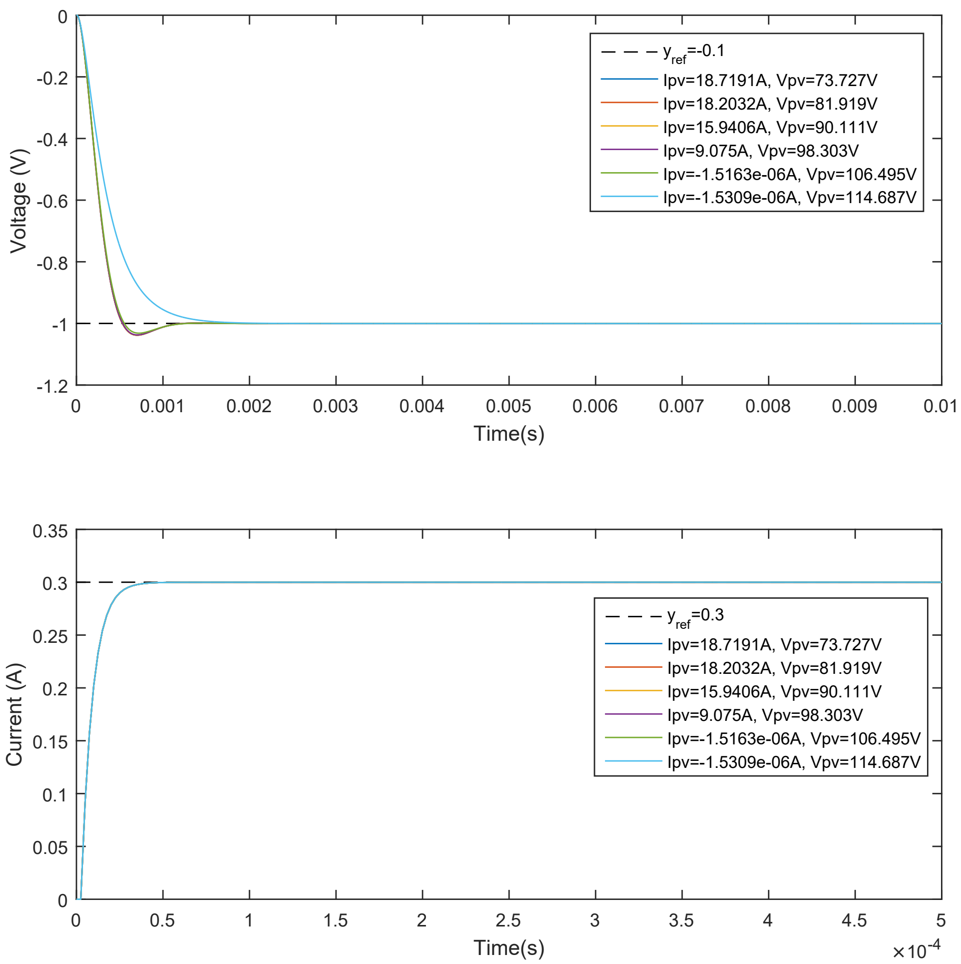

FIGURE 3.5: Response of PV array LQR-based voltage and current based closed-loop transfer functions at different operating points: (a) reference voltage tracking, (b) reference current tracking.

3.4 Maximum power point tracking

It was shown in Chapter 2 that temperature and irradiation variations result in varying the MPP in a wide range. The direct connection of the PV array to a power conversion system would be an intuitive but inefficient solution. When connected with a battery, the PV array will provide maximum power only if the battery voltage is close to the actual MPP voltage operating point. In the case of a resistive load, the maximum power is verified only if the load characteristic curve intersects with the I-V curve of the PV array at the MPP operating point.

To verify such specifications, an intermediate power conversion stage has to be inserted in order to adjust the PV array operating point to match the MPP. The DC-DC converter presented in the previous section is used for this purpose. By varying continuously the duty cycle of the converter, the conversion stage will be able to track the MPP dynamically. The algorithms designed to accomplish such task are called **M**aximum **P**ower **P**oint **T**racking (or **MPPT**). Their common objective is to track continuously the MPP under varying PV array environmental conditions. The intuitive approach to calcu-

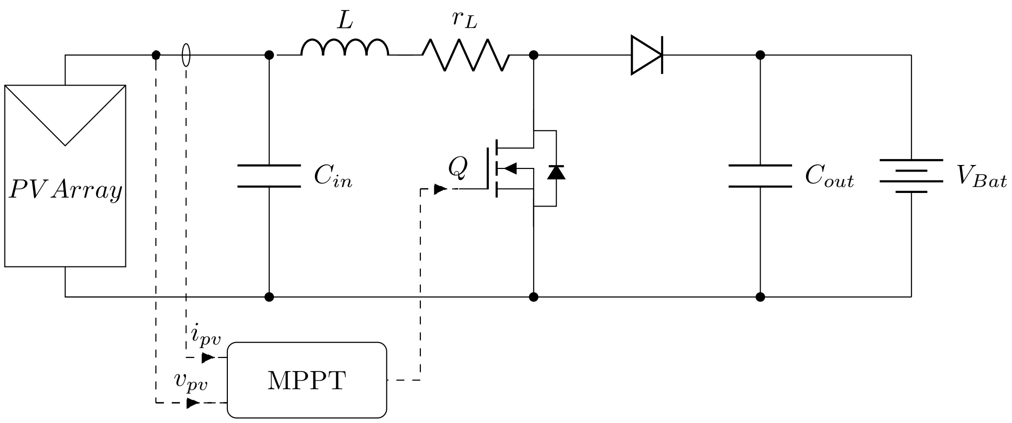

FIGURE 3.6: Boost DC-DC converter with MPPT.

late the MPP operating point is to use available known data as open-circuit voltage and short-circuit current to estimate the actual MPP, such approach is called Fractional Open-circuit voltage in the case of using PV voltage variable and fractional short-circuit current in the case of PV current.

3.4.1 Fractional open-circuit voltage and short-circuit current

In the fractional open-circuit voltage (also called constant voltage), the MPP operating point is estimated using an approximation of the considered PV array, the operating voltage at MPP is given as follows [18]:

$$V_{MPP} \approx k \cdot V_{oc} \tag{3.50}$$

The estimation factor k is reported in the literature to be in the range $70 - 82\%$. V_{oc} is mainly affected by temperature as shown in Chapter 2. The fractional short-circuit current (constant current) method uses the same approach of the open-circuit voltage with a different range $78 - 92\%$.

$$I_{MPP} \approx k \cdot I_{sc} \tag{3.51}$$

3.4.2 Hill-climbing and the P&O MPPT

The simplest structure to continuously track the MPP consists of perturbing the actual operating point of the PV array and observing the resultant change in power. According to the sign of the change in power, an appropriate increase or decrease in the actual operating point is executed. The perturbed variable may be the duty cycle of the dc-dc converter (in this case the MPPT may be called Hill Climbing as in [18]), or it may be the PV output voltage [38] or current[39]. The flowchart of this technique is given in figure 3.7. The variable X may be chosen to be the duty cycle, PV voltage or current. In the case of duty cycle, the sign of perturbation step ϕ have to be inverted in the case of the boost dc-dc converter as the voltage is inversely proportional to the duty cycle.

The P&O MPPT is characterized by steady state oscillations that may be minimized by using a variable perturbation step [40]. The algorithm may also fail in fast changing irradiation [41] as in the case of passing clouds which may be solved by adding appropriate handling logic as will be presented in the incremental conductance MPPT.

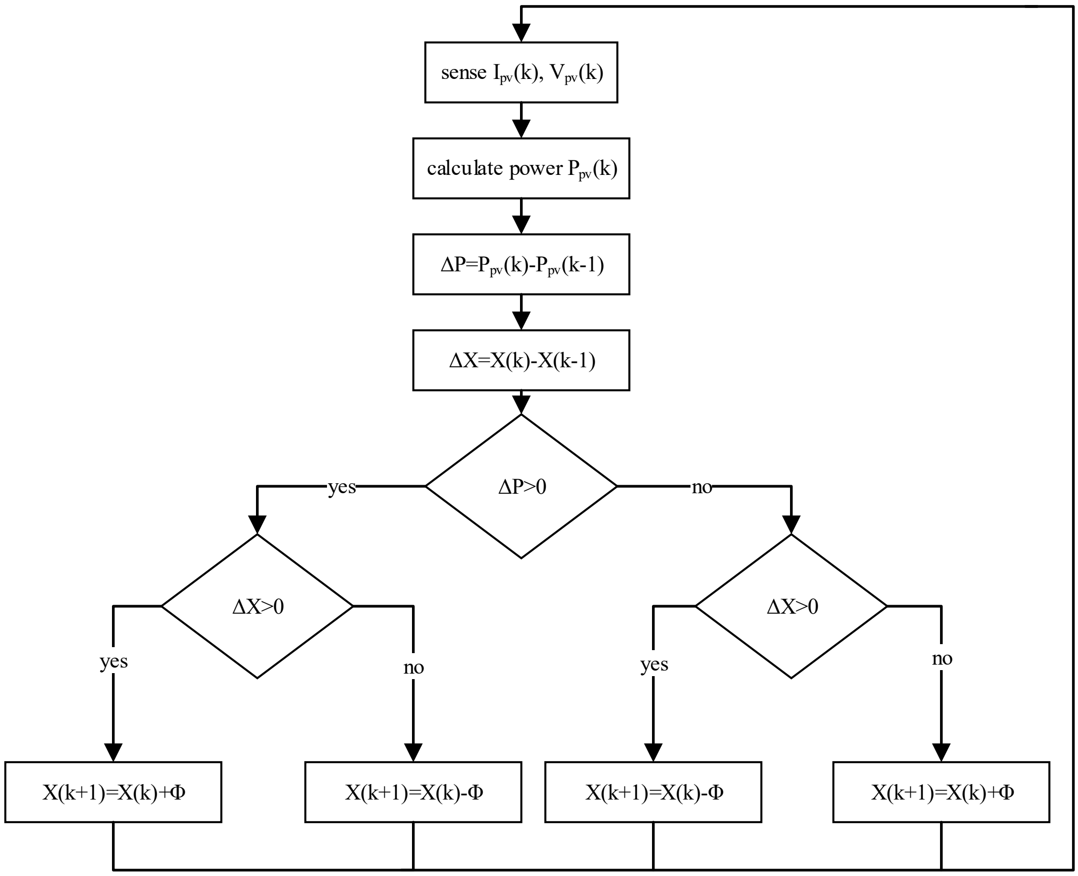

FIGURE 3.7: Flowchart of the Hill climbing and P&O algortihms.

3.4.3 Incremental Conductance (IncCond) MPPT

The incremental conductance algorithm uses the sign of the power-voltage curve as follows:

$$\begin{cases} \frac{dP}{dV} = 0, \; at\ MPP \\ \frac{dP}{dV} > 0, \; at\ the\ left\ of\ the\ MPP \\ \frac{dP}{dV} < 0, \; at\ the\ right\ of\ the\ MPP \end{cases} \tag{3.52}$$

we know that:

$$\frac{dP}{dV} = \frac{d(I \cdot V)}{dV} = I\frac{dV}{dV} + V\frac{dI}{dV} = I + V\frac{dI}{dV} \tag{3.53}$$

the conditions in 3.52 may be rewritten as follows:

$$\begin{cases} \frac{\Delta I}{\Delta V} = -\frac{I}{V}, \ at\ MPP \\ \frac{\Delta I}{\Delta V} > -\frac{I}{V}, \ left\ of\ the\ MPP \\ \frac{\Delta I}{\Delta V} < -\frac{I}{V}, \ right\ of\ the\ MPP \end{cases} \tag{3.54}$$

which gives the conditions for achieving MPPT using the conductance $\frac{I}{V}$ and the incremental conductance $\frac{\Delta I}{\Delta V}$. The IncCond MPPT may then be constructed as illustrated in the flowchart in figure 3.8. The detection of fast change in irradiation is highlighted, the operation at MPP is characterized by equal incremental conductance to the actual conductance, and no change in operating point ($dV = 0$), the fast change in irradiation induces a change in the PV current, the appropriate actions are then taken. The presence of

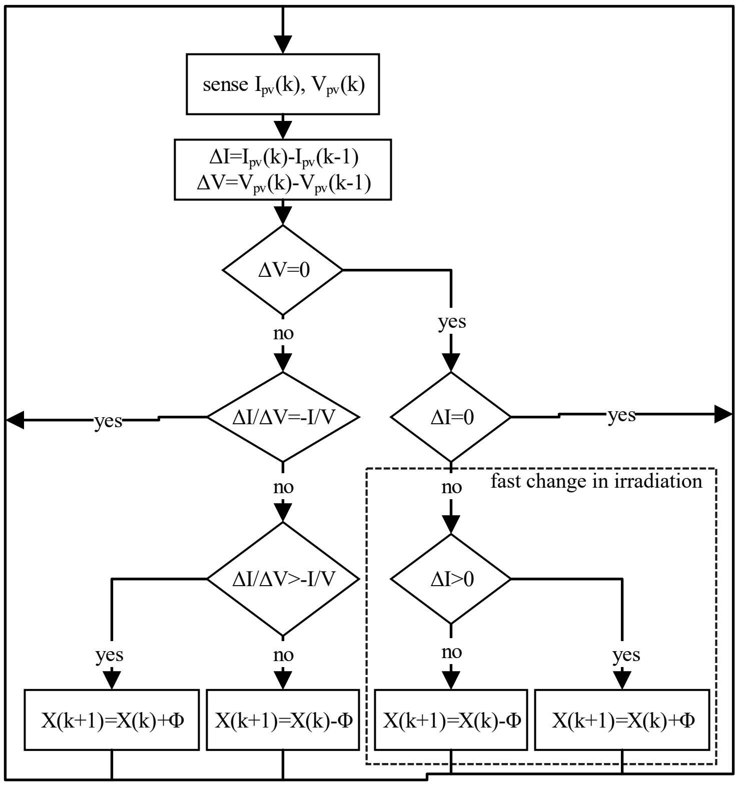

FIGURE 3.8: Flowchart of the IncCond algortihm.

multi-peak power-voltage curve makes the MPPT algorithm fail to track the global MPP, as both P&O and IncCond algorithms are trapped at the first occurrence of extremum that may or may not be the global. To solve such issue, soft-computing methods have been proposed to track the global maximum by using a meta-heuristic search.

3.4.4 Soft computing MPPT

Working with imprecise data using a precise technique may lead to a loss of performance and even instability, fuzzy logic and neural network based MPPT algorithms have been designed to deal with the nonlinearity present in PV array characteristic curve and also may have good performance in the presence of incomplete knowledge of the controlled system. However these techniques require history of the operation and experience from the PV installation that may not be available. In addition, the algorithms fail to track the MPP in the presence of multi-peak characteristic curve.
The problem of nonlinearity in P-V curve of PV arrays in addition to the effect of faults and operating conditions that results in the creation of multiple extremum points have initiated the use of meta-heuristic search algorithms to track the global maximum power point (GMPP). The authors in [27] have first proposed the implementation of a Particle Swarm Optimization based MPPT to track the GMPP of a PV array subject to partial shading. The PSO algorithm was first proposed in [42], and multiple modified versions have been proposed to enhance convergence compared to other optimization algorithms as in [43] with genetic algorithms. The PSO technique has been reported to perform better in terms of success rate and quality of the final solution [44].

Particle Swarm Optimization algorithm

The first version of the PSO algorithm introduced in [42] is based on the principle that each individual(particle) that flies within a swarm of particles in a given search space is characterized by a dynamically variable velocity modified according to its experience and that of its companions. The variables that characterize the particle are summarized as follows:

- The position of a given particle (i) at a given iteration (k) is noted x_i^k.

- The best known previous position that gives the personal best fitness of this particle is noted $pbest_i$.
- The best position among all the particles of the swarm is noted $gbest$.
- The dynamic rate of change of the position of a particle (i) that represents its velocity at a given iteration (k) is noted v_i^k.

The velocity and position are updated as follows:

$$\begin{cases} v_i^{k+1} = v_i^k + c_1 \cdot r_1 \cdot \left(pbest_i - x_i^k\right) + c_2 \cdot r_2 \cdot \left(gbest - x_i^k\right) \\ x_i^{k+1} = x_i^k + v_i^{k+1} \end{cases} \tag{3.55}$$

where c_1 and c_2 are positive constants that adds weights to the tendency to personal best or group best position. r_1, r_2 are random numbers in $[0\ 1]$. An inertia weight has been added in [45] to make a balance between global and local search, the global search is a priority when w the weighting factor is close to 1, a local search is facilitated when w is small. The updated PSO equation is given in equation (3.56).

$$\begin{cases} v_i^{k+1} = w \cdot v_i^k + c_1 \cdot r_1 \cdot \left(pbest_i - x_i^k\right) + c_2 \cdot r_2 \cdot \left(gbest - x_i^k\right) \\ x_i^{k+1} = x_i^k + v_i^{k+1} \end{cases} \tag{3.56}$$

A graphical representation of the process of update of the dynamic velocity is given in figure 3.9. The illustration gives an interpretation of the multi-dimensional optimization problem where the variables are not on the same axis.

3.5 Summary

The nonlinear characteristic curve of the PV array requires the addition of an intermediate power conversion stage in order to track the optimal operating point in the presence of variable operating conditions. The presence of multi-peaks in the power-voltage curve makes the tracking more challenging

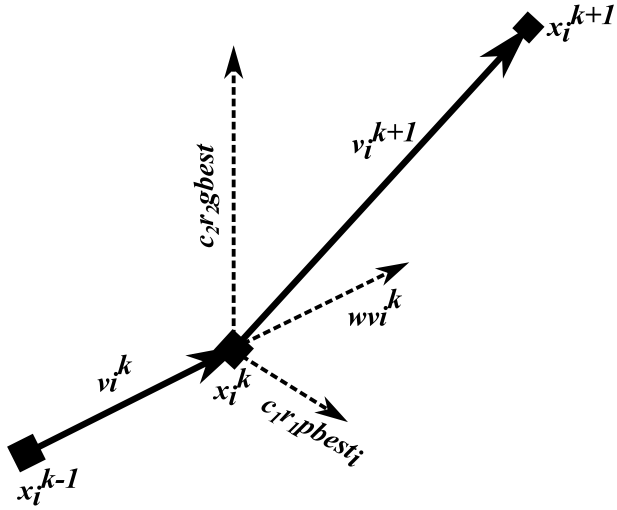

FIGURE 3.9: Particle swarm position update.

as conventional search techniques may be trapped in local extremum characterized by a low power output. Using evolutionary search algorithms allows the tracking of global extremum independently of the shape of the power-voltage characteristic curve.

Chapter 4

Fault-tolerant control of photovoltaic energy processes

4.1 Introduction

Fault tolerant control (FTC) is mainly motivated by the improvement of safety and efficiency of processes, it can be classified into two main categories: passive and active FTC [46], [47]. In the passive approach, faults that may affect a normal operation are known and are taken into consideration in the design stage of the fault tolerant controller. In active fault-tolerant control architectures, faults are unknown and the tolerance is achieved by the reconfiguration of the controller, it consists of two main steps: Fault Detection and Isolation (FDI) and controller reconfiguration. In the FDI stage, the system is supervised and faults are detected with minimal uncertainties and then isolated using a diagnosis procedure. When a fault is detected, the controller is reconfigured to achieve stability and acceptable closed-loop performance [48].

4.2 Sensor-fault-tolerant control of the PV array

The sensor fault tolerance is considered as a *passive control technique* as the fault nature is known and the control law is designed to be insensitive to bias in sensors. In order to achieve such objective, a fault estimation is necessary to cancel the additive action resulting from the sensor fault. The sensor fault will be considered as an unknown input vector added to the system (3.43) as follows:

$$\begin{cases} x(k+1) = Ax(k) + Bu(k) \\ y(k) = Cx(k) + F_s f_s(k) \end{cases} \tag{4.1}$$

Where F_s is assumed to be known, and f_s represents sensor fault magnitude to be estimated. The Singular Value Decomposition (SVD) will be used to estimate the magnitude of the sensor fault.

If the variable to be tracked is chosen to be the PV current then:

$$y = \begin{bmatrix} C_1 & C_2 \end{bmatrix} x(k) + \begin{bmatrix} F_{s1} & F_{s2} \end{bmatrix} f_s(k) = C_1 x(k) + F_{s1} f_s(k) \tag{4.2}$$

as $C_2 = F_{s2} = 0$ when the PV current variable is chosen.

The tracking integral is then given as follows:

$$\begin{cases} x_I(k+1) & = x_I(k) + T_s(y_r(k) - y(k)) \\ & = x_I(k) + T_s(y_r(k) - C_1 x(k) - F_{s1} f_s(k)) \end{cases} \tag{4.3}$$

4.2.1 Sensor fault estimation

The magnitude of the sensor fault can be estimated when considered as an additional component of the augmented state vector $\bar{X}_s(k)$. The augmented state space system is given as follows [49]:

$$\bar{E}_s \bar{X}_s(k+1) = \bar{A}_s \bar{X}_s(k) + \bar{B}_s \bar{U}(k) + \bar{G}_s y_r(k) \tag{4.4}$$

$$\bar{E}_s = \begin{bmatrix} I_n & 0 & 0 \\ 0 & I_p & 0 \\ C & 0 & F_s \end{bmatrix} \quad \bar{A}_s = \begin{bmatrix} A & 0 & 0 \\ -T_s C_1 & I_p & -T_s F_{s1} \\ 0 & 0 & 0 \end{bmatrix} \quad \bar{B}_s = \begin{bmatrix} B & 0 \\ 0 & 0 \\ 0 & I_q \end{bmatrix}$$

$$\bar{G}_s = \begin{bmatrix} 0 \\ T_s I_p \\ 0 \end{bmatrix} \quad \bar{X}_s(k) = \begin{bmatrix} x(k) \\ x_I(k) \\ f_s(k) \end{bmatrix} \quad \bar{U}(k) = \begin{bmatrix} u(k) \\ y(k+1) \end{bmatrix}$$

Using the singular value decomposition of the matrix $\bar{E}_s$(if $\bar{E}_s$ is of full rank), the estimated magnitude of the fault can be calculated.

The SVD of $\bar{E}_s$ is given as follows: $\bar{E}_s = T \begin{bmatrix} S \\ 0 \end{bmatrix} M^T$, with $T = \begin{bmatrix} T_1 \\ T_2 \end{bmatrix}$

The matrices T and M are orthonormal: $TT^T = I,\ MM^T = I$, and S is a non-singular diagonal matrix.

The solution of eq. (4.4) using the SVD of $\bar{E}_s$ and its pseudo inverse $\bar{E}_s^+$ gives the following equations:

$$\begin{cases} \bar{X}_s(k+1) &= \tilde{A}_s\bar{X}_s(k) + \tilde{B}_s\bar{U}(k) + \tilde{G}_s y_r(k) \\ 0 &= \tilde{A}_0\bar{X}_s(k) + \tilde{B}_0\bar{U}(k) + \tilde{G}_0 y_r(k) \end{cases} \tag{4.5}$$

where

$$\begin{aligned} \tilde{A}_s &= MS^{-1}T_1^T\bar{A}_s = \bar{E}_s^+\bar{A}_s, \quad \tilde{A}_0 = T_2^T\bar{A}_s \\ \tilde{B}_s &= MS^{-1}T_1^T\bar{B}_s = \bar{E}_s^+\bar{B}_s, \quad \tilde{B}_0 = T_2^T\bar{B}_s \\ \tilde{G}_s &= MS^{-1}T_1^T\bar{G}_s = \bar{E}_s^+\bar{G}_s, \quad \tilde{G}_0 = T_2^T\bar{G}_s \end{aligned} \tag{4.6}$$

4.2.2 Sensor fault compensation

The modified sensor fault tolerant control law is designed by taking into account the fault in the closed loop system as follows:

$$\begin{cases} u(k) &= -K_p x_f(k) - K_p F_s f_s(k) - K_I x_{If}(k) - K_I\tilde{f}(k) + u_{FTC}(k) \\ \tilde{f}(k) &= \tilde{f}(k-1) - T_e F_{s1} f_s(k-1) \\ x_I(k) &= x_{If}(k) + \tilde{f}(k) \end{cases} \tag{4.7}$$

where x_f and x_{If} are fault-free variables, and $C = I$. The compensation for the fault can be given as:

$$u_{FTC} = K_p F_s \hat{f}_s(k) + K_I\tilde{f}(k) \tag{4.8}$$

where $\hat{f}_s$ is the estimation of the magnitude of the sensor fault.

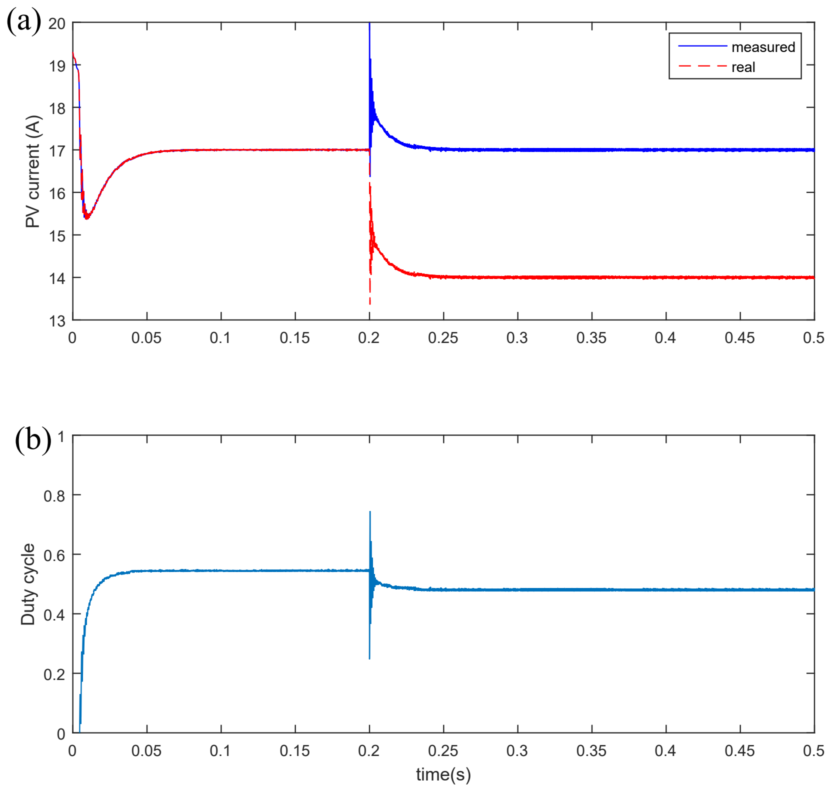

FIGURE 4.1: PV array subject to a sensor fault without FTC:(a) PV array current, (b) Duty cycle.

4.2.3 PV array sensor-fault-tolerant control

In a first step, the PV array is subject to sensor fault of magnitude ($I_f = 3A$) at the time instant ($t = 0.2s$), the response of the non compensated PV array current to the sensor fault is given in figure 4.1(a). The measured current is regulated to the reference current ($I_{ref} = 17A$) whereas the real PV current is shifted by the sensor fault offset. The action of the controller to compensate the measured bias is shown in figure 4.1(b).

When the fault tolerant control procedure is implemented, the fault magnitude is estimated and the controller is prevented to act for the sensor offset, the duty cycle in figure 4.2(b) shows no action in response to the introduced fault at ($t = 0.2s$), whereas the measured current in figure 4.2(a) shows clearly the offset introduced by the sensor fault.

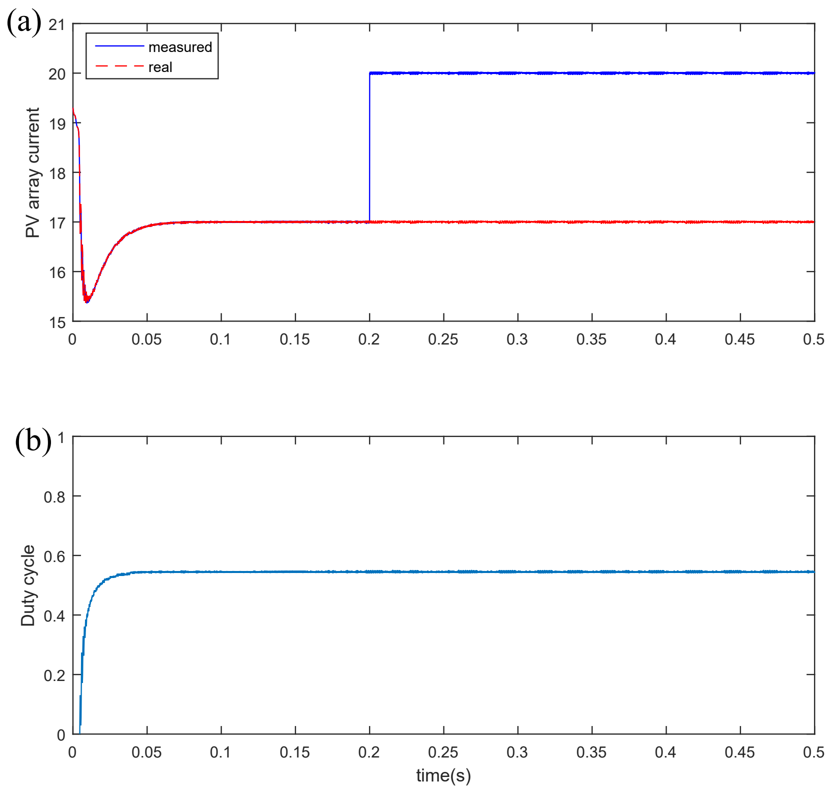

FIGURE 4.2: PV array subject to a sensor fault with FTC:(a) PV array current, (b) Duty cycle.

4.3 Active fault-tolerant strategy for PV systems

In addition to sensing faults, PV arrays are subject to component faults that may have unknown nature so that they may be considered in the controller design stage. An active fault-tolerant strategy is then proposed to deal with such faults. The fault isolation procedure is skipped due to the similarities observed in the patterns of the different types of faults on the P-V curves. The configuration of the fault-tolerant control architecture developed to manage the output power of the PV array is illustrated in Figure 4.3, where the FDI algorithm analyzes the output power of the PV system for an abrupt change caused by a fault or any external disturbance. The controller is then reconfigured in order to drive the system toward an optimal operating point preventing degraded system performance represented by an excessive loss of power.

Existing MPPT algorithms [18], [50] deal only with changes in climatic con-

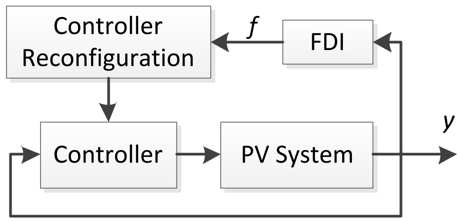

FIGURE 4.3: Fault-tolerant control strategy for PV systems.

ditions and the partial shading phenomena. In the proposed method, mismatch and connection-related faults are considered and the adaptation characteristic of the Particle Swarm Optimisation (PSO) algorithm added to the regulation of the PI controller are used to achieve the fault-tolerance objective.

The proposed fault-tolerant control algorithm is based on the combination of the IncCond MPPT method used in fault-free situation and an improved PSO-based controller selected after detecting a fault using the FDI procedure. The architecture of the proposed control law is given in Figure 4.4 The algo-

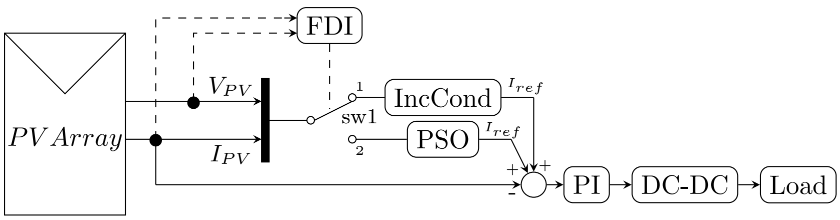

FIGURE 4.4: ICPSO-based fault-tolerant strategy for PV processes.

rithm starts by measuring voltage and current variables across the PV array and calculates the corresponding output power. Resulting output power variable values are given to the FDI procedure to check for the presence of faults in the system as illustrated in Figure 4.4. The controller is then reconfigured based on the value of the fault signal f issued from the FDI procedure by changing the position of the switch (sw_1), the transition is executed when the condition (4.9) is verified [27], where α is determined experimentally. After several tests of different faulted conditions, its best value for our configuration is ($\alpha = 2$). The condition (4.9) allows the detection of abrupt changes in output power that are mainly caused by faults and sudden change in irradiation due to partial shading.

$$\frac{|P_{pv}^{k+1} - P_{pv}^{k}|}{P_{pv}^{k}} > \alpha \tag{4.9}$$

Depending on the outcome of eq. (4.9), a corresponding MPPT algorithm is executed as depicted in Figure 4.4. In fault-free operating conditions, a modified current-based version of the Incremental Conductance (IncCond) algorithm is used to track the MPP by using a hill climbing approach (Figure 4.5). The current-based IncCond is slightly different from the original version proposed in [41]. When a fault is detected ($sw_1 = 2$), the *Improved Current-based PSO (ICPSO)* algorithm is executed; the heuristic search for the global MPP is launched until the following conditions are verified:

$$\begin{cases} Cond_1 : \Delta fitness < \epsilon \\ Cond_2 : N_{iter} \text{ is reached} \end{cases} \tag{4.10}$$

The condition $Cond_1$ tests the convergence of the algorithm by checking if the fitness function has reached a stable value, the addition of such test allows faster convergence of the ICPSO-MPPT algorithm compared to classical PSO based algorithms. Figure 4.6 shows a comparison between the proposed ICPSO and a classical PSO based MPPT algorithm. The ICPSO gives better transient performance and faster tracking. In the case where this test is not verified and the second test $Cond_2$ is reached, the optimization process will be reinitialized until convergence is guaranteed. When $Cond_1$ and $Cond_2$ are verified, the fault-tolerant algorithm gives control to the IncCond. This final step is executed due to the degraded performance of the ICPSO algorithm compared to the IncCond algorithm in steady state operation. In both fault-free and faulted tracking operation, the algorithm results in a reference current I_{ref} that is compared with the actual current value (Figure 4.4), the PI controller makes then an optimal transition to the new reference current value.

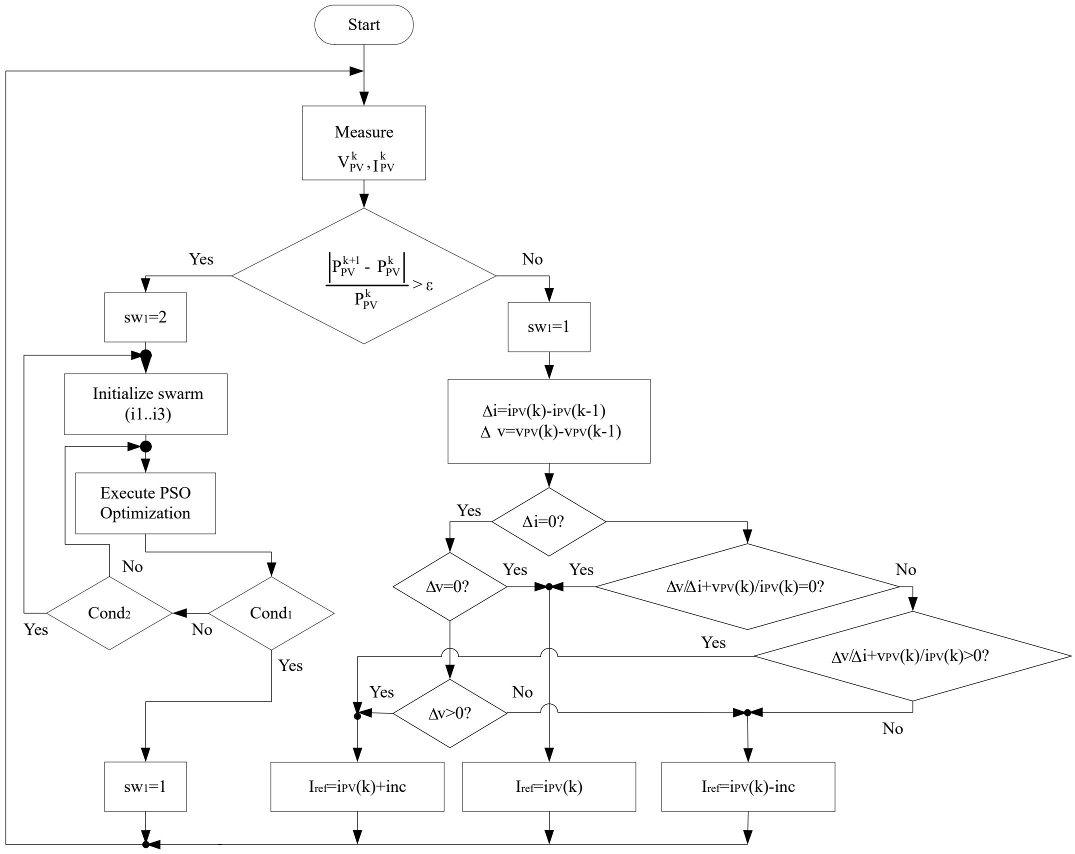

FIGURE 4.5: Proposed FTC strategy flowchart.

4.3.1 Improved Particle Swarm Optimization MPPT

In the PSO algorithm the particles are chosen to be the reference current I_{ref} given to the boost controller. The choice of variable associated to the particle is dependent of the application, in the case of PV panels the particles can be chosen to be the PV panel voltage, current or duty ratio. The current variable was chosen due to the small size of the solutions space (unlike voltage variable) and the possibility of direct implementation for different types of PV panels (unlike duty ratio based method where the direct correspondence between its value and the operation point is not obvious).
The position of particles at each iteration k is given by the vector x^k:

$$x^k = [I^k_1 \; I^k_2 \; ... \; I^k_N] \tag{4.11}$$

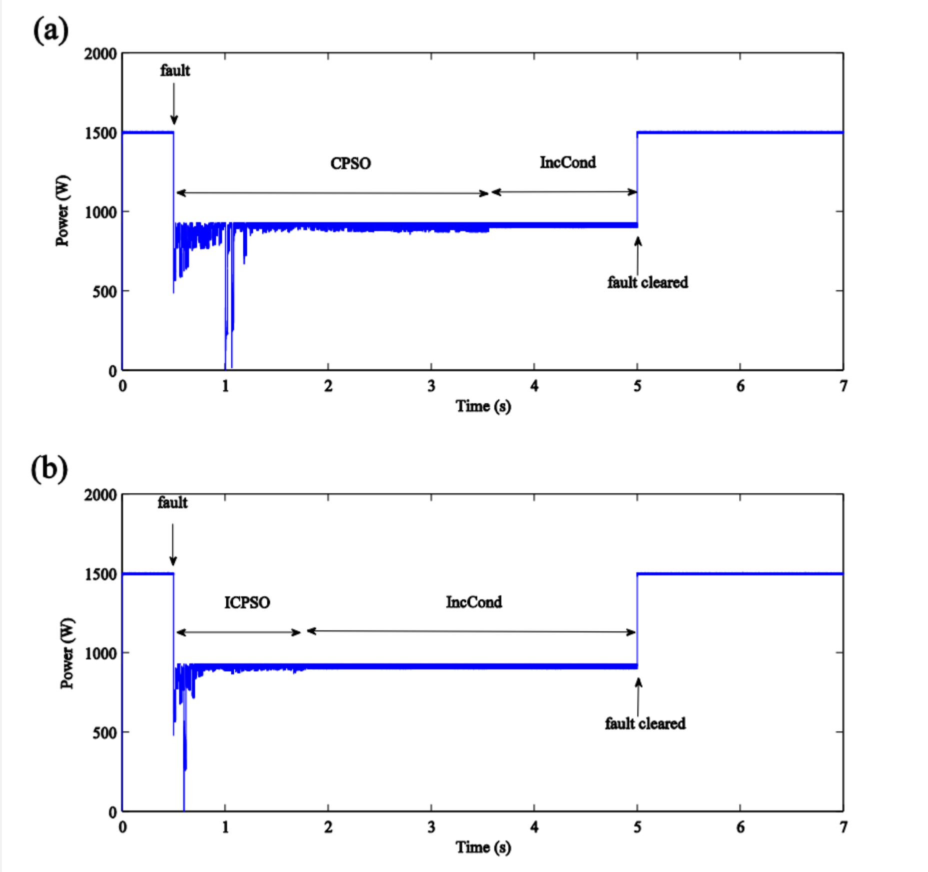

FIGURE 4.6: Power response of the faulted PV array:(a) Current-based PSO (CPSO), (b) Improved CPSO (ICPSO).

Where N is the number of particles in the swarm. The position of each particule x_i is updated as follows:

$$x_i^{k+1} = x_i^k + v_i^{k+1} \tag{4.12}$$

$$v_i^{k+1} = w \cdot v_i^k + c_1 \cdot rand_1 \cdot \left(P_{best_i}^k - x_i^k\right) + c_2 \cdot rand_2 \cdot \left(G_{best}^k - x_i^k\right) \tag{4.13}$$

Where v_i is the velocity of the displacement, w is the learning factor, c_1 and c_2 are positive constants that gives the ponderation of convergence towards the Personal best position (P_{best}) and Group best position (G_{best}) respectively. $rand_1$ and $rand_2$ are normalized random numbers (between 0 and 1).

The values of the parameters of the PSO algorithm have a direct effect on its performance. The number of particles is the first parameter to be defined

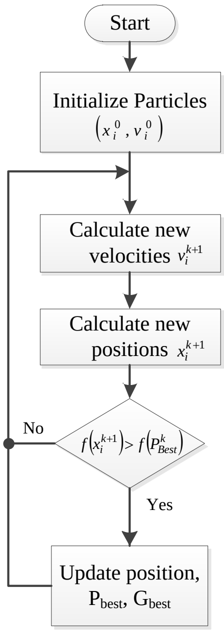

FIGURE 4.7: PSO algorithm flowchart.

as it depends on the size of the space of search. In a previous work, the authors in [27] studied the effect of the number of particles on the performance of an MPPT algorithm where an optimal number of three (03) particles is found. The parameters w, c_1 and c_2 are determined experimentally. The adequate values for our application are 0.4, 1 and 1.6 respectively. These values give a priority to the performance of the group in order to track the global MPP by exploring the space of all possible solutions. The objective function to be maximized is the power given by the PV panel

$$F_i(k) = max(P_{pv}^k) \tag{4.14}$$

The position of any particle is updated only if the new position is greater than its personal best position (P_{best}) (Figure 4.7). Such approach was used in previous research works [50], [27] to evaluate the performance of particles at each iteration. As the PSO algorithm was used without stopping criteria, its convergence is not guaranteed. In this work we add convergence test to maintain the stability of the algorithm and allow better stability. We define a fitness function as follows:

$$fitness(k) = ||F(k)|| \tag{4.15}$$

The fitness function will be used as the evaluation of the swarm instead of F that represents the evaluation of each particle at a given iteration k.

4.4 Simulation results

The fault tolerant algorithm is applied to control the PV array presented in Chapter 2 under faulted conditions. The following simulation scenarios are considered:

- **Scenario 1**:
  When the simulation starts, the PV array is healthy and the Incremental conductance is executed to track the MPP. At the time instant ($t = 0.5s$), a Line-Ground fault is introduced by connecting the nodes of some PV panels to the ground until when ($t = 5s$) where the fault is cleared.
  When the fault is introduced at ($t = 0.5s$), the response of the PV system is given in figure 4.8 (a). The controller starts the optimization procedure in which the global maximum power point is tracked by exploring the space of all possible solutions (figure 4.9 (a)).
  When convergence is reached, the IncCond MPPT algorithm takes control and stabilizes the system around the global MPP (figure 4.8). A comparison with the classical IncCond algorithm shows that the efficiency of the PV array is improved by 36% when using the proposed method(see Table 4.1). When the fault is cleared, both MPPT algorithms converge to the MPP.

- **Scenario 2**:
  The Line-Line fault is introduced at ($t = 0.5s$) by a short-circuit between the nodes of some PV panels until when ($t = 5s$) where the healthy state

of the PV array is restored.

The FDI procedure detects the fault when it is introduced at ($t = 0.5s$) and launches the current-based PSO (ICPSO) MPPT algorithm to track the global MPP (see figure 4.8 (b)). The particles converge toward the operating point characterizing the global MPP (figure 4.9 (b)). The results summarized in Table 4.1 show a gain in efficiency of 4.95% compared to the classical MPPT algorithm.

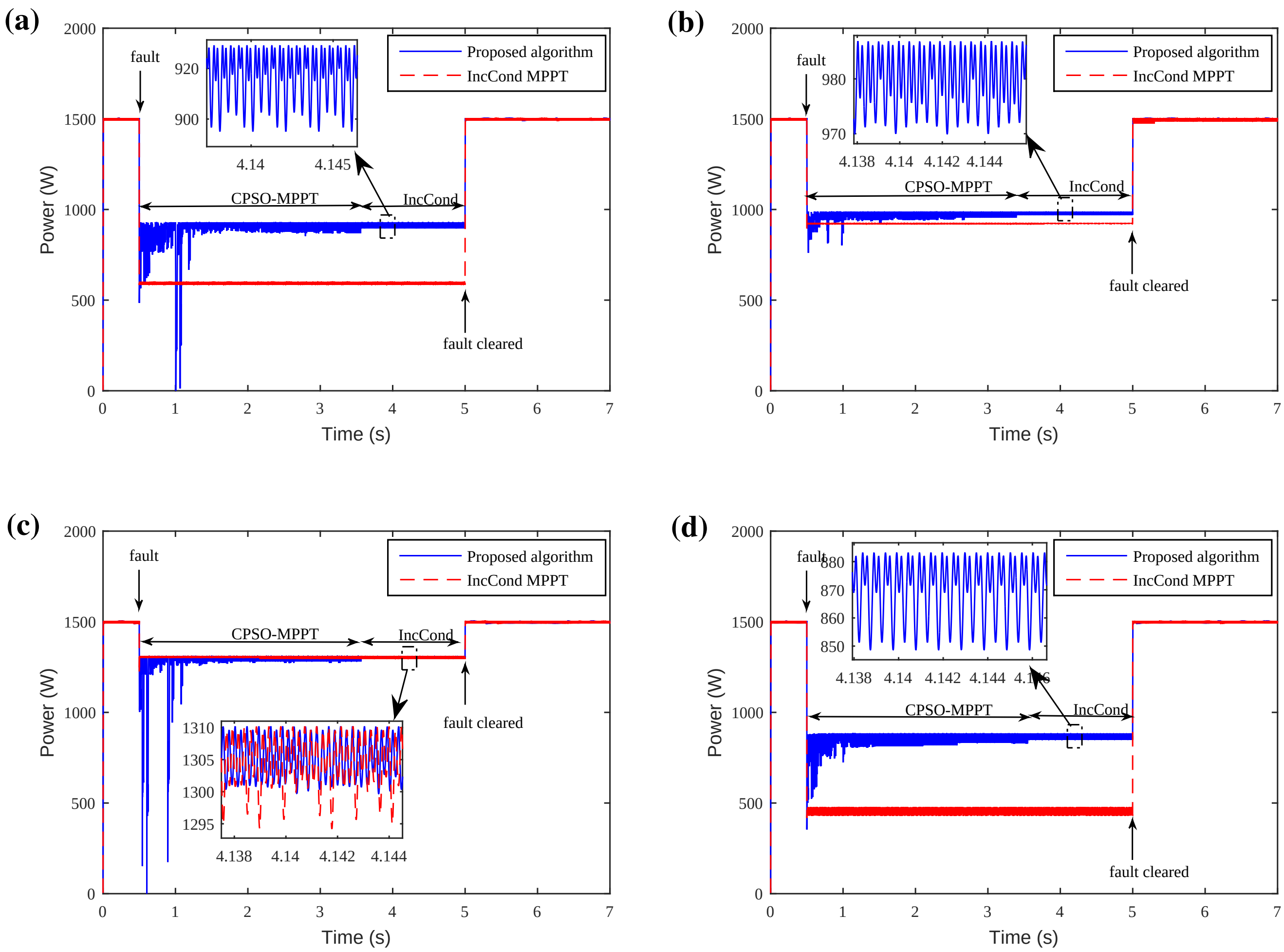

FIGURE 4.8: PV array output power in the presence of various faults: (a) line-ground, (b) line-line, (c) mismatch, (d) partial shading.

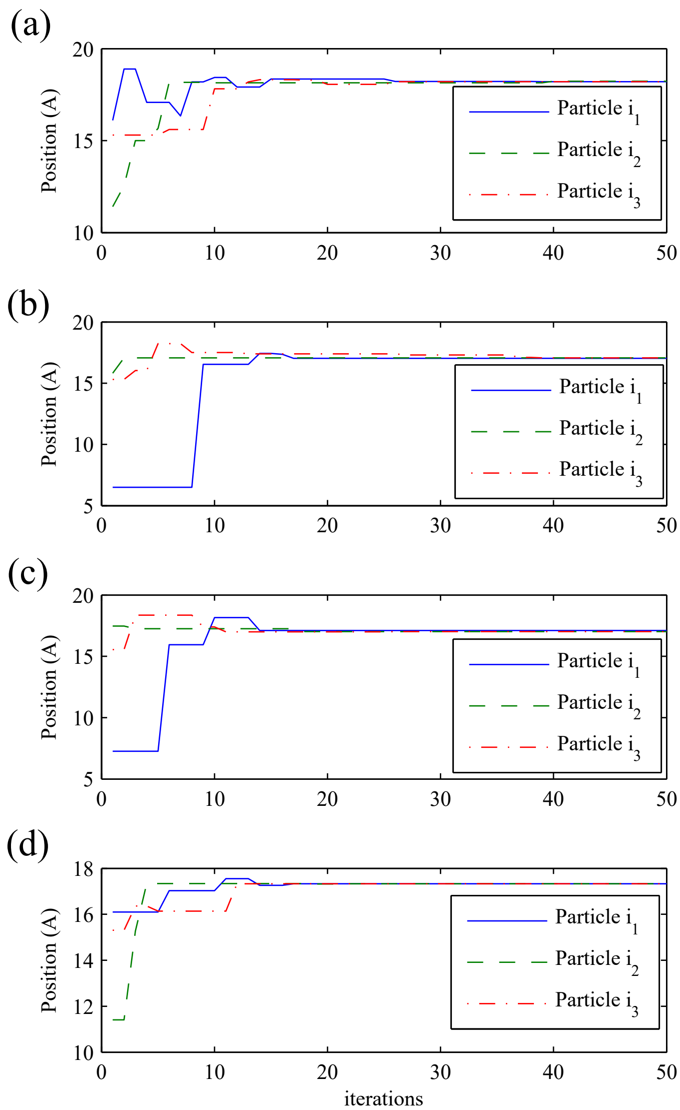

FIGURE 4.9: Evolution of the swarm particles.

- **Scenario 3**:

  The mismatch fault is introduced at ($t = 0.5s$) by modifying the parallel and series resistances of a PV panel. The healthy state of the PV array is restored at ($t = 5s$).

  In figure 4.8 (c), the response of the PV system to a mismatch fault shows the convergence of both MPPT algorithms to the global MPP. The transient spikes in the PSO-based method are caused by the initial search procedure that explores the space of possible solutions to find the global MPP (figure 4.9 (c)).

TABLE 4.1: Maximum Power Points (MPP) of the faulted PV array

PV Array	IncCond		Proposed FTC		Gain in power	Efficiency
	$I_{pv}(A)$	$P_{pv}(W)$	$I_{pv}(A)$	$P_{pv}(W)$	$\Delta P(W)$	$\Delta\eta\%$
Line-ground	07.33	591.55	17.29	924.28	332.73	36
Line-line	10.56	923.79	16.73	971.85	48.06	04.95
Mismatch	18.20	1296.6	16.94	1301.5	04.90	0.37
Partial shading	05.27	476.03	17.64	881.88	405.85	46.02

- **Scenario 4**:

  The value of the solar irradiation is modified for a group of PV panels in order to simulate a partial shading at ($t = 0.5s$) until ($t = 5s$), then the healthy state is restored.

  PV arrays are most of the time subject to temporary partial shading that alters its normal operation during a limited period of time. In this case, the proposed fault-tolerant control is the most effective. In fact, the transitions between faulted and normal states are difficult to manage using classical MPPT algorithms. Even PSO-based MPPT algorithm, when used alone, has to be reinitialized in order to be able to search all the range of possible solutions for the global MPP. The effect of transient poor performance caused by this search operation can be avoided when passing to the normal operation of the PV array by switching to the IncCond MPPT algorithm. This proposed technique gives a smooth transition to the new operating point. The results of the application of the fault-tolerant MPPT algorithm to this type of fault are shown in figure 4.8 (d). The efficiency of the PV array is improved by 46% which is a considerable gain in power (Table 4.1).

4.5 Summary

Fault tolerance is applied in its both passive and active approaches to mitigate sensor faults and environment induced faults. In the passive sensor fault tolerant control law, the drift in sensor signal has been introduced in the design stage in order to cancel its effect when appeared. When a fault affects the components of the PV installation such as modify its wiring network, the consequence on the performance cannot be taken into consideration in the design stage as its nature and form are unknown. In this case, a reconfigurable controller based on the evolutionary PSO technique has been used to guide the controlled system to a suboptimal operating point.

Chapter 5

Experimental tests of the fault-tolerant strategy

5.1 Introduction

The proposed fault-tolerant strategy is implemented in an experimental setup composed of a developed prototype of the boost DC-DC converter, a DSP controller, a power interface and a solar simulator. The previously used I-V and P-V characteristic curves have been implemented in the solar simulator. The main advantage of using a solar simulator is its ability to reproduce the loaded I-V curves of the faulted PV array in the form of electrical voltage and current.

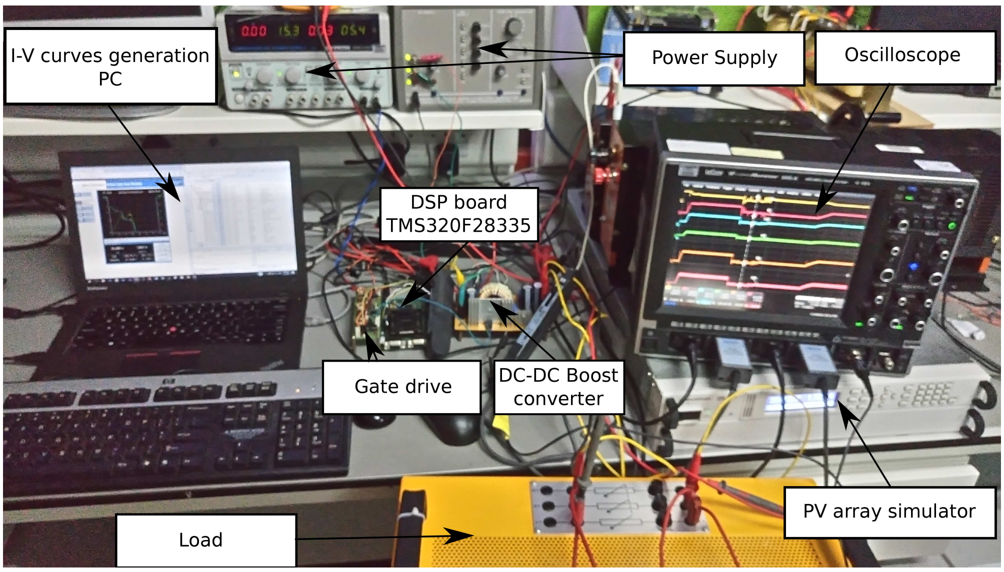

FIGURE 5.1: Experimental setup.

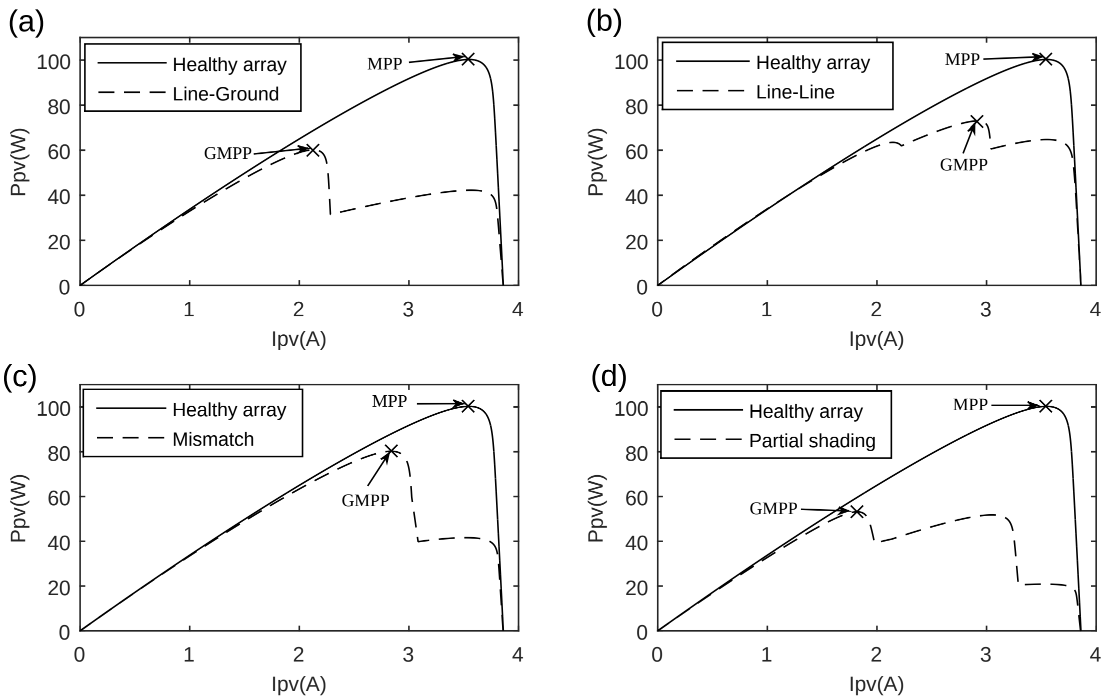

FIGURE 5.2: Experimental P-I curves for different faulted conditions: (a) line-ground fault, (b) line-line fault, (c) mismatch fault, (d) partial shading fault.

5.2 Description of the experimental setup

The experimental setup is presented in Figure 5.1. An $Agilent E4360A$ PV array simulator is used to generate I-V curves for the following experiments. Different faulted scenarios are simulated in MATLAB/Simulink (Figure 5.2), then I-V curves for normal and faulted conditions are loaded into the internal memory of the PV simulator using ethernet interface to generate the corresponding current and voltage values. The I-V curves are implemented at reduced power scale (1:15) of the PV array presented in previous sections; the resulting PV array has a rating of 100W at STC conditions.

The DSP controller used to implement the proposed algorithm is the Texas Instruments C2000 series ($TMS320F28335$) is characterized by 150MHZ processor, a 12bit ADC and multiple PWM output ports. The voltage and current measurements are acquired using a conditioning circuit and then are fed to the 12 bit ADC of the DSP. The PWM signal generated at 40KHz by the DSP controller is fed to a gate driver circuit before it gets to the MOSFET gate. The developed DC-DC boost converter prototype has the following characteristics: input capacitor ($C_{in} = 1000\mu F/100V$), inductor ($250\mu H/8A$), output capacitor ($C_{out} = 2 \times 250\mu F/200V$), ($R_Load = 100\Omega$). The measurement of input and output variables were made using $Lecroy64Xi - A$ oscilloscope with additional differential probes. In order to make comparison between the performances of two algorithms, experimental data were saved from the oscilloscope and then plotted using the MATLAB software. The following experiments are conducted in STC $G = 1000W/m^2, T = 25^oC$).

5.3 Experimental implementation using a DSP microcontroller

Initially, the PV array is operated in normal operating conditions, the FTC algorithm implemented on the DSP tracks the MPP (Figure 5.3) located at the operating point ($Impp = 3.55A, Pmpp = 100.27W$). At the time instant ($t = 15s$), faults are introduced by loading the I-V curve of the simulated fault into the solar array simulator. Then the original I-V curve is restored at the time ($t = 30s$).

5.3.1 Line-Ground fault

In the first scenario, Line-Ground fault was introduced at ($t = 15s$) the IncCond algorithm converges to a local maximum power point (LMPP) mainly because of the current value of the LMPP is close to the previous operating point at MPP in normal operating conditions (figure 5.4). Figure 5.3 shows the evolution of input/output variables for the proposed FTC algorithm. After the introduction of the fault, the ICPSO algorithm is launched and GMPP is tracked in 1.94 seconds with additional effeciency of 31.8% (Table 5.1). When the fault is cleared, IncCond algorithm tracks the new MPP.

TABLE 5.1: Experimental performance of the proposed FTC algorithm in faulted operating conditions

PV Array	IncCond		Proposed FTC		Gain in power	Efficiency
	$I_{pv}(A)$	$P_{pv}(W)$	$I_{pv}(A)$	$P_{pv}(W)$	$\Delta P(W)$	$\Delta\eta\%$
Line-ground	03.69	41.03	02.24	60.16	19.13	31.8
Line-line	03.83	63.24	03.01	72.99	48.06	13.36
Mismatch	03.71	39.08	03.06	78.92	39.84	50.48
Partial shading	03.25	49.47	01.99	51.09	01.62	03.17

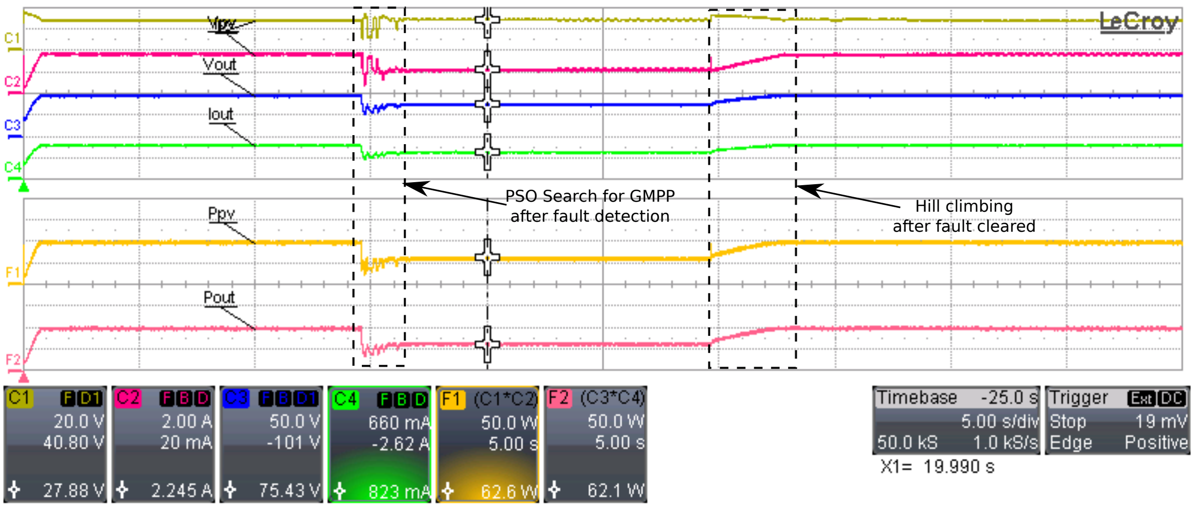

FIGURE 5.3: Performance of the proposed FTC algorithm in the presence of line-ground fault.

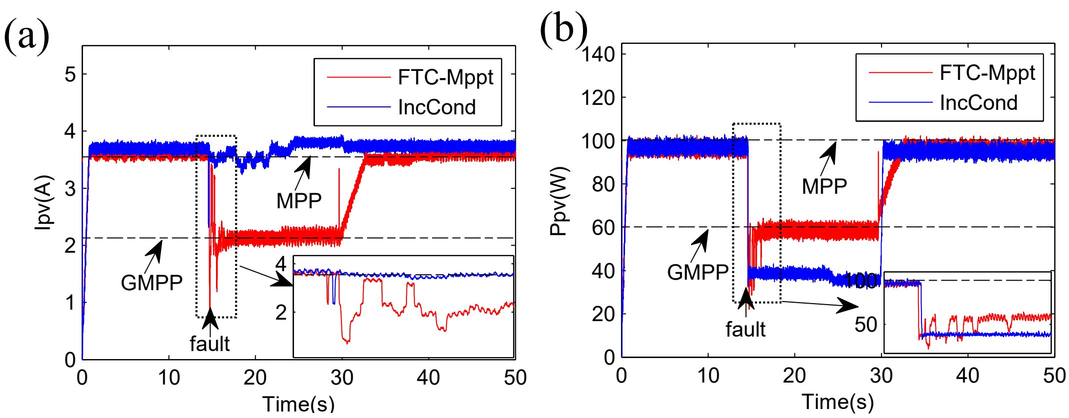

FIGURE 5.4: Comparison of the proposed FTC algorithm with InCond MPPT in the presence of line-ground fault: (a) PV current, (b) PV power.

5.3.2 Line-Line fault

Line-Line fault is introduced in the second scenario; the IncCond tracks a local MPP with almost no change in current measurement (figure 5.5). The proposed FTC tracks GMPP in 5.82 seconds (Figure 5.6) due to the presence of multiple MPP in the P-I curve but with additional efficiency of 13.36%.

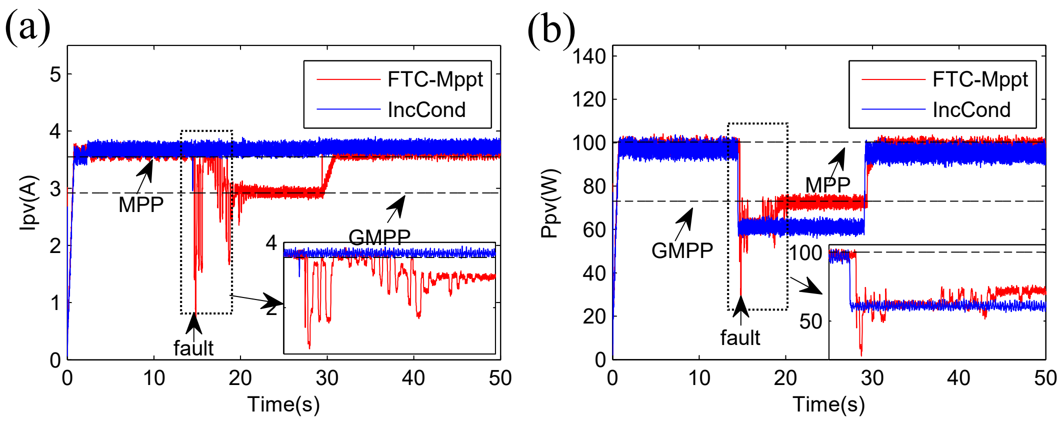

FIGURE 5.5: Comparison of the proposed FTC algorithm with InCond MPPT in the presence of line-line fault: (a) PV current, (b) PV power.

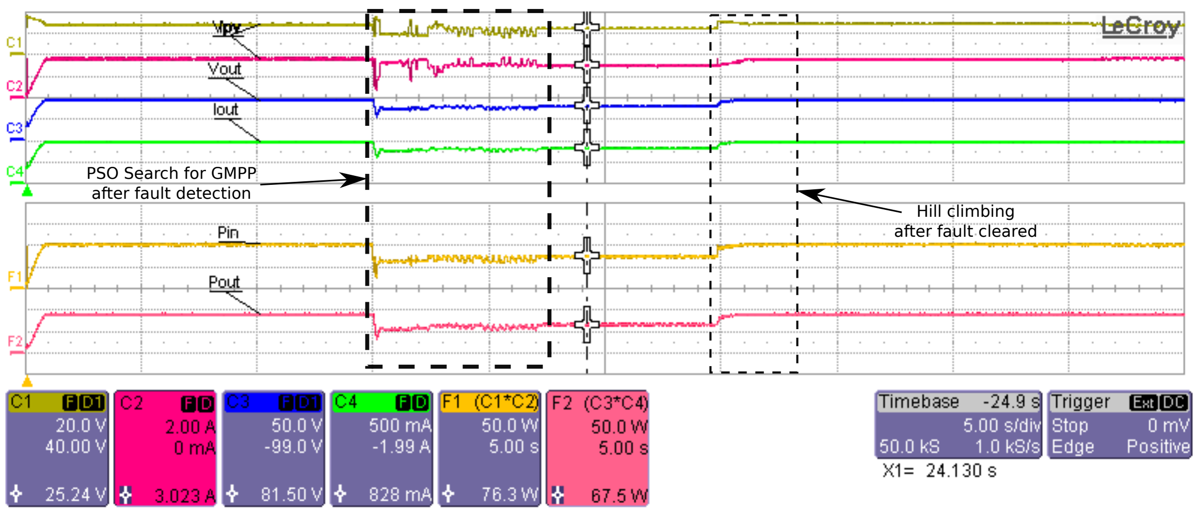

FIGURE 5.6: Performance of the proposed FTC algorithm in the presence of line-line fault.

5.3.3 Mismatch fault

The mismatch fault is simulated in the third scenario; the IncCond algorithm tracks an MPP with low power value (figure 5.7). The ICPSO algorithm tracks the global MPP in 2.35seconds (Figure 5.8) with the best gain in power of 50%.

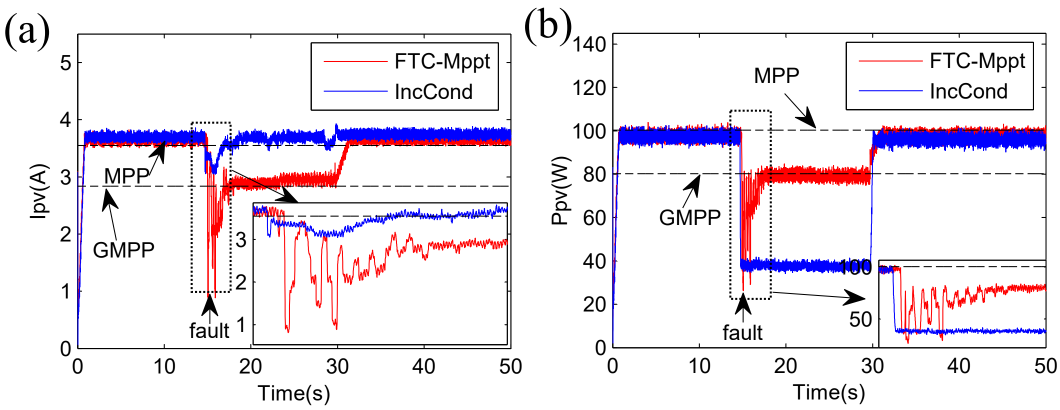

FIGURE 5.7: Comparison of the proposed FTC algorithm with InCond MPPT in the presence of mismatch fault: (a) PV current, (b) PV power.

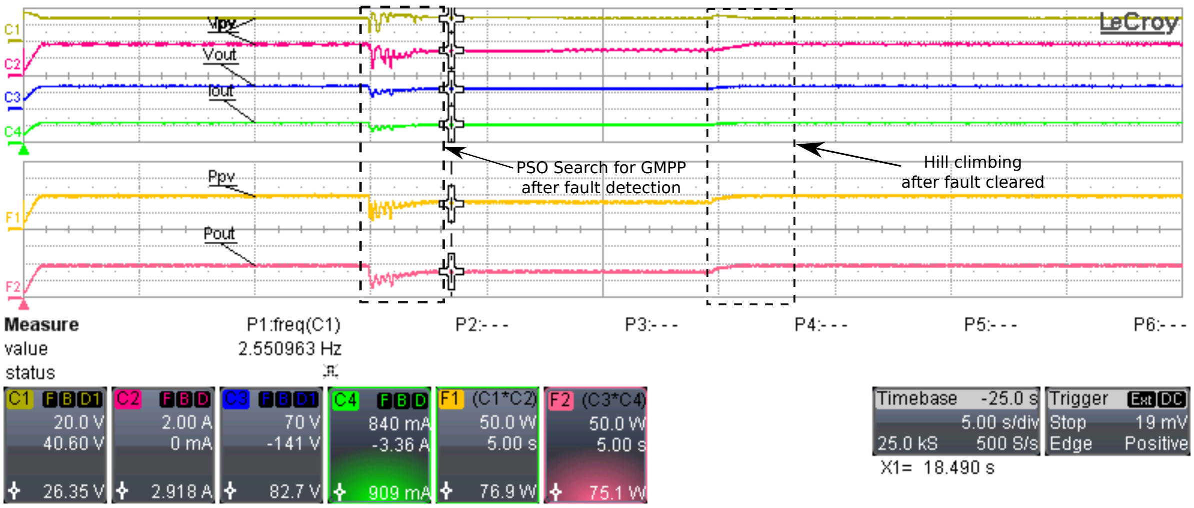

FIGURE 5.8: Performance of the proposed FTC algorithm in the presence of mismatch fault.

5.3.4 Partial shading fault

Partial shading is introduced in the last scenario, the efficiency of the two algorithms is almost identical with additional 03.17% (Table 5.1) given the small difference between MPP (figure 5.2(d)) whereas the current measurement operating point is different (figures 5.2(d) and 5.9(a)). The ICPSO-based algorithm tracks the GMPP in 3.9 seconds (figure 5.10).

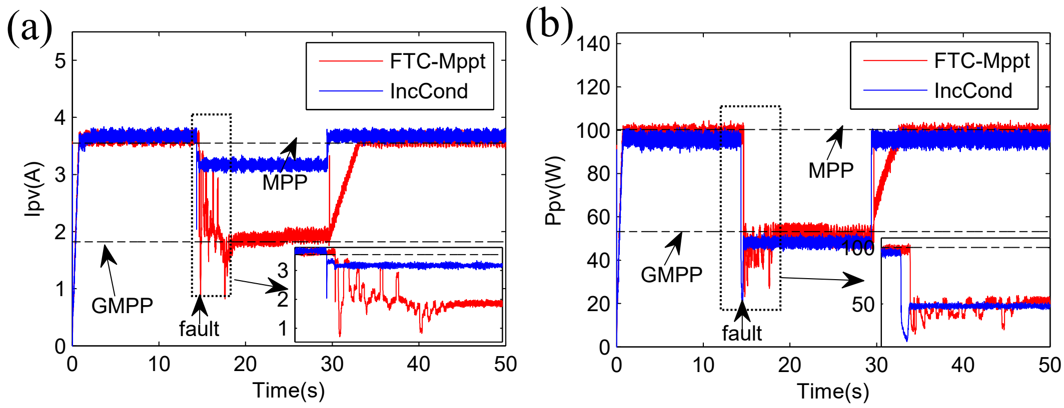

FIGURE 5.9: Comparison of the proposed FTC algorithm with InCond MPPT in the presence of partial shading: (a) PV current, (b) PV power.

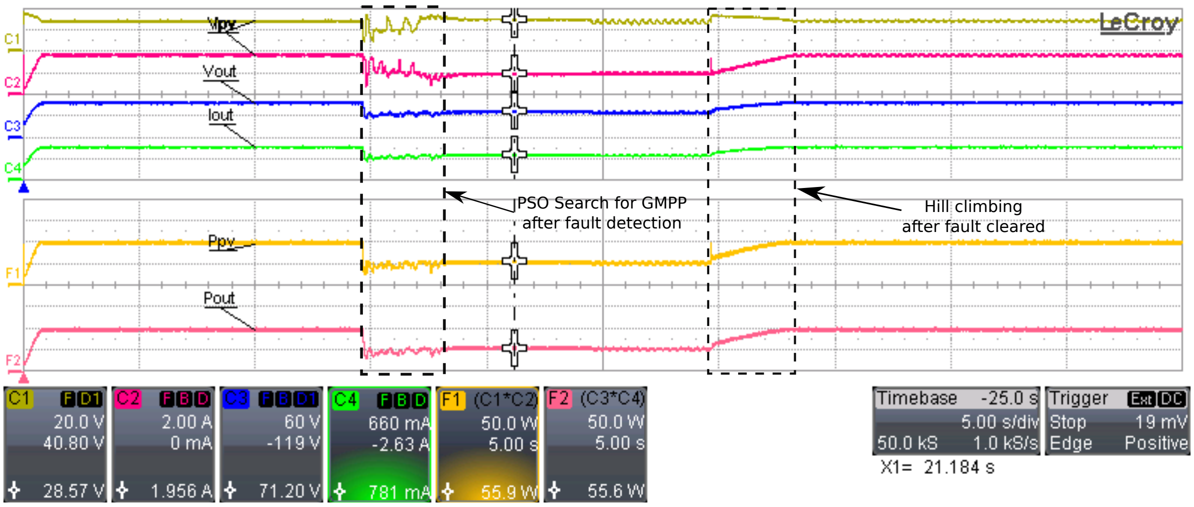

FIGURE 5.10: Performance of the proposed FTC algorithm in the presence of partial shading.

5.3.5 Load change robustness test

The robustness of the proposed approach is tested by applying a 50% step change in the load. Figure 5.11 shows the response of the proposed FTC method to a load step change. The current regulation keeps tracking the MPP whereas a change in output current and voltage has occurred to compensate the change in load.

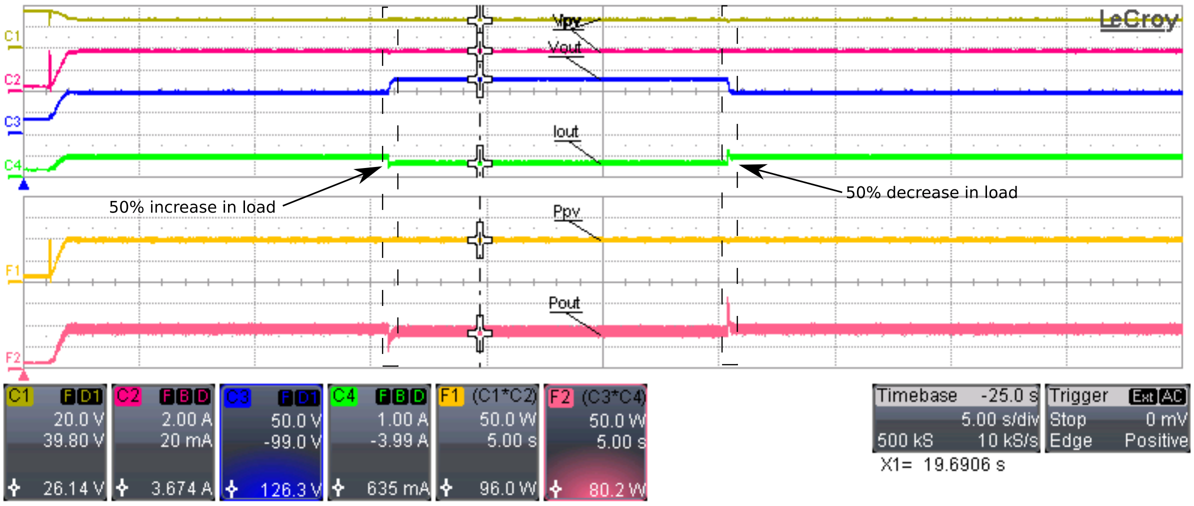

FIGURE 5.11: Performance of the proposed FTC algorithm in the presence of load change.

5.4 Summary

The fault-tolerant power extraction strategy has been implemented in an effective experimental setup that allows indoor simulation of different types of faults in addition to a fast processing microcontroller that allows the implementation of complex control algorithms. The obtained results show the effectiveness of the proposed FTC strategy in dealing with intermittent faults with good transient performance.

Chapter 6

Conclusion

Solar PV arrays are widely used in isolated areas where a local power management system has to be present to maximize their efficiency in the presence of weather disturbances and various types of faults.

The proposed fault-tolerant approach is model-free, that can be implemented in real-time, and that uses only current and voltage sensors. The algorithm improves the performance of the PV arrays and allows tolerance to different types of faults. Using the current of the PV array as control variable reduces the search space for the PSO algorithm and gives additional robustness to load variations. Simulation and experimental results show the effectiveness of the fault-tolerant MPPT algorithm in handling intermittent faults with improved transient performance and a considerable gain in power. The proposed fault tolerant strategy has the following advantages:

- Detection of abrupt changes not detectable by over current protection devices
- May be used mainly for standalone photovoltaic energy generation systems
- Improves the performance of PV arrays with tolerance to different types of faults
- The choice of input current as control variable reduces the search space
- The choice of input current as control variable gives robustness to load change

- Handling intermittent faults with improved transient performance.

As perspectives, the scheme presented in this study can easily be modified to enhance its performance:

- Implement other swarm based optimization algorithms in order improve the transient response of the PV system,
- The hard switching in the proposed scheme may be replaced with soft switching,
- Multiple local controllers may be designed according to the operating region,
- Other fault-tolerant control schemes may be implemented using the state space modeling and the LMI approach.

Appendix A

Simulation of faulted PV array

A.1 Faults simulation in the PV array under Simulink

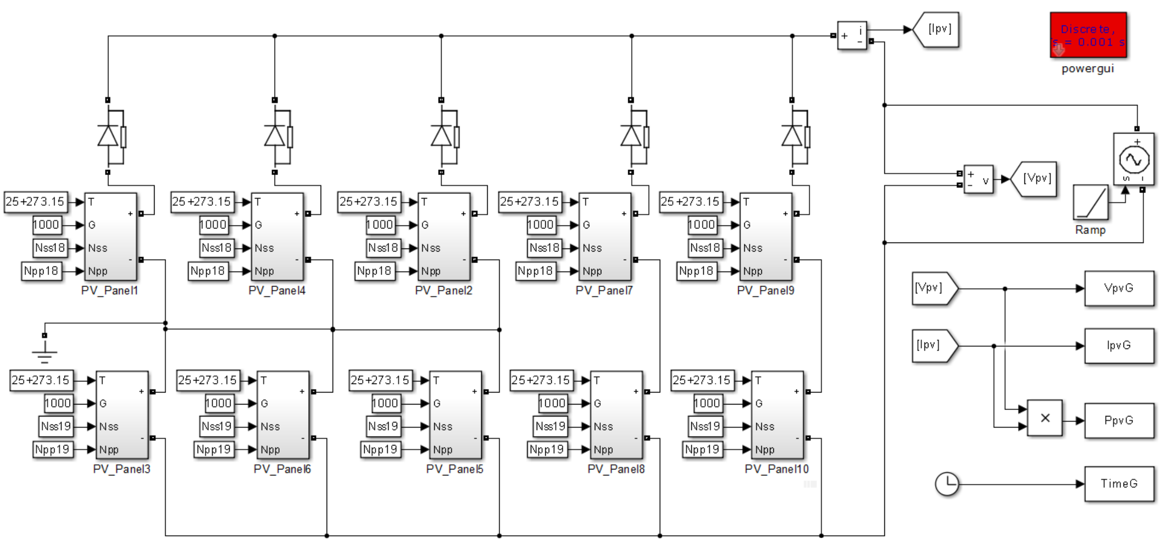

FIGURE A.1: Simulation model of the faulted PV array (line-ground fault).

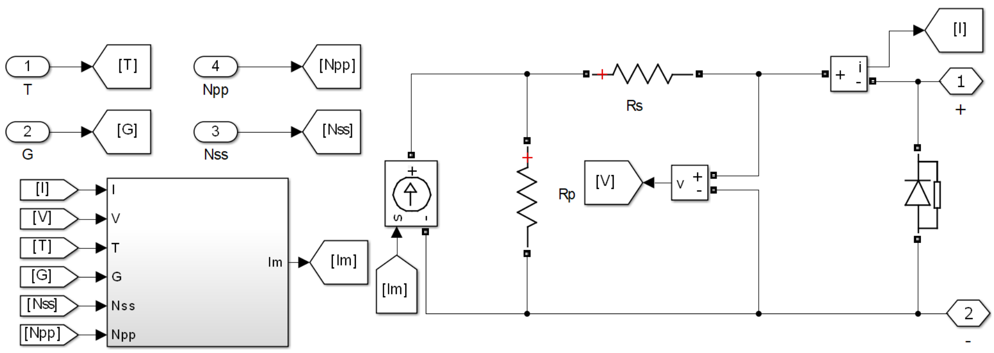

FIGURE A.2: Simulation model of the PV array subsystem.

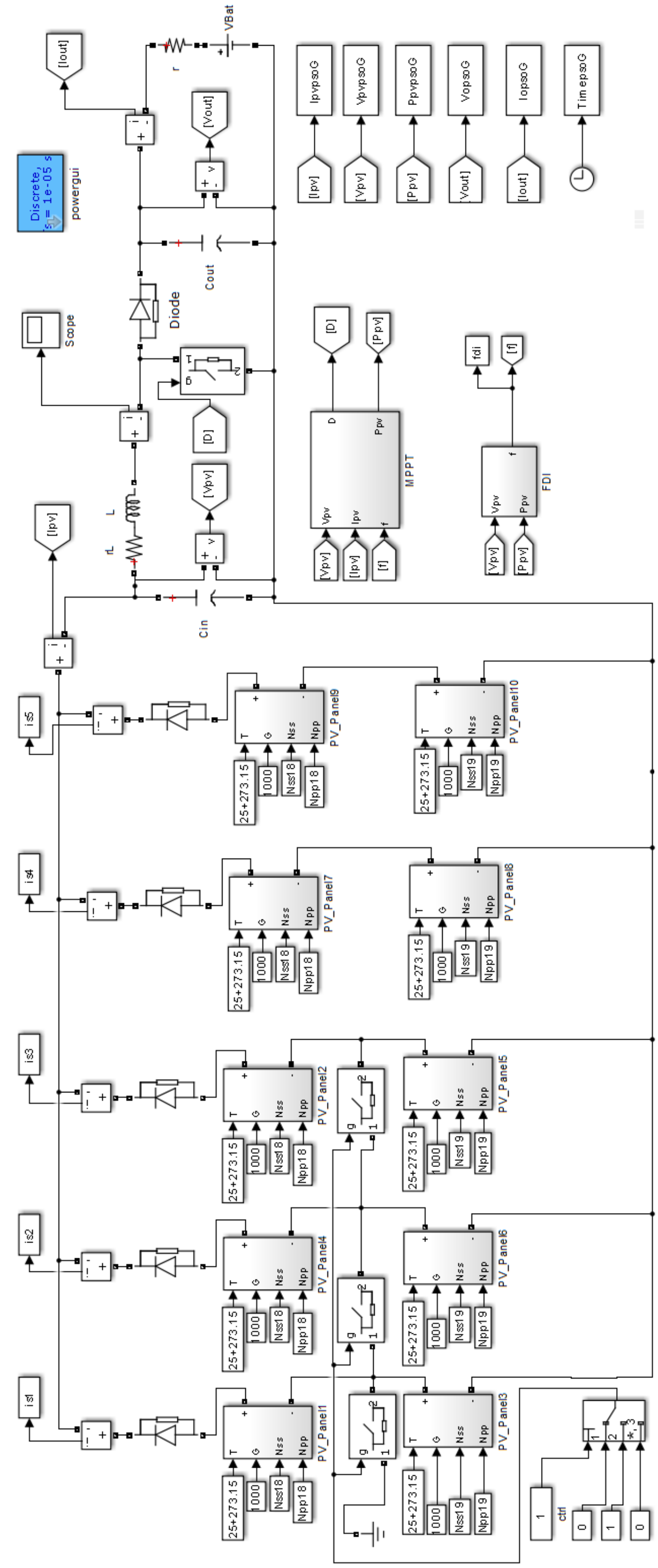

FIGURE A.3: Simulation model of the controlled PV array.

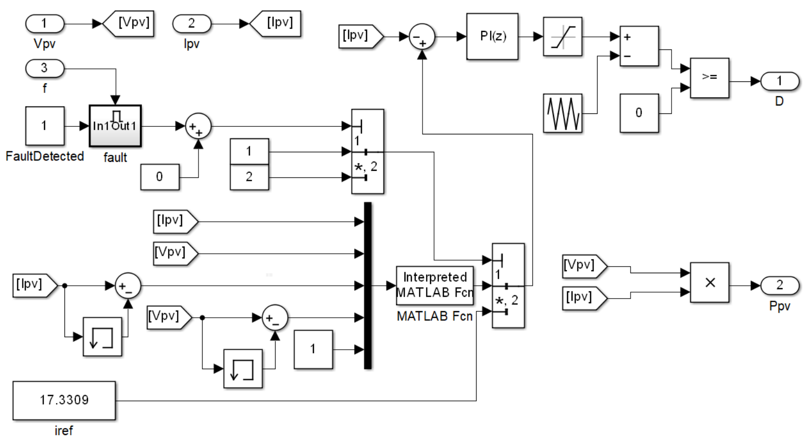

FIGURE A.4: Fault-tolerant control of faulted PV array.

Appendix B

Experimental setup description

B.1 Measurement and control setup description

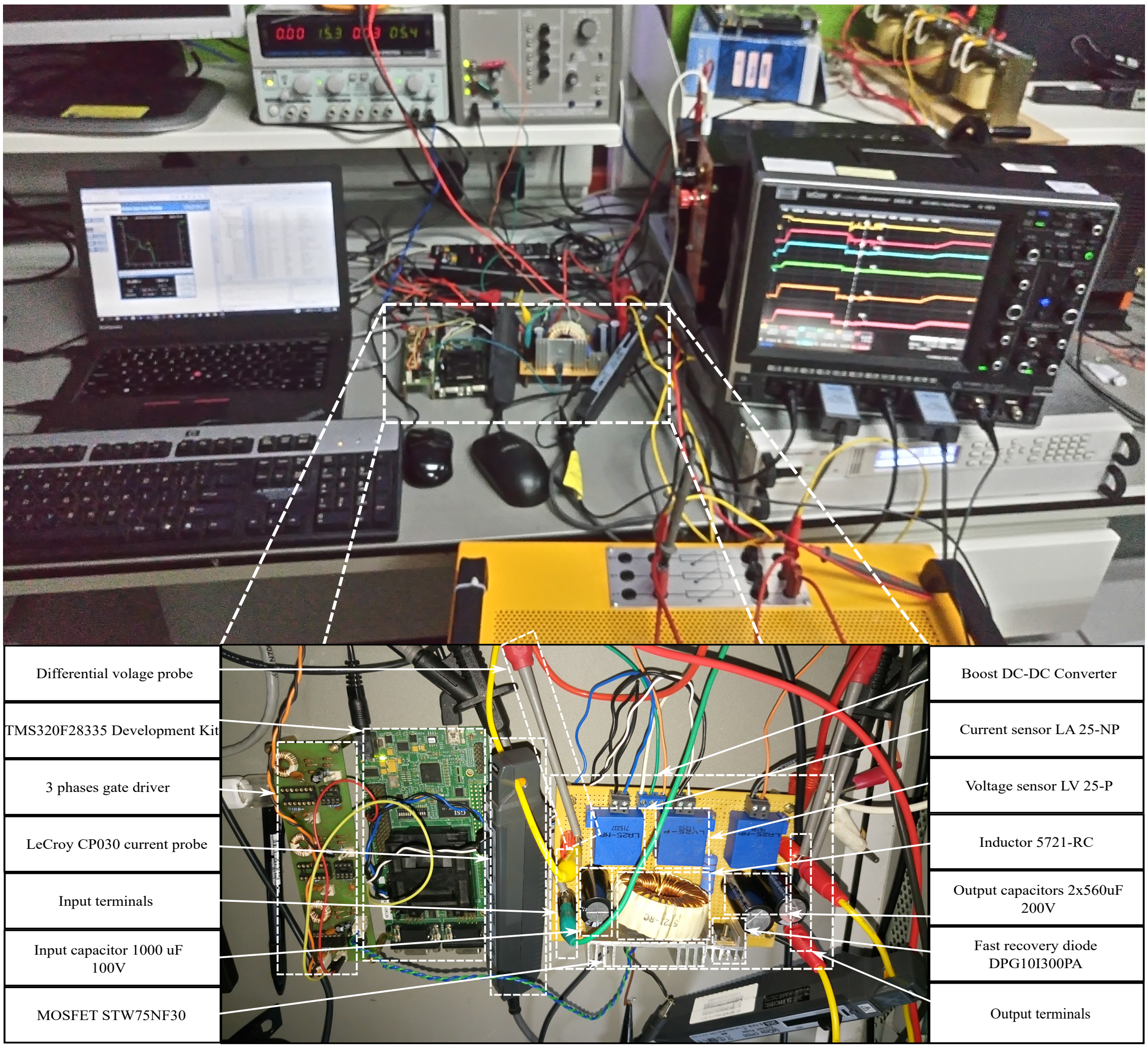

FIGURE B.1: Measurement and control setup.

The boost DC-DC converter is equipped with input and output current sensors (*LA 25-NP*) in addition to the input voltage sensor (*LV 25-P*) that are fed by a dual symmetrical power supply ($\pm 15V$) with their outputs connected the ADC channels of the DSP. The gate of the MOSFET switch is controlled by the *DSC TMS320F28335* using a 3 phases gate driver in which we use only one phase. The gate driver is fed by a $5V$ power supply. The input and output currents are analyzed and recorded in the oscilloscope using *LeCroy CP030* current probes that are connected to the channels 2 and 4 of the oscilloscope *Lecroy64Xi-A*. The input and output voltages are acquired in the oscilloscope using *PINTEK DP-25* differential voltage probes that are connected to the channels 1 and 3 respectively.

B.2 Characteristics of the eZdspF28335

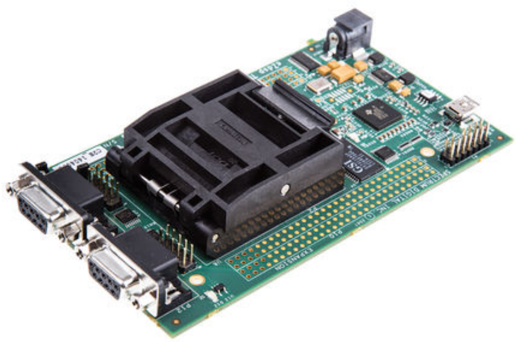

FIGURE B.2: eZdspF28335 development board.

The eZdspF28335 development board allows fast prototyping of DSP based applications as the board provides several expansion connectors allowing easy access to internal peripherals such as ADC, PWM,...etc. The following hardware features are given:

- 150 Mhz operating speed
- On chip 32-bit floating point unit
- 68K bytes on-chip RAM
- 512K bytes on-chip flash memory

- 256K bytes off-chip SRAM memory
- On-chip 12 bit ADC with 16 input channels
- 30 Mhz input clock
- On board RS-232 connector with line driver
- On board CAN 2.0 interface with line driver and connector
- Multiple expansion connectors (analog I/O)
- On board embedded USB JTAG controller
- 5-volt only operation with supplied AC adapter
- On board IEEE 1149.1 JTAG emulation connector

The software features associated with this board are:

- TI F28xx Code Composer Studio (CCS) Integrated Development Environment (IDE), version 3.3
- TI Flash APIs to support the F28335
- TI F28335 header files and example software

The PWM module is located at the connector $P8$ as highlighted in figure B.3. The $P8$ connector pin definition is given in Table B.1. The ADC module is

TABLE B.1: PWM modules in P8 connector of the eZdspF28335

Pin#	Signal		Pin#	Signal
1	+3.3V/+5V/NC		2	+3.3V/+5V/NC
3	MUX_GPIO29_SCITXDA_XA19		4	MUX_GPIO28_SCIRXDA_XZCS6n
5	GPIO14_TZ3n_XHOLD_SCITXDB_MCLKXB		6	GPIO20_EAEP1A_MXDA_CANTXB
7	GPIO21_EQEP18_MDRA_CANRXB		8	GPIO23_EQEP1_MFSXA_SCIRXDB
9	GPIO0_EPWM1A		10	GPIO1_EPWM1B/ECAP6/MFSRB
11	GPIO2_EPWM2A		12	GPIO3_EPWM2B_ECAP5_MCLKRB
13	GPIO4_EPWM3A		14	GPIO5_EPWM3B_MFSRA_ECAP1
15	GPIO27_ECAP4_EQEP2S_MFSXB		16	GPIO6_EPWMN4A_EPWMSYNCI/EPWMSYNCO
17	GPIO13_TZ2N_CANRXB_MDRB		18	GPIO34_ECAP1_XREADY
19	GND		20	GND
21	GPIO7_EPWM4B_MCLKRA_ECAP2		22	GPIO15TZ4n_XHOLDA_SCIRXDB_MFSXB
23	GPIO16_SPISIMOA_CANTXB_TZ5n		24	GPIO17_SPISOMIA_CANRXB_TZ6n
25	GPIO18_SPICLKA_SCITXDB_CANRXA		26	GPIO19_SPISTAn_SCIRXDB_CANTXA
27	_MUX_GPIO31_CANRXA_XA17		28	MUX_GPIO30_CANRXA_XA18
29	MUX_GPIO11_EPWM6B_SCIRXDB_ECAP4		30	MUX_GPIO8EPWM5A_CANTXB_ADCSOCA0nP3
31	MUX_GPIO9_EPWM5B_SCITXDB_ECAP3		32	MUX_GPIO10_EPWM6A_CANRXB_ADCASOCB0n
33	MUX_GPIO22		34	GPIO25_ECAP2_EPEQ2B_MDRB
35	GPIO26_ECAP3_EQEP21_MCLKXB		36	GPIO32_SDAA_EPWMSYNCI_ADCSOCAOn
37	GPIO12_TZ1N_CANTXB_MDXB		38	GPIO33_SCLA_EPWNSYNCVO_ADCSOCBOn
39	GND		40	GND

located at the connector $P9$ as highlighted in figure B.3. The $P9$ connector pin definition is given in Table B.2.

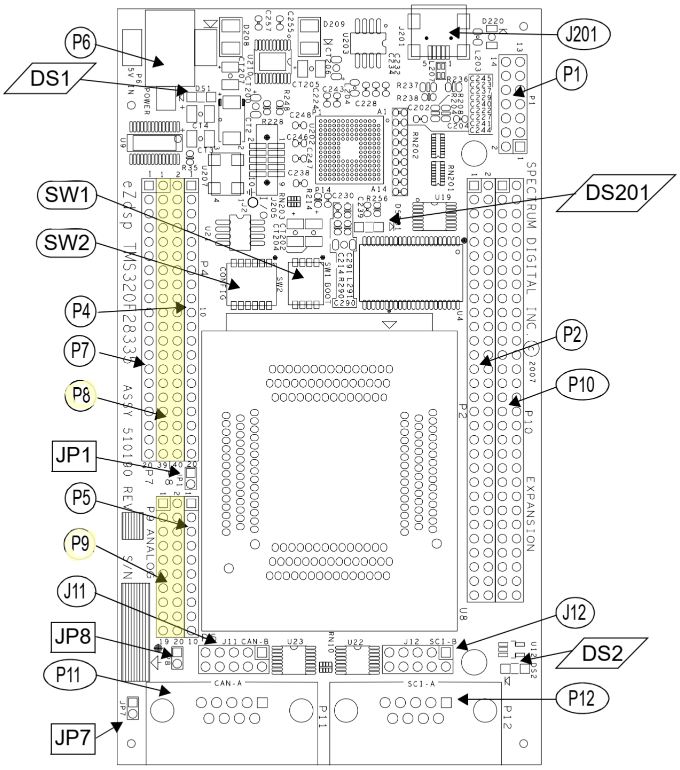

FIGURE B.3: eZdspF28335 printed circuit board.

TABLE B.2: ADC channels in P9 connector of the eZdspF28335

Pin #	Signal		Pin #	Signal
1	GND		2	ADCINA0
3	GND		4	ADCINA1
5	GND		6	ADCINA2
7	GND		8	ADCINA3
9	GND		10	ADCINA4
11	GND		12	ADCINA5
13	GND		14	ADCINA6
15	GND		16	ADCINA7
17	GND		18	ADCLO
19	GND		20	No connect

B.3 Current sensor LA 25-NP

The current sensor LA 25-NP from allows galvanic isolation between the circuit with the current to be measured and the acquisition system (such the ADC of the DSP), the sensor measures AC and DC currents with variable sensitivity. In our case, we will use the sensor as depicted in figure B.4, where the pins 1-5 and 6-10 are shorted, the current flows in the positive direction from i_n to i_p. Such configuration gives a nominal primary current of $25A$ which is sufficient for our application. The measurement resistance R_M should vary between $100 - 320\Omega$, we use a potentiometer for this purpose.

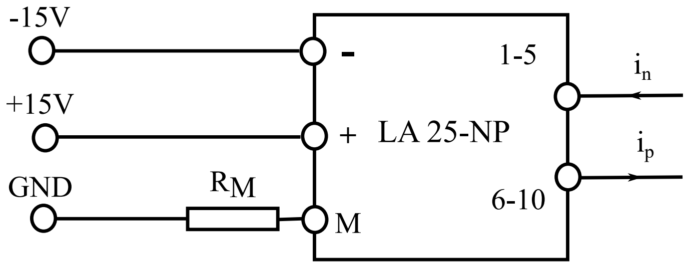

FIGURE B.4: LA 25-NP current sensor description.

B.4 Voltage sensor LV 25-P

The voltage sensor LV 25-P from allows galvanic isolation between the circuit with the voltage to be measured and the acquisition system, the sensor measures AC and DC voltages with variable sensitivity. In our case, we will use the sensor as depicted in figure B.5, where the pins +HV and -HV are connected to the high voltage to be measured. The maximum voltage to be measured is dependent on the choice of the resistor R such that a nominal current of $10mA$ should be present in the primary side. For a maximum voltage of $200V$, a resistor of $R = 20k\Omega$ should be selected. The measurement resistance R_M should vary between $100 - 350\Omega$ in our test conditions, we use a potentiometer for this purpose.

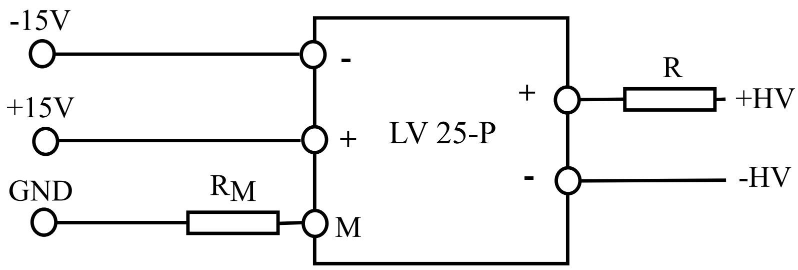

FIGURE B.5: LV 25-P voltage sensor description.

B.5 Gate driver schematics

The gate driver drives the MOSFET according to the incoming PWM signal from the DSP controller, an opto-isolation is provided using the $HCPL3120$ (U2) integrated circuit. The circuit U2 is fed by a constant voltage of 15V issued from a power supply source of 5V using an oscillator circuit as shown in figure B.6.

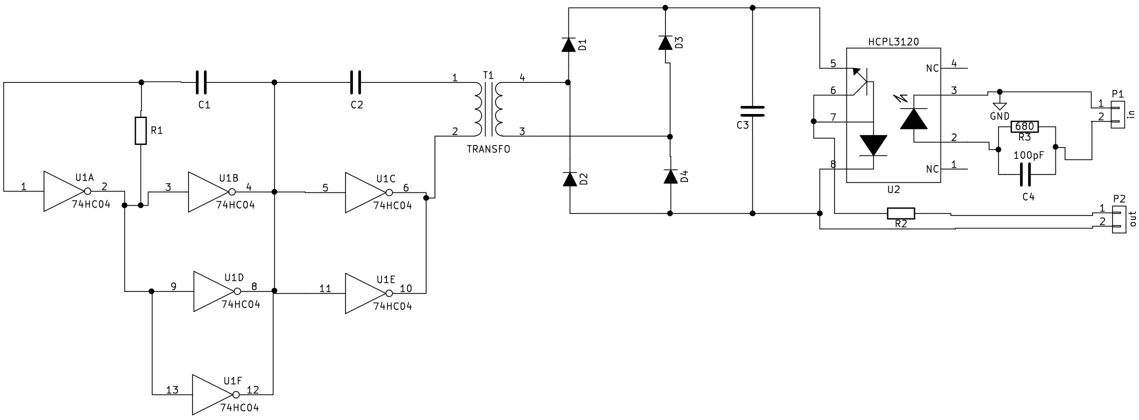

FIGURE B.6: Gate driver schematics.

B.6 Agilent E4360A solar array simulator

FIGURE B.7: Agilent E4360A solar array simulator.

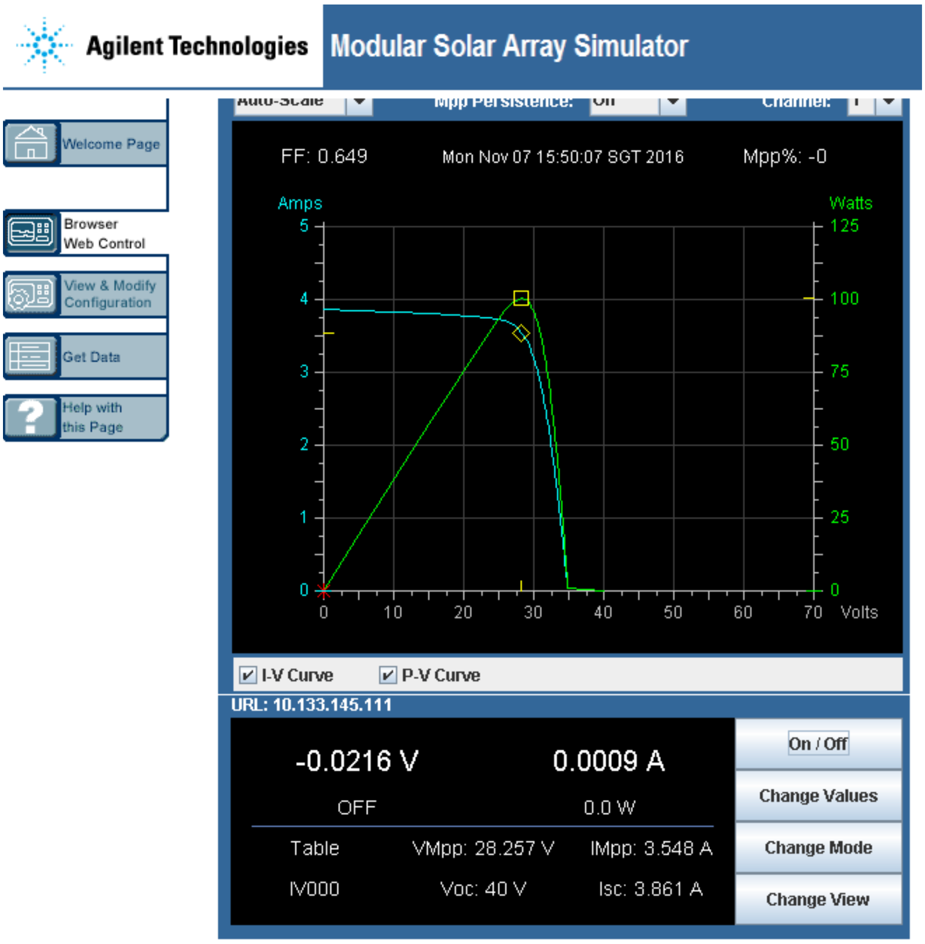

FIGURE B.8: I-V and P-V curves of healthy PV array in Agilent E4360A.

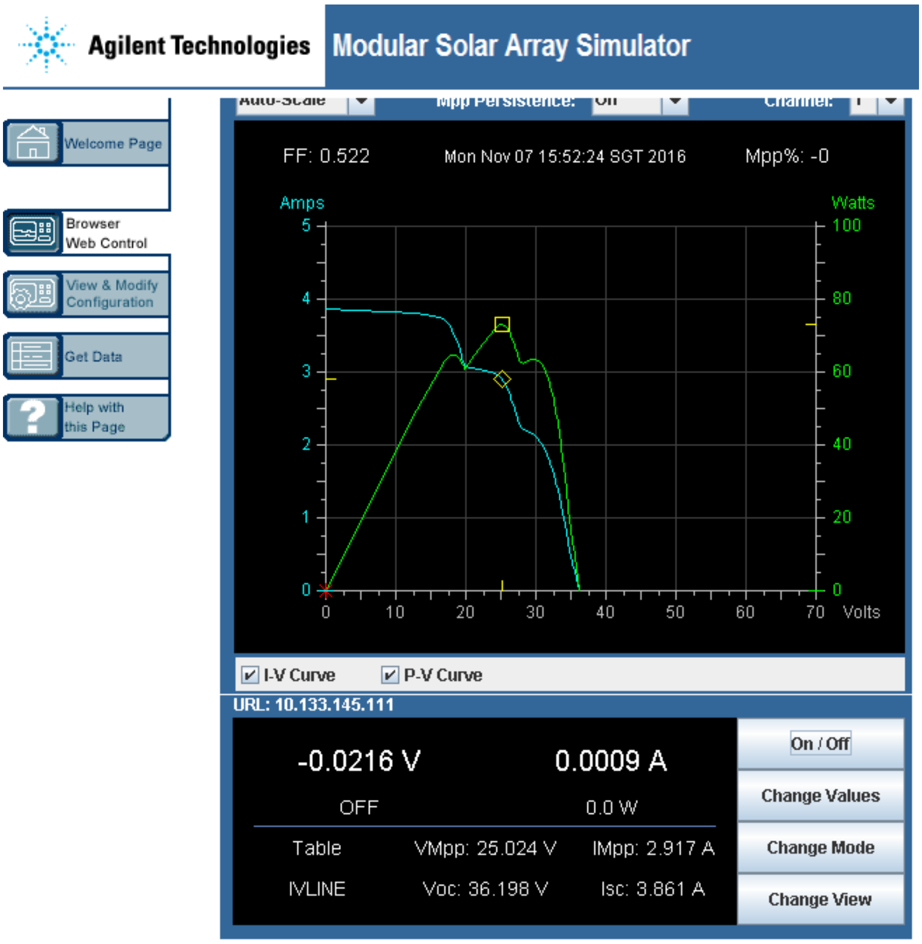

FIGURE B.9: I-V and P-V curves of line-line fault in Agilent E4360A.

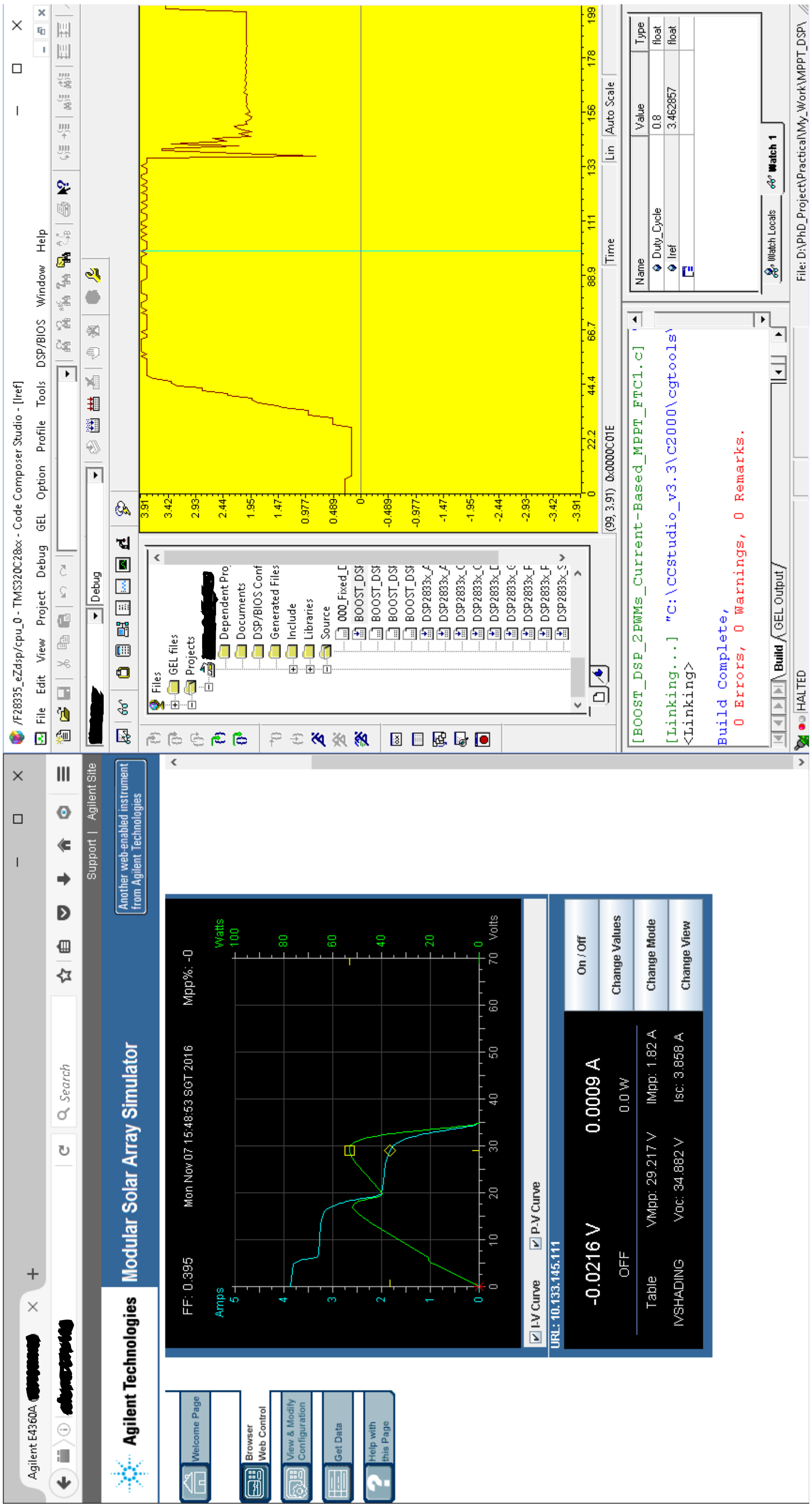

FIGURE B.10: I-V curve generation using Agilent E4360A and DSP debugging using CCS 3.3.

Bibliography

[1] *Renewables 2018*. Market Report Series: Renewables. OECD, 2018. DOI: 10.1787/re_mar-2018-en. URL: https://www.oecd-ilibrary.org/energy/renewables-2018{_}re{_}mar-2018-en.

[2] W. Herrmann and N. Bogdanski. "Outdoor weathering of PV modules - Effects of various climates and comparison with accelerated laboratory testing". In: *2011 37th IEEE Photovoltaic Specialists Conference*. IEEE, 2011, pp. 002305–002311. ISBN: 978-1-4244-9965-6. DOI: 10.1109/PVSC.2011.6186415. URL: http://ieeexplore.ieee.org/document/6186415/.

[3] Ahmed Bouraiou et al. "Analysis and evaluation of the impact of climatic conditions on the photovoltaic modules performance in the desert environment". In: *Energy Conversion and Management* 106 (2015), pp. 1345–1355. ISSN: 01968904. DOI: 10.1016/j.enconman.2015.10.073. URL: https://www.sciencedirect.com/science/article/pii/S0196890415009954.

[4] E.E. van Dyk and E.L. Meyer. "Analysis of the effect of parasitic resistances on the performance of photovoltaic modules". In: *Renewable Energy* 29.3 (2004), pp. 333–344. ISSN: 09601481. DOI: 10.1016/S0960-1481(03)00250-7. URL: http://linkinghub.elsevier.com/retrieve/pii/S0960148103002507.

[5] E.E van Dyk et al. "Long-term monitoring of photovoltaic devices". In: *Renewable Energy* 25.2 (2002), pp. 183–197. ISSN: 09601481. DOI: 10.1016/S0960-1481(01)00064-7. URL: http://www.sciencedirect.com/science/article/pii/S0960148101000647.

[6] Volker Quaschning and Rolf Hanitsch. "Numerical simulation of current-voltage characteristics of photovoltaic systems with shaded solar cells".

In: *Solar Energy* 56.6 (1996), pp. 513–520. ISSN: 0038092X. DOI: 10.1016/0038-092X(96)00006-0. URL: http://www.sciencedirect.com/science/article/pii/0038092X96000060.

[7] M Alonsogarcia, J Ruiz, and F Chenlo. "Experimental study of mismatch and shading effects in the – characteristic of a photovoltaic module". In: *Solar Energy Materials and Solar Cells* 90.3 (2006), pp. 329–340. ISSN: 09270248. DOI: 10.1016/j.solmat.2005.04.022. URL: http://linkinghub.elsevier.com/retrieve/pii/S0927024805001145.

[8] Jubaer Ahmed and Zainal Salam. "A critical evaluation on maximum power point tracking methods for partial shading in PV systems". In: *Renewable and Sustainable Energy Reviews* 47 (2015), pp. 933–953. ISSN: 13640321. DOI: 10.1016/j.rser.2015.03.080. URL: http://linkinghub.elsevier.com/retrieve/pii/S1364032115002336.

[9] W Bower and J Wiles. "Investigation of ground-fault protection devices for photovoltaic power system applications". In: *Conference Record of the Twenty-Eighth IEEE Photovoltaic Specialists Conference - 2000 (Cat. No.00CH37036)*. Vol. 6. d. IEEE, 2000, pp. 1378–1383. ISBN: 0-7803-5772-8. DOI: 10.1109/PVSC.2000.916149. URL: http://ieeexplore.ieee.org/lpdocs/epic03/wrapper.htm?arnumber=916149.

[10] D. Stellbogen. "Use of PV circuit simulation for fault detection in PV array fields". In: *Conference Record of the Twenty Third IEEE Photovoltaic Specialists Conference - 1993 (Cat. No.93CH3283-9)*. IEEE, 1993, pp. 1302–1307. ISBN: 0-7803-1220-1. DOI: 10.1109/PVSC.1993.346931. URL: http://ieeexplore.ieee.org/lpdocs/epic03/wrapper.htm?arnumber=346931.

[11] N. Boutasseta, M. Ramdani, and S. Aouabdi. "Performance evaluation of photovoltaic arrays subject to a Line-Ground fault". In: *3rd International Conference on Systems and Control*. IEEE, 2013, pp. 83–86. ISBN: 978-1-4799-0275-0. DOI: 10.1109/ICoSC.2013.6750839. URL: http://ieeexplore.ieee.org/lpdocs/epic03/wrapper.htm?arnumber=6750839.

[12] Ye Zhao et al. "Line–Line Fault Analysis and Protection Challenges in Solar Photovoltaic Arrays". In: *IEEE Transactions on Industrial Electronics* 60.9 (2013), pp. 3784–3795. ISSN: 0278-0046. DOI: 10.1109/TIE.2012.2205355. URL: http://ieeexplore.ieee.org/lpdocs/epic03/wrapper.htm?arnumber=6221990.

[13] A. Mellit, G.M. Tina, and S.A. Kalogirou. "Fault detection and diagnosis methods for photovoltaic systems: A review". In: *Renewable and Sustainable Energy Reviews* 91 (2018), pp. 1–17. ISSN: 13640321. DOI: 10.1016/j.rser.2018.03.062. URL: https://linkinghub.elsevier.com/retrieve/pii/S1364032118301370.

[14] Asma Triki-Lahiani, Afef Bennani-Ben Abdelghani, and Ilhem Slama-Belkhodja. "Fault detection and monitoring systems for photovoltaic installations: A review". In: *Renewable and Sustainable Energy Reviews* 82 (2018), pp. 2680–2692. ISSN: 13640321. DOI: 10.1016/j.rser.2017.09.101. URL: https://linkinghub.elsevier.com/retrieve/pii/S1364032117313618.

[15] Ye Zhao et al. "Graph-Based Semi-supervised Learning for Fault Detection and Classification in Solar Photovoltaic Arrays". In: *IEEE Transactions on Power Electronics* 30.5 (2015), pp. 2848–2858. ISSN: 0885-8993. DOI: 10.1109/TPEL.2014.2364203. URL: http://ieeexplore.ieee.org/document/6933939/.

[16] Mohd Nafis Akram and Saeed Lotfifard. "Modeling and Health Monitoring of DC Side of Photovoltaic Array". In: *IEEE Transactions on Sustainable Energy* 6.4 (2015), pp. 1245–1253. ISSN: 19493029. DOI: 10.1109/TSTE.2015.2425791.

[17] J.J. Schoeman and J.D. Wyk. "A simplified maximal power controller for terrestrial photovoltaic panel arrays". In: *1982 IEEE Power Electronics Specialists conference*. 1982, pp. 361–367. DOI: 10.1109/PESC.1982.7072429. URL: http://ieeexplore.ieee.org/articleDetails.jsp?arnumber=7072429.

[18] Trishan Esram and Patrick L Chapman. "Comparison of Photovoltaic Array Maximum Power Point Tracking Techniques". In: *IEEE Transactions on Energy Conversion* 22.2 (2007), pp. 439–449. ISSN: 0885-8969. DOI: 10.1109/TEC.2006.874230. URL: http://ieeexplore.ieee.org/lpdocs/epic03/wrapper.htm?arnumber=4207429.

[19] V. Salas et al. "Review of the maximum power point tracking algorithms for stand-alone photovoltaic systems". In: *Solar Energy Materials and Solar Cells* 90.11 (2006), pp. 1555–1578. ISSN: 09270248. DOI: 10.1016/j.solmat.2005.10.023. URL: http://linkinghub.elsevier.com/retrieve/pii/S0927024805003582.

[20] Kashif Ishaque and Zainal Salam. "A review of maximum power point tracking techniques of PV system for uniform insolation and partial shading condition". In: *Renewable and Sustainable Energy Reviews* 19 (2013), pp. 475–488. ISSN: 13640321. DOI: 10.1016/j.rser.2012.11.032. URL: http://dx.doi.org/10.1016/j.rser.2012.11.032http://linkinghub.elsevier.com/retrieve/pii/S1364032112006442http://www.sciencedirect.com/science/article/pii/S1364032112006442.

[21] Ziyad Salameh and Daniel Taylor. "Step-up maximum power point tracker for photovoltaic arrays". In: *Solar Energy* 44.1 (1990), pp. 57–61. ISSN: 0038092X. DOI: 10.1016/0038-092X(90)90027-A. URL: http://www.sciencedirect.com/science/article/pii/0038092X9090027A.

[22] D Lalili et al. "Input output feedback linearization control and variable step size MPPT algorithm of a grid-connected photovoltaic inverter". In: *Renewable Energy* 36.12 (2011), pp. 3282–3291. ISSN: 09601481. DOI: 10.1016/j.renene.2011.04.027. URL: http://www.sciencedirect.com/science/article/pii/S0960148111001996.

[23] R. Ramaprabha, M. Balaji, and B.L. Mathur. "Maximum power point tracking of partially shaded solar PV system using modified Fibonacci search method with fuzzy controller". In: *International Journal of Electrical Power & Energy Systems* 43.1 (2012), pp. 754–765. ISSN: 01420615.

DOI: 10.1016/j.ijepes.2012.06.031. URL: http://linkinghub.elsevier.com/retrieve/pii/S0142061512002931.

[24] Kashif Ishaque et al. "An Improved Particle Swarm Optimization (PSO)–Based MPPT for PV With Reduced Steady-State Oscillation". In: *IEEE Transactions on Power Electronics* 27.8 (2012), pp. 3627–3638. ISSN: 0885-8993. DOI: 10.1109/TPEL.2012.2185713. URL: http://ieeexplore.ieee.org/lpdocs/epic03/wrapper.htm?arnumber=6138329.

[25] N. Boutasseta. "PSO-PI based Control of Photovoltaic Arrays". In: *International Journal of Computer Applications* 48.17 (2012), pp. 36–40. ISSN: 09758887. DOI: 10.5120/7444-0557. URL: http://research.ijcaonline.org/volume48/number17/pxc3880557.pdf.

[26] J. Prasanth Ram and N. Rajasekar. "A new global maximum power point tracking technique for solar photovoltaic (PV) system under partial shading conditions (PSC)". In: *Energy* 118 (2017), pp. 512–525. ISSN: 03605442. DOI: 10.1016/j.energy.2016.10.084. URL: http://linkinghub.elsevier.com/retrieve/pii/S0360544216315183.

[27] Masafumi Miyatake et al. "Maximum Power Point Tracking of Multiple Photovoltaic Arrays: A PSO Approach". In: *IEEE Transactions on Aerospace and Electronic Systems* 47.1 (2011), pp. 367–380. ISSN: 0018-9251. DOI: 10.1109/TAES.2011.5705681. URL: http://ieeexplore.ieee.org/lpdocs/epic03/wrapper.htm?arnumber=5705681.

[28] Xue Lin et al. "Designing Fault-Tolerant Photovoltaic Systems". In: *IEEE Design & Test* 31.3 (2014), pp. 76–84. ISSN: 2168-2356. DOI: 10.1109/MDAT.2013.2288252. URL: http://ieeexplore.ieee.org/document/6651710/.

[29] Eunice Ribeiro, Antonio J. Marques Cardoso, and Chiara Boccaletti. "Fault-Tolerant Strategy for a Photovoltaic DC–DC Converter". In: *IEEE Transactions on Power Electronics* 28.6 (2013), pp. 3008–3018. ISSN: 0885-8993. DOI: 10.1109/TPEL.2012.2226059. URL: http://ieeexplore.ieee.org/document/6340353/.

[30] Nadir Boutasseta, Messaoud Ramdani, and Saad Mekhilef. "Fault-tolerant power extraction strategy for photovoltaic energy systems". In: *Solar Energy* 169 (2018), pp. 594–606. ISSN: 0038092X. DOI: 10.1016/j.solener.2018.05.031. URL: https://linkinghub.elsevier.com/retrieve/pii/S0038092X1830464X.

[31] M. G. Villalva, J.R. Gazoli, and E.R. Filho. "Comprehensive Approach to Modeling and Simulation of Photovoltaic Arrays". In: *IEEE Transactions on Power Electronics* 24.5 (2009), pp. 1198–1208. ISSN: 0885-8993. DOI: 10.1109/TPEL.2009.2013862. URL: http://ieeexplore.ieee.org/lpdocs/epic03/wrapper.htm?arnumber=4806084.

[32] M. G. Villalva, Jonas Rafael Gazoli, and Ernesto Ruppert Filho. "Modeling and circuit-based simulation of photovoltaic arrays". In: *2009 Brazilian Power Electronics Conference*. Vol. 14. 1. IEEE, 2009, pp. 1244–1254. ISBN: 978-1-4244-3369-8. DOI: 10.1109/COBEP.2009.5347680. URL: http://ieeexplore.ieee.org/lpdocs/epic03/wrapper.htm?arnumber=5347680.

[33] Jing Jun Soon and Kay-Soon Low. "Photovoltaic Model Identification Using Particle Swarm Optimization With Inverse Barrier Constraint". In: *IEEE Transactions on Power Electronics* 27.9 (2012), pp. 3975–3983. ISSN: 0885-8993. DOI: 10.1109/TPEL.2012.2188818. URL: https://ieeexplore.ieee.org/document/6165376/.

[34] Jyri Kivimaki et al. "Revisited Perturbation Frequency Design Guideline for Direct Fixed-Step Maximum Power Point Tracking Algorithms". In: *IEEE Transactions on Industrial Electronics* 64.6 (2017), pp. 4601–4609. ISSN: 02780046. DOI: 10.1109/TIE.2017.2674589.

[35] Jyri Kivimaki et al. "Design Guidelines for Multi-Loop Perturbative Maximum Power Point Tracking Algorithms". In: *IEEE Transactions on Power Electronics* 8993.c (2017), pp. 1–1. ISSN: 0885-8993. DOI: 10.1109/TPEL.2017.2683268. URL: http://ieeexplore.ieee.org/document/7879313/.

[36] M.G. Villalva, T.G. de Siqueira, and E. Ruppert. "Voltage regulation of photovoltaic arrays: small-signal analysis and control design". In: *IET Power Electronics* 3.6 (2010), p. 869. ISSN: 17554535. DOI: 10.1049/iet-pel.2008.0344. URL: http://digital-library.theiet.org/content/journals/10.1049/iet-pel.2008.0344.

[37] Mohammed Khorshed Alam et al. "A Comprehensive Review of Catastrophic Faults in PV Arrays: Types, Detection, and Mitigation Techniques". In: *IEEE Journal of Photovoltaics* 5.3 (2015), pp. 982–997. ISSN: 2156-3381. DOI: 10.1109/JPHOTOV.2015.2397599. URL: http://ieeexplore.ieee.org/document/7045450/.

[38] E Koutroulis, K Kalaitzakis, and N C Voulgaris. "Development of a microcontroller-based, photovoltaic maximum power point tracking control system". In: *Power Electronics, IEEE Transactions on* 16.1 (2001), pp. 46–54. ISSN: 0885-8993. DOI: 10.1109/63.903988.

[39] Panagiotis E. Kakosimos and Antonios G. Kladas. "Implementation of photovoltaic array MPPT through fixed step predictive control technique". In: *Renewable Energy* 36.9 (2011), pp. 2508–2514. ISSN: 09601481. DOI: 10.1016/j.renene.2011.02.021. URL: http://linkinghub.elsevier.com/retrieve/pii/S0960148111001121.

[40] Weidong Xiao and W.G. Dunford. "A modified adaptive hill climbing MPPT method for photovoltaic power systems". In: *2004 IEEE 35th Annual Power Electronics Specialists Conference (IEEE Cat. No.04CH37551)*. Vol. 3. IEEE, 2004, pp. 1957–1963. ISBN: 0-7803-8399-0. DOI: 10.1109/PESC.2004.1355417. URL: http://ieeexplore.ieee.org/document/1355417/.

[41] K.H. Hussein. "Maximum photovoltaic power tracking: an algorithm for rapidly changing atmospheric conditions". In: *IEE Proceedings - Generation, Transmission and Distribution* 142.1 (1995), p. 59. ISSN: 13502360. DOI: 10.1049/ip-gtd:19951577. URL: http://digital-library.theiet.org/content/journals/10.1049/ip-gtd{_}19951577.

[42] J. Kennedy and R. Eberhart. "Particle swarm optimization". In: *Proceedings of ICNN'95 - International Conference on Neural Networks*. Vol. 4. IEEE, pp. 1942–1948. ISBN: 0-7803-2768-3. DOI: 10.1109/ICNN.1995.488968. URL: http://ieeexplore.ieee.org/document/488968/.

[43] Russell C Eberhart and Yuhui Shi. "Comparison between genetic algorithms and particle swarm optimization". In: *Evolutionary Programming VII*. 1998, pp. 611–616. ISBN: 978-3-540-64891-8. DOI: 10.1007/BFb0040812. URL: http://link.springer.com/10.1007/BFb0040812.

[44] Emad Elbeltagi, Tarek Hegazy, and Donald Grierson. "Comparison among five evolutionary-based optimization algorithms". In: *Advanced Engineering Informatics* 19.1 (2005), pp. 43–53. ISSN: 14740346. DOI: 10.1016/j.aei.2005.01.004. URL: http://linkinghub.elsevier.com/retrieve/pii/S1474034605000091.

[45] Y Shi and R C Eberhart. "Empirical study of particle swarm optimization". In: *Evolutionary Computation, 1999. CEC 99. Proceedings of the 1999 Congress on* 3 (1999), 1–1950 Vol. 3. ISSN: 1089-778X. DOI: 10.1109/CEC.1999.785511.

[46] Ron J Patton. "Fault-Tolerant Control: The 1997 Situation". In: *IFAC Proceedings Volumes* 30.18 (1997), pp. 1029–1051. ISSN: 14746670. DOI: 10.1016/S1474-6670(17)42536-5. URL: http://linkinghub.elsevier.com/retrieve/pii/S1474667017425365.

[47] Youmin Zhang and Jin Jiang. "Bibliographical review on reconfigurable fault-tolerant control systems". In: *Annual Reviews in Control* 32.2 (2008), pp. 229–252. ISSN: 13675788. DOI: 10.1016/j.arcontrol.2008.03.008. URL: http://linkinghub.elsevier.com/retrieve/pii/S1367578808000345.

[48] Jin Jiang and Xiang Yu. "Fault-tolerant control systems: A comparative study between active and passive approaches". In: *Annual Reviews in Control* 36.1 (2012), pp. 60–72. ISSN: 13675788. DOI: 10.1016/j.arcontrol.2012.03.005. URL: http://www.sciencedirect.com/science/article/pii/S1367578812000065.

[49] Hassan Noura et al. *Fault-tolerant Control Systems*. Advances in Industrial Control. London: Springer London, 2009. ISBN: 978-1-84882-652-6. DOI: 10.1007/978-1-84882-653-3. URL: http://link.springer.com/10.1007/978-1-84882-653-3.

[50] Kashif Ishaque et al. "A direct control based maximum power point tracking method for photovoltaic system under partial shading conditions using particle swarm optimization algorithm". In: *Applied Energy* 99 (2012), pp. 414–422. ISSN: 03062619. DOI: 10.1016/j.apenergy.2012.05.026. URL: http://linkinghub.elsevier.com/retrieve/pii/S0306261912003996.